Organic-Inorganic Hybrid Photovoltaics Based on Organometal Halide Perovskites

by

Michael M. Lee

A thesis submitted to the Faculty of the

Condensed Matter Physics

In Fulfillment of the Requirements
For the Degree of

Doctor of Philosophy

University of Oxford
Merton College

2 0 1 3

To the memory of my grandparents.

Statement by Author

This thesis has been submitted in complete fulfilment of the requirements for an advanced degree at The University of Oxford and is deposited in the University Library to be made available to borrowers under rules of the Library.

Brief quotations from this thesis are allowable without special permission, provided that accurate acknowledgment of source is made. Requests for permission for extended quotation from or reproduction of this manuscript in whole or in part may be granted by the head of the major department or the Dean of the Graduate College when in his or her judgment the proposed use of the material is in the interests of scholarship. In all other instances, however, permission must be obtained from the author.

Mike didn't really discover the perovskite solar cell- in the same way Leibniz didn't really discover calculus. They did name a biscuit after Leibniz; that's probably the best he can hope for.

My ever-supportive friends

Acknowledgments

I would like to thank Dr Henry J. Snaith, Agnese Abrusci, Pablo Docampo, Leonie O. Vogt, Sandeep K. Pathak, Andrew S. Hey, Edward J. W. Crossland esq., James M. Ball, and the rest of the Snaith Group. I would further like to thank our collaborators in Japan: Nobuya Sakai, Dr Takurou Murakami, Prof. Tsutomu Miyasaka. I would like to thank my friends at Merton College: Caterina Doglioni, Daniel R. Short, Craig N. Lumb, William R. Upcher, Melllvar L. Duncan; the football chaps: So Solid-State FC (Physics) Mark J. Holmes and Peter Babkevich and the College team: Merton-Hertford FC. I would also like to thank Prof. Stephen Blundell, and my old professors: Prof. Keith Bennett and Prof. Mike Petty. Cheers, guys.

Table of Contents

Table of Contents—*Continued*

Abstract

This thesis details the development of a novel photovoltaic device based on organometal halide perovskites. The initial focus of this thesis begins with the study of light-trapping strategies in solid-state dye-sensitised solar cells (detailed in chapter 3). While I report enhancement in device performance through the application of near and far-field light-trapping techniques, I find that improvements remain step-wise due to fundamental limitations currently employed in dye-sensitised solar cell technology—notably, the available light-sensitising materials. I found a promising yet under researched family of materials in the methyl ammonium tri-halide plumbate perovskite (detailed in chapter 4). The perovskite light-sensitiser was applied to the traditional mesoscopic sensitised solar cell device architecture as a replacement to conventional dye yielding world-record breaking photo-conversion efficiencies for solid-state sensitised solar cells as high as 8.5%. The system was further developed leading to the conception of a novel device architecture, termed the mesoporous superstructured solar cell (MSSC), this new architecture replaces the conventional mesoporous titanium dioxide semiconductor with a porous insulating oxide in aluminium oxide, resulting in very low fundamental losses evidenced through high photo-generated open-circuit voltages of over 1.1 V. This development has delivered striking photo-conversion efficiencies of 10.9% (detailed in chapter 6).

Organic-Inorganic Hybrid Photovoltaics Based on Organometal Halide Perovskites

Michael M. Lee, D. Phil
The University of Oxford, 2 0 1 3

Supervisor: Dr Henry J. Snaith

This thesis details the development of a novel photovoltaic device based on organometal halide perovskites. The initial focus of this thesis begins with the study of light-trapping strategies in solid-state dye-sensitised solar cells (detailed in chapter 3). While I report enhancement in device performance through the application of near and far-field light-trapping techniques, I find that improvements remain step-wise due to fundamental limitations currently employed in dye-sensitised solar cell technology—notably, the available light-sensitising materials. I found a promising yet under researched family of materials in the methyl ammonium tri-halide plumbate perovskite (detailed in chapter 4). The perovskite light-sensitiser was applied to the traditional mesoscopic sensitised solar cell device architecture as a replacement to conventional dye yielding world-record breaking photo-conversion efficiencies for solid-state sensitised solar cells as high as 8.5%. The system was further developed leading to the conception of a novel device architecture, termed the mesoporous superstructured solar cell (MSSC), this new architecture replaces the conventional mesoporous titanium dioxide semiconductor with a porous insulating oxide in aluminium oxide, resulting in very low fundamental losses evidenced through high photo-generated open-circuit voltages of over 1.1 V. This development has delivered striking photo-conversion efficiencies of 10.9% (detailed in chapter 6).

1. Introduction

"Water, water, everywhere
And all the boards did shrink
Water, water everywhere
Nor any drop to drink."

– S. T. Coleridge *The Rime of the Ancient Mariner*

The power reaching the Earth from the sun is 120,000 TW while the global energy demand currently stands at 15 TW. Evidently the world's energy demands can be satisfied through the conversion of a fraction of the solar radiation incident on the Earth's surface without incurring any direct cost of generating carbon dioxide emissions [1].

Diminishing returns in conventional photovoltaic technology is a fundamental reason for the resistive uptake of solar energy; whilst traditional photovoltaic technologies are edging ever closer to their theoretical maxima for power-conversion efficiency, costs of production remain high. A shift in focus towards cost-reduction is needed to ensure photovoltaics become economically viable by remaining competitive with other sources of energy. Solution-processable materials such as organic molecules, conjugated polymers, and semiconductor nanocrystals offer new and exciting routes to the low-cost production of photovoltaics [1]. Reel-to-reel printing offers a bona fide opportunity to produce electronics rapidly, with the potential of very large-area processing, in ambient conditions (notably without the need for clean room facilities or highly controlled environments) thus at very low cost. The consideration of materials is also an important factor for cost reduction and the toxicity of materials is worth considering with regards to sustainability and recycling. One of the leading inorganic

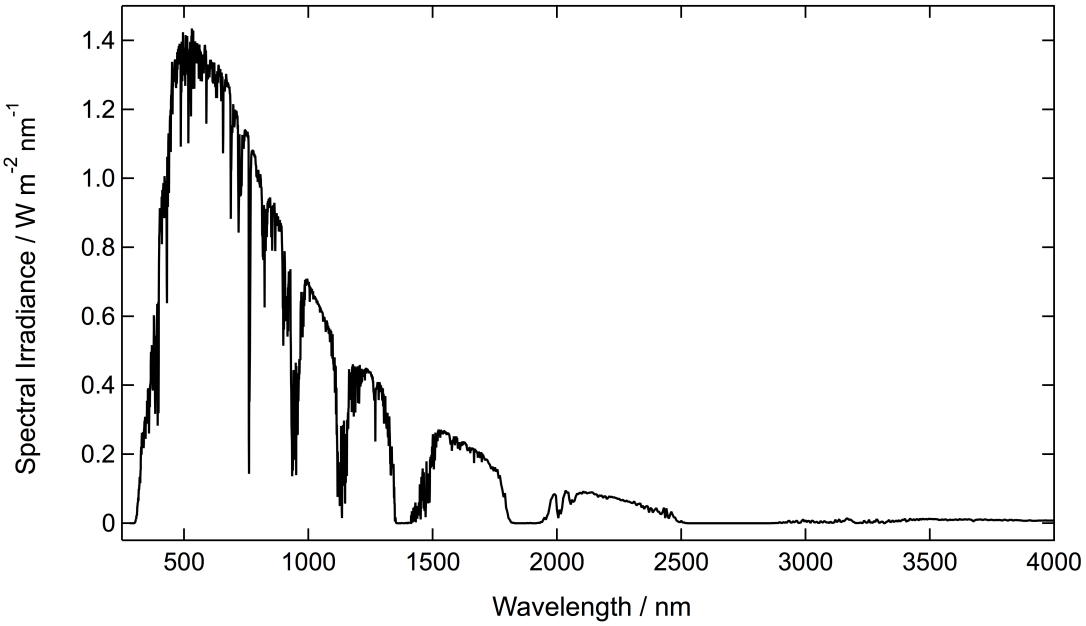

FIGURE 1.1. AM 1.5G solar radiation spectrum. (This data is based on the American Society for Testing and Materials (ASTM) Terrestrial Reference Spectra, which are standards adopted by the photovoltaics industry to ensure consistent test conditions and are similar to the light that could be expected in North America.)

photovoltaic technologies uses cadmium telluride and indium- both materials may become expensive to harvest at high volume [2]. By comparison materials used for organic photovoltaics can be found and made in abundance. Copper phthalocyanine is a widely used molecule that is manufactured at a rate of 100000 tons per year, this would roughly produce $10^{11}\mathrm{m}^2$ of solar cell 1 μm thick which at 10% efficiency would generate around 10 TW.

Organic electronics offer a lightweight, large-area, low-cost, and mechanically robust- both highly flexible and highly durable- alternative to inorganic electronics. Indeed, the physical properties of organic materials generate new and exciting opportunities for the integration of electronics where inorganic materials would be unsuitable or economically unviable

1.1. Photovoltaic fundamentals

A photovoltaic device operates in three stages: first, a sufficiently energetic photon (possessing energy greater than, or equal, to the band gap) is absorbed causing the excitation of an electron from the ground state across a band gap to a higher energy level, leaving a hole in the ground state; second, the photo-excited charges are split from their generation site due to an intrinsic energetic asymmetry in the device; finally the charges are extracted to an external circuit to do useful work. By illuminating a solar cell under simulated sunlight (typically AM 1.5G 100 mW cm^{-2}) a current-voltage (J-V) curve can be generated, from this curve we extract performance parameters of the cell. An ideal solar cell is described by the following equation:

$$J = J_{SC} - J_0(e^{\frac{eV}{kT}} - 1) \tag{1.1}$$

Where J_{SC} is the short-circuit current density, J_0 is a constant dark saturation current and k is Boltzmann's constant. The second term $J_0(e^{\frac{eV}{kT}}-1)$ is the dark current density, which arises because a potential difference develops across the terminals whenever a load is present. This causes a current in the opposite direction to the photocurrent, hence reducing the net current from its value when no load is present (J_{SC}). The power generated by a solar cell is given by P = VI. It is hence zero when no load is present (short-circuit, V = 0) as well as when an infinite load is present (open-circuit, I = 0). The maximum power generated by a cell will be at a load somewhere between these two extremes.

A good solar cell has high short-circuit current, high open-circuit voltage and a high fill factor. The latter is a measure of ideality in the device - the more square the curve the closer the solar cell is to operating as a perfect device. The fill factor is related to resistances within the photovoltaic device, see Figure 1.3.

$$FF = \frac{J_{MP}V_{MP}}{J_{SC}V_{OC}} \tag{1.2}$$

Where J_{MP} and V_{MP} are the current density and voltage at the maximum power point, respectively and V_{OC} is the open circuit voltage. Ultimately the efficiency, η, of the cell is the quantity summarising all of these performance parameters. It is defined as the power density delivered by the cell at the ideal operating point (J_{MP} — V_{MP}) as a fraction of the light power density incident on the cell P_i.

$$\eta = \frac{J_{MP}V_{MP}}{P_i} = \frac{J_{SC}V_{OC}FF}{P_i} \tag{1.3}$$

External quantum efficiency is the ratio of the number of carriers extracted by the solar cell to the number of photons of a given energy incident on the solar cell. If all photons of a certain wavelength are absorbed and the resulting carriers are collected, then the quantum efficiency at that particular wavelength is unity. Internal quantum efficiency (IQE) is the EQE per absorbed photon, thus IQE takes into account losses due to reflection and low absorptivity.

1.2. Traditional photovoltaics / 1st generation solar

Conventional silicon *pn*-junction solar cells perform all three processes of light absorption, charge separation and charge transport within the same bulk material. The advantage is that there are no losses due to interface states, however, finding a material capable of performing all three processes requires some compromise. Silicon has an indirect band gap and suffers from poor optical absorption, thus thicknesses of 300–500 μm are required in order to sufficiently harvest all the incident light. The thick absorber layer requires charge carriers to travel further, resulting in more opportunities for recombination and scattering from defects. This sets stringent demands on the quality of the silicon which ultimately drives costs upward.

The absorption of a photon causes the formation of the neutral quasi-particle commonly known as the exciton. This is a bound state of an electron-hole pair which

can transport energy yet being electrically neutral doesn't transport charge. The binding energy of an exciton is given by:

$$E_B = V_{Coulomb} = \frac{e^2}{4\pi\varepsilon_0\varepsilon_r r} \tag{1.4}$$

In a semiconductor such as silicon the dielectric constant is usually large, thus screening the electric field between electrons and holes in the material. This results in a Wannier-Mott exciton which is loosely bound (with binding energies of 0.01 - 0.1 eV) and has its radius extending beyond the lattice spacing of the material as visually depicted in figure 1.2.

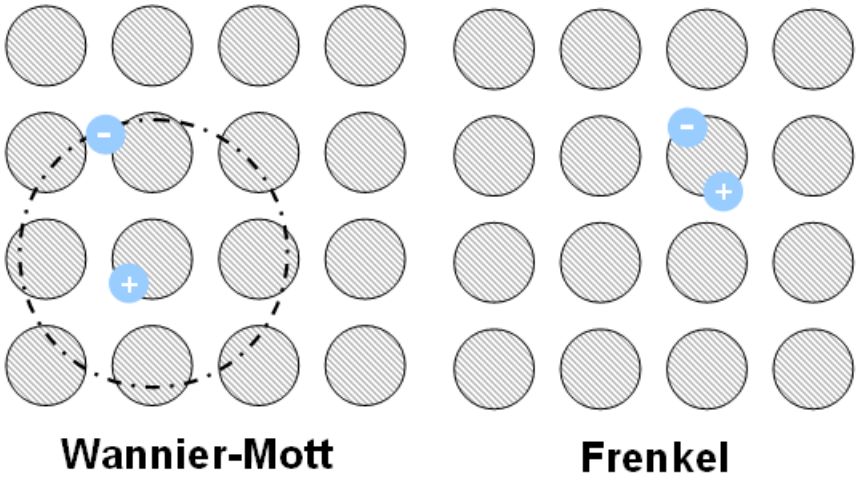

FIGURE 1.2. Schematic representation of Wannier-Mott excitons (left), and Frenkel excitons (right)

1.3. Towards low-cost / 2nd Generation Solar

Thin-film architectures for photovoltaics have become popular due to the promise of cost-reduction through lower material usage, simplified manufacture with materials compatible with flexible systems. The ultimate target is low-cost photovoltaics via rapid reel-to-reel processing. The leading second generation thin-film technologies are

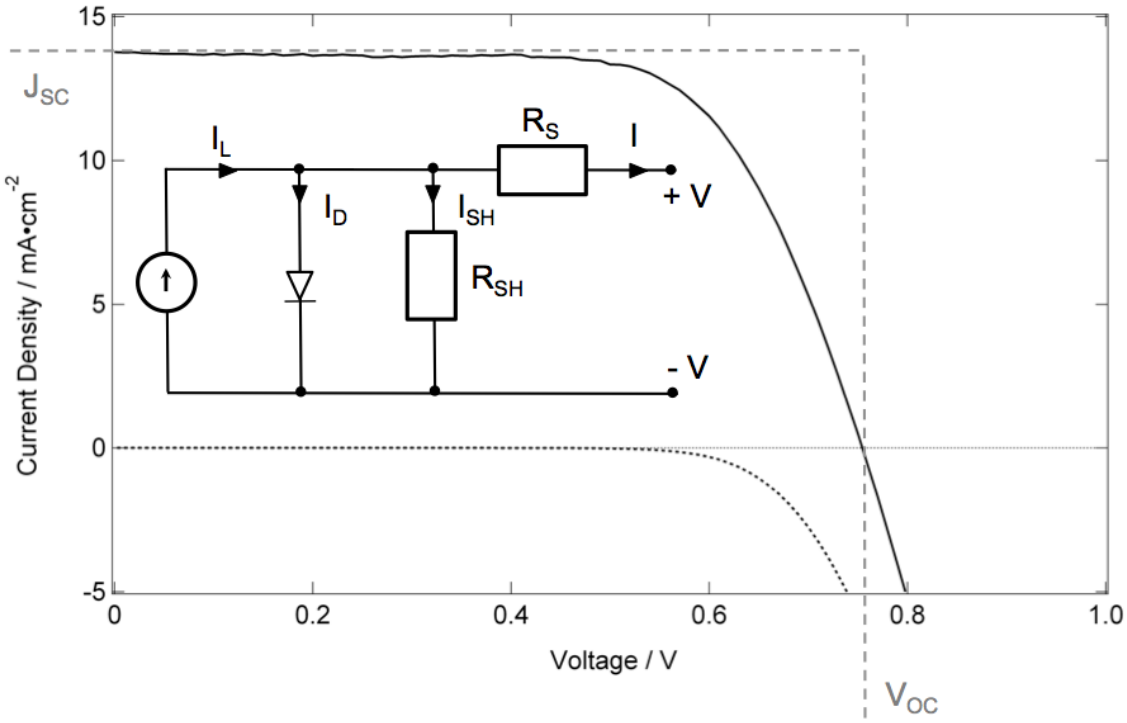

FIGURE 1.3. Typical current-voltage curve of a photovoltaic device under illumination (full trace) and without illumination (dashed trace). Key parameters: open-circuit voltage and short-circuit current density are also displayed. Equivalent circuit is drawn as an inset where I = output current, I_L = photogenerated current, I_D = diode current, I_{SH} = shunt current, V = voltage across the output terminals, R_S = series resistance, R_{SH} = shunt resistance.

copper indium gallium selenide (CIGS), cadmium telluride (CdTe), and amorphous silicon see Figure 1.7. Recently, the Swiss Federal Laboratories for Materials Science and Technology (Empa) have achieved 20.4% on flexible substrates with their CIGS cells.

1.4. New and Emerging Photovoltaics / 3rd Generation Solar

Unlike conventional photovoltaic systems based on the *pn*-junction in which light absorption, charge separation and charge transport all occur within one material a

dye-sensitised solar cell allocates each of these processes to a different component in the device. The current embodiment of the dye-sensitised solar cell was first developed by O'Regan and Graetzel in 1991 [3].

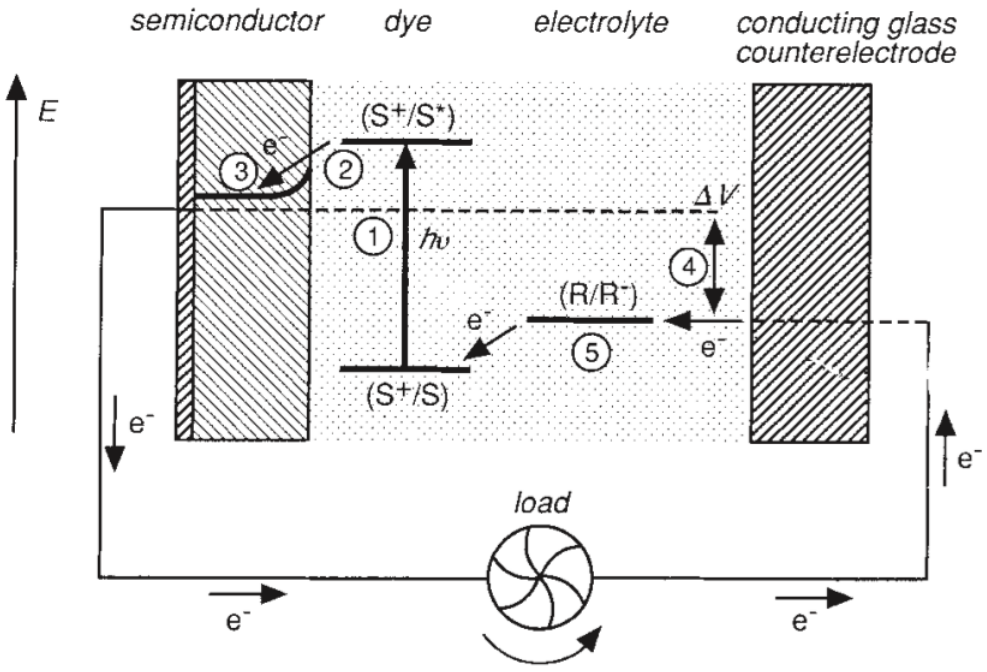

FIGURE 1.4. Dye-sensitised solar sell device schematic and energetic landscape. Permission requested from [3]

Consider Figure 1.4, under illumination the dye is excited from its ground state (S) into an excited state (S^*): (1) $S + h\nu \rightarrow S^*$, the electron in the excited state is injected into a wide band gap n-type semiconductor (in this case titanium dioxide, TiO_2): (2) $S^* \rightarrow S^+ + e_{CB}$, which is then conducted to the anode (3). The photo-voltage is determined by the difference of the quasi-Fermi level of TiO_2 under illumination and the Nernst potential of the redox couple in the electrolyte (4). The oxidised dye is regenerated through a reduction and oxidation (redox) process with the liquid electrolyte thus returning an electron to the ground state of the dye molecule: (5) $S^+ + R \rightarrow S + R^+$. Here the dye serves as an 'electrochemical pump' driving low

energy electrons in the ground state into higher energy electrons in the excited state. Generally the metal oxide is mesostructured. Indeed, mesostructuring was the major breakthrough for DSCs in 1991 since it enabled a large interface across which the excitons can be split and to increase optical absorption of the sensitiser.

Kinetic competition distinguishes the dye-sensitised solar cell from conventional solar cells: in a conventional device there exists no competition of processes at the interface since an exciton is formed, separated by a field and then transported to the terminals. For the DSC carefully timed processes ensure the device operates effectively. Below is a list of processes and timings in a typical DSC:

- Electron injection: fs to ps [4]
- Dye natural lifetime: ns - μs scale [4]
- Dye regeneration: μs for liquid-state, ps for solid-state [5, 6]
- Interfacial recombination: 100 μs - ms [5, 7]

Dye regeneration and interfacial recombination occur at similar time scales hence transport direction is decided by the result of kinetic competition. Further, organic molecules typically have small dielectric constants and Coulomb interactions between electrons and holes can therefore be quite large. The absorption of a photon therefore creates a Frenkel exciton, bound tightly (binding energies of 0.1 - 1 eV) with a radius comparable to the size of the unit cell (Figure 1.2). How far an exciton can travel in its bound state is given by the exciton diffusion length, generally only a few tens of nanometers for Frenkel excitons. It is therefore crucial that charge separation occurs quickly.

The benefit of separating the three photovoltaic stages of light absorption, charge separation and charge transport (where majority charge carriers exist in separate phases thus eliminating recombination in the bulk, leaving only surface recombination to contend with) to different components enables the optimisation of individual

elements. Hybrid architectures offer a vast library of materials for device optimisation, including a variety of metal oxides, organic and inorganic absorbers, molecular, polymeric and electrolytic hole-conducting media. Beyond this, however, the versatility offered by a hybrid framework allows these new materials to be utilised in novel configurations. The staggering choice of materials places less stringent demands on the quality of the materials used and allows for greater creativity. The confluence of these benefits results in significantly lower costs and the potential for much more innovation.

1.5. Solid-state dye-sensitised solar cell

In the past the hole-transporter used was predominantly a liquid-electrolyte, but recently a solid-state alternative has become more popular. The first efficient solid-state DSC was realised by Bach *et al.* in 1998 [6] employing (2,2(7,7(-tetrakis-(N,N-dipmethoxyphenylamine)9,9(-spirobifluorene) (spiro- OMeTAD). The solid-state DSC operates in very much the same way its liquid predecessor except hole-transport occurs through an organic small molecule hole-transporting medium and the mechanism is hole-hopping rather than molecular diffusion.

Infiltration of the hole-transporter into mesoporous a TiO_2 film is achieved by casting spiro-OMeTAD solution on to the film, soaking the film for a period of time where the pores are filled with solution by capillary action and finally spinning the film to remove excess solution, as can be seen from Figure 1.6. Any excess solution that isn't spun off through the spin-coating process or hasn't evaporated will gel to form an over-layer termed the 'capping layer'. The application of a solid-state hole-transporter has limited the thickness of the active layer due to issues of physically filling the pores of the mesostructure. Kroeze and co-workers report that spiro-OMeTAD could infiltrate a 2 μm film of mesoporous TiO_2, this was confirmed through the use of transient absorption where all the dye cations were observed to transfer holes to

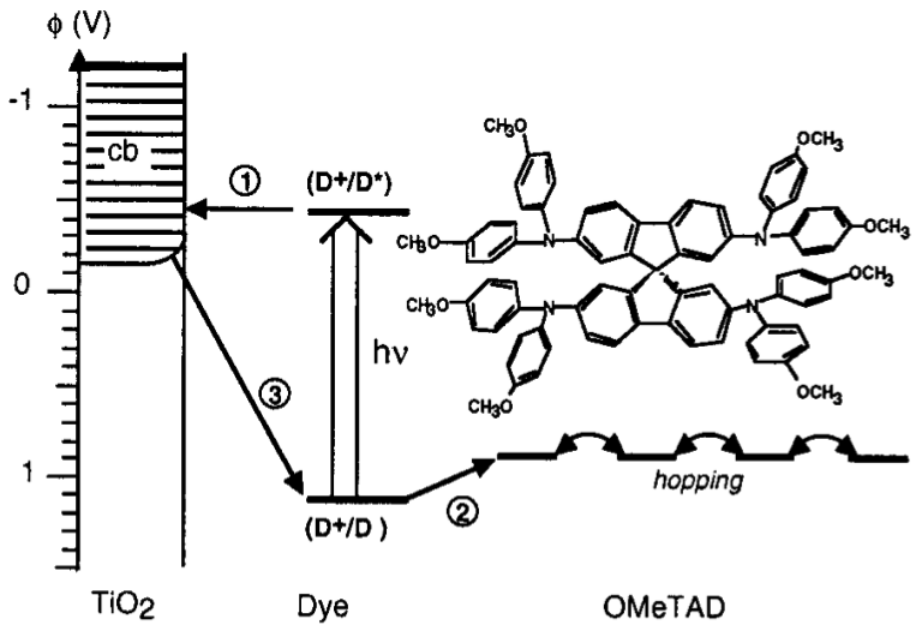

FIGURE 1.5. Solid-State dye-sensitised solar cell with device schematic and energy landscape (permission requested from [6])

spiro-OMeTAD [8]. The study of pore-filling is an important one for solid-state DSCs since the infiltration depth and filling fraction (i.e. the volume fraction of the pores filled by the hole-transporter medium) are important parameters of pore filling: low infiltration depth of spiro-OMeTAD prevents dye molecules at the bottom of the film from transferring photo-generated holes to spiro-OMeTAD thus contributing to photocurrent. Low filling fraction (<49%) leads to lower current densities and lower fill factors [9]. Improving the infiltration of spiro-OMeTAD into mesoporous TiO_2 will lead to more efficient charge collection. Recently it has been shown that infiltration is uniform with depth with only the fraction of dye wetting likely to change [10, 11, 12, 13].

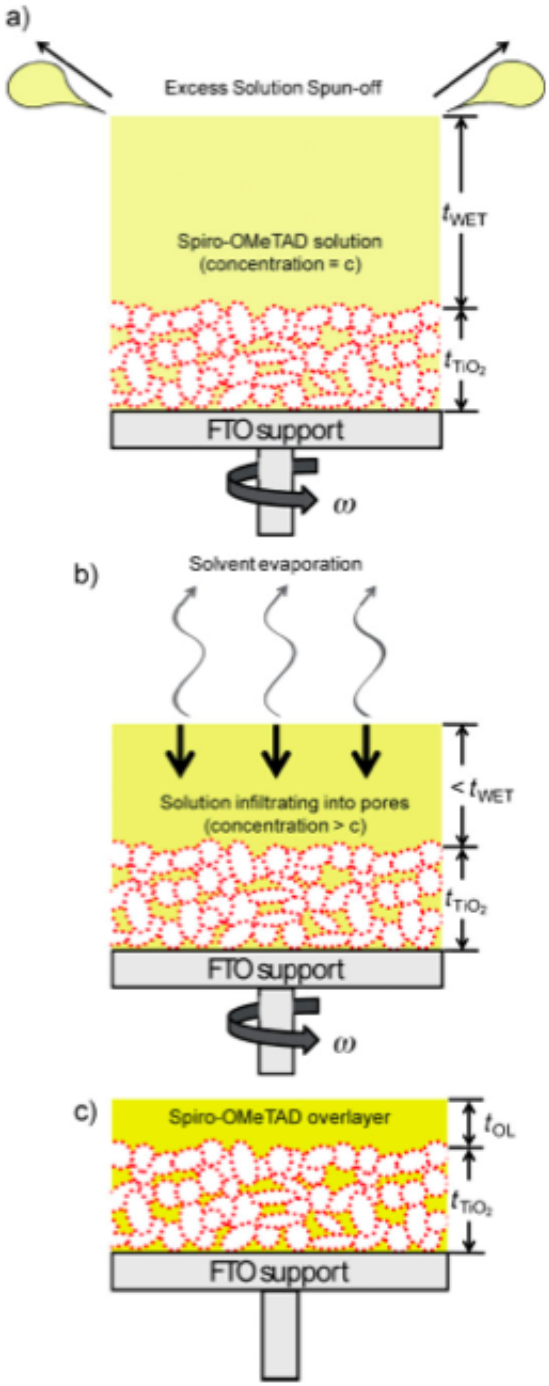

FIGURE 1.6. Schematic illustrating pore-filling mechanism in mesoporous TiO_2 (permission requested from [13])

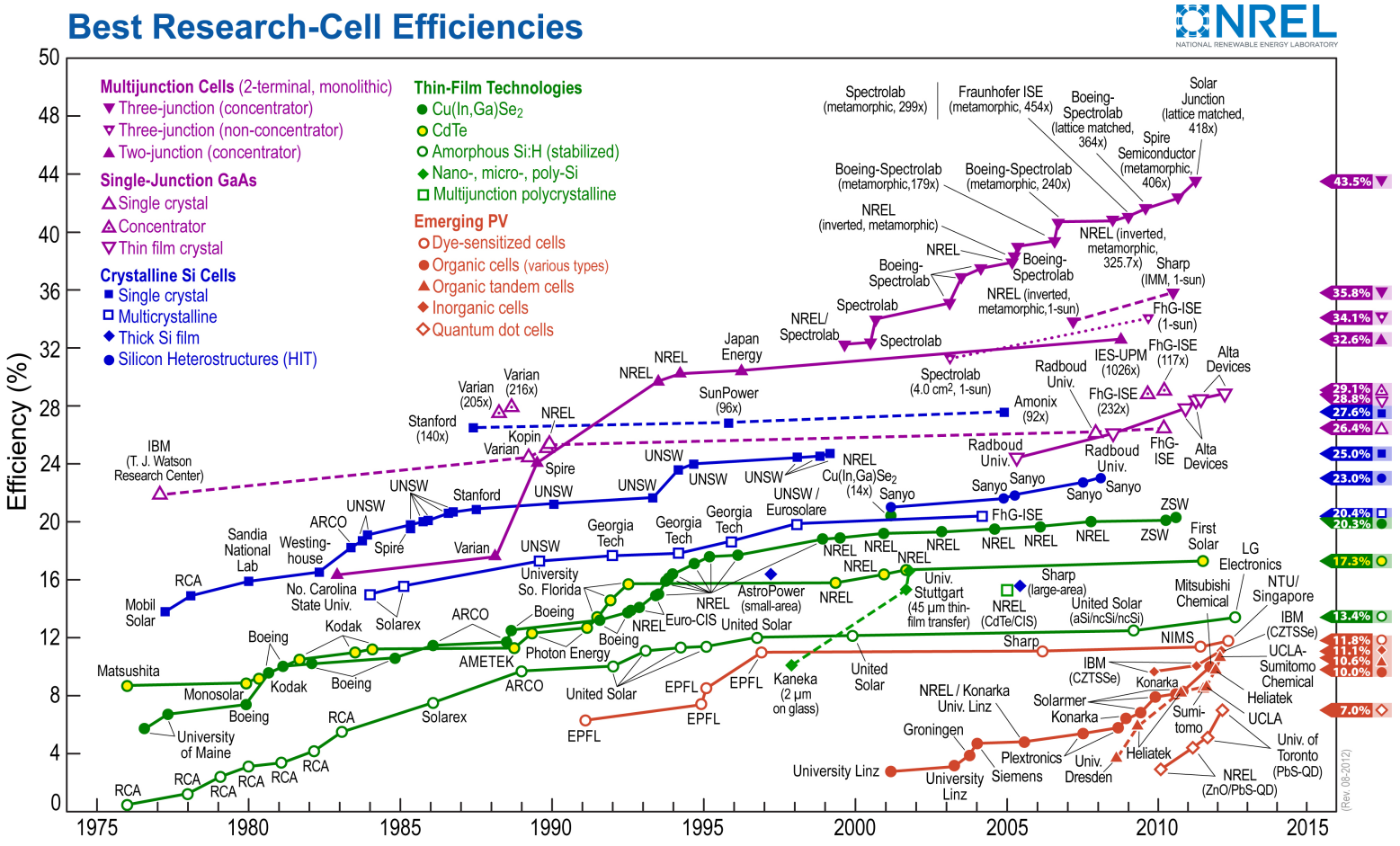

FIGURE 1.7. Conversion efficiencies of best research solar cells worldwide from 1976 through 2012 for various photovoltaic technologies. Efficiencies determined by certified agencies/laboratories

2. Experimental Details

2.1. Device fabrication

Unless stated otherwise all chemicals were purchased from Sigma-Aldrich and were anhydrous if available.

2.1.1. Solid-state dye-sensitised solar cell device fabrication

Substrate cleaning

Fluorine-doped tin oxide (F:SnO_2) coated glass (Pilkington TEC 15) 15 $\Omega/\square$ was patterned by etching with Zn powder and 2 M HCl diluted in milliQ water. The etched substrate was then cleaned with 2% hellmanex diluted in milliQ water, rinsed with milliQ water, acetone and ethanol and dried with clean dry air. The substrate underwent an oxygen plasma treatment for 5 minutes prior to spray pyrolysis of compact titanium dioxide (TiO_2).

Spray pyrolysis of compact TiO_2

A thin layer of compact anatase TiO_2 of roughly 50 nm in thickness was formed through spray pyrolysis of titanium diisopropoxide bis(acetylacetonate) diluted in anhydrous ethanol at a volumetric ratio of 1:10 using N_2 as a carrier gas.

Formation of mesoporous titanium dioxide

0.5 μm thick mesoporous TiO_2 layer was deposited by spin-coating TiO_2 paste (Dyesol 18NR-T) diluted in anhydrous ethanol at 1:2.5 by weight at 2000 RPM. The layers were then sintered in air at 550 °C for 30 minutes. Once cooled and cut down to device size the samples were stored.

Formation of light-sensitising material: dye

The substrates were then immersed in a bath of $TiCl_4$ at a concentration of 15 mM for 1 hour at 70 °C , followed by rinsing in milliQ water and heating to 550 °C and cooled to 70 °C. Once substrates reached 70 °C they were immersed in solution of Z907 dye for 18 hours. Z907 dye was mixed at a concentration of 0.3 mM was dissolved in a solution of acetonitrile anhydrous to tert-butyl alcohol at equal volumetric ratio.

Formation of hole-transporting layer and electrodes

25 μl of a chlorobenzene solution containing 68 mM Spiro-OMeTAD, 55 mM tert-butylpyridine and 9 mM lithium bis(trifluoromethylsyfonyl)imide salt was cast onto the dye coated substrate and spun at a rate of 2000 RPM for 45 seconds. Cells were left in the dark in air overnight prior to thermal evaporation of 200 nm Ag electrodes to complete the solar cells.

2.1.2. Meso-superstructure device fabrication

Following the procedure from section 2.1.1, however, replace formation of mesoporous titanium dioxide and formation of light-sensitising material with the following:

Formation of mesoporous aluminium dioxide

0.5 μm thick mesoporous Al_2O_3 layer was deposited by spin-coating Al_2O_3 paste diluted further in anhydrous ethanol at 1:1.5 by weight at 2000 RPM

Formation of light-sensitising material: perovskite

25 μl of 20 wt% perovskite precursor solution was dispensed onto each pre-prepared mesoporous electrode film spin-coating at 1500 RPM for 30 seconds in air. The coated

films were then placed on a hot plate set at 100 °C for 45 minutes in air. During the drying procedure at 100 °C, the coated electrode changed colour from light yellow to dark brown, indicating the formation of the perovskite film.

2.2. Materials synthesis

TiO_2 microvoids scattering layer

Polystyrene microspheres suspended in water (Duke Scientific, Thermofisher) were centrifuged at 7000 RPM for 3 hours. A buffer exchange from water to ethanol was carried out, the particles were then carefully re-suspended at low temperature using a low intensity ultrasonic probe to avoid damaging the particles by causing particles to aggregate. The re-dispersed particles in ethanol/water suspension were then centrifuged once more. The buffer exchange process was carried out three times to ensure minimal traces of water in the microsphere solution. Finally, the microspheres in ethanol were used to dilute commercially available Dyesol paste 18NR-T to the desired microsphere concentration and paste thickness.

PEDOT scattering layer

Microspheres mixed into a conductive polymer, PEDOT:PSS, are used as a back reflector. PEDOT:PSS (Clevios) is first filtered though 1 um PTFE filter. Filtered PEDOT is mixed at different volumetric ratios to microspheres in water.

Aluminium oxide paste synthesis

Aluminium oxide dispersion 10 wt% in water was washed by centrifuging at 7500 RPM for 6 hours and redispersing in absolute ethanol with an ultrasonic probe at a duty cycle of 50 % (2 seconds on, 2 seconds off) for a duration of 5 minutes. The washing process was repeated for three cycles. For every 10 g of the original dis-

persion (1 g total Al_2O_3) the following was added: 3.33 g of α-terpineol and 5 g of a 50:50 mix of ethyl-cellulose 10 cP and 46 cP in ethanol 10 wt %. After the addition of each component, the mix was stirred for 2 minutes and sonicated with the aforementioned sonication program for 1 minute. Finally, the resulting mixture was introduced into a rotary evaporator to remove excess ethanol in order achieve the required paste consistency suitable for doctor blading, spin-coating or screen-printing.

Organometal halide perovskite synthesis

Methylamine (CH_3NH_2) solution 33 wt% in absolute ethanol was reacted with hydroiodic acid (HI) 57 wt% in water with excess methylamine under nitrogen atmosphere in ethanol at room temperature. Typical quantities were 24 mL methylamine, 10 mL hydroiodic acid and 100 mL ethanol. Crystallization of methylammonium iodide (CH_3NH_3I) was achieved using a rotary evaporator; a white colored powder was formed indicating successful crystallization. Methylammonium iodide (CH_3NH_3I) and lead (II) chloride ($PbCl_2$) was dissolved in anhydrous N,N-Dimethylformamide at a 3:1 molar ratio of CH_3NH_3I to $PbCl_2$, to produce a mixed halide perovskite precursor solution. In spin-coated and dried films, the formed perovskite of methylammonium lead iodide chloride ($CH_3NH_3IPbCl_2$) had a final I to Cl ratio of approximately 2:1 as determined by energy dispersive x-ray analysis. The excess methylammonium iodide and chlorine is assumed to be lost via evaporation during the drying process.

2.3. Ultraviolet-visible spectroscopy

The Cary 300 is a double-beam, ratio-recording spectrometer. Radiation from the instruments source of illumination is split into two different beams: the sample beam and the reference beam. Each beam is interrupted periodically by means of a 'chopper', such that the integrating sphere is illuminated alternately by the two beams. At any given wavelength, the instrument records the ratio of the signal produced by

the detector when the sphere is illuminated by the sample beam to the signal produced by the detector when the sphere is illuminated by the reference beam. The Beer-Lambert law is defined as:

$$A = -\log \frac{I}{I_o} = -\log T = \epsilon c l$$

Where ϵ is the molar absorptivity, c is the molar concentration and l is the optical path length. The product of the molar absorptivity and molar concentration yields the absorption coefficient α.

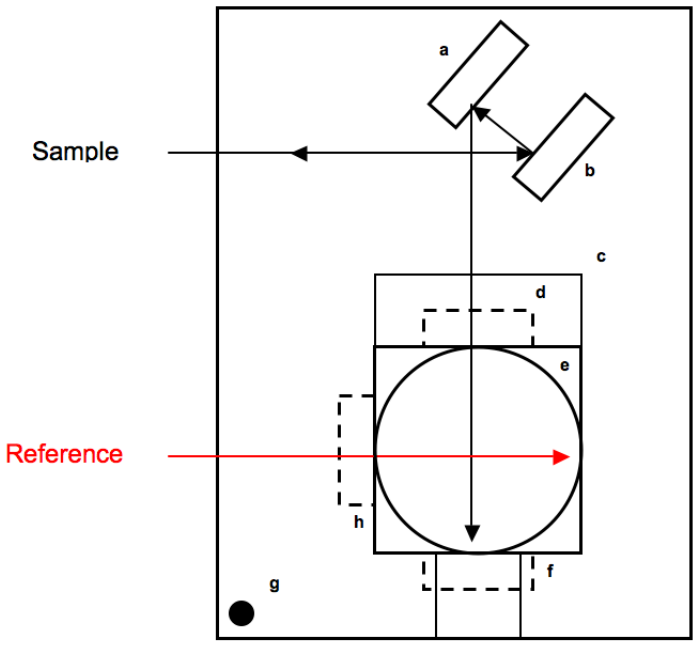

FIGURE 2.1. Schematic of Integrating Sphere Assembly a: Mirror M2, b: Mirror M1, c: PMT Module, d: Transmittance Port, e: 70 mm Spectralon Integrating Sphere, f: Reflectance Port, g: Locator Hole For Alignment Pin, h: Reference Beam Entrance Port

2.4. Optoelectronic characterisation

Current-Voltage characteristics were measured (2400 Series SourceMeter, Keithley Instruments) under simulated AM 1.5G sunlight at 100 mW.cm^{-2} irradiance;

generated using an AAB ABET technologies Sun 2000 solar simulator and calibrated using an NREL calibrated silicon reference cell with a KG5 filter to minimise spectral mismatch (the mismatch factor was calculated to be less than 1%). The solar cells were masked with a metal aperture to define the active area which was typically 0.09 cm^2 and measured in a light-tight sample holder to minimize any edge effects.

Photovoltaic action spectra were measured (2400 Series SourceMeter, Keithley Instruments) with chopped monochromatic light incident which were biased with white light-emitting diodes (LED) at an equivalent solar irradiance of 10 $mW.cm^{-2}$. The monochromatic light intensity for the incident photon-to-electron conversion efficiency (IPCE) was calibrated with a UV-enhanced silicon photodiode. The solar cells were masked with a metal aperture to define the active area which was typically 0.09 cm^2 and measured in a light-tight sample holder to minimize any edge effects.

2.5. Transient absorption

Photo-induced absorption (PIA) spectra were obtained from perovskite/TiO_2 or Al_2O_3 films deposited on FTO coated glass. The films were excited with an Argon ion laser tuned at 496.5 nm with a maximum fluence of 50 mW cm^{-2} and chopped at a frequency of 23 Hz. The detection is made with a continuous white light probe (halogen bulb) of around 1 sun intensity onto the sample. After passing through the sample, the probe beam enters a monochromator (SpectraPro-2300i, Acton Research Corporation) coupled to diode for detection in the visible (PDA10A, Thorlabs) and in the NIR (ID-441-C, Acton Research Corporation). Acquisition is made by a lock in amplifier locked at the light modulation frequency (SR830, Stanford Research Systems) and a NI USB-6008 (National Instruments) acquisition card. A computer running LabView (National Instruments) controls the setup and record spectra. No further

treatment is applied to the data.

3. Light-trapping strategies for thin-film photovoltaics

Light management is a major issue in solid-state dye-sensitized solar cells (DSC) due to the limited thickness of the active layer (2 μm). Solid-state DSCs of the highest efficiency presently employ organic-based sensitizers [14] which absorb strongly but across a narrow-band. By contrast ruthenium-based sensitizers absorb panchromatically but weakly, nevertheless photo-conversion efficiencies of over 5% have been reported for solid-state DSCs employing ruthenium-based sensitizers [15]. Optical enhancements are expected to increase the efficiency further. In this chapter we employ two new far-field photonic scattering strategies to enhance the light harvesting capabilities of dye-sensitised films and devices.

3.1. Light scattering via small particles

Light scattering is the redistribution of light in the non-specular direction. Scattering occurs upon an encounter with non-homogeneites or an obstacle. More precisely, light which is reflected diffusely is termed scattered light. Indeed, the measure of how much a system scatters light is given by the term 'haze' which is the ratio of diffuse reflectance upon specular reflectance.

Mie theory describes scattering from spherical particles with feature sizes comparable to sizes wavelength of light. In 1908, Gustav Mie demonstrated a computational approach of simulating light scattering by small spherical particles using Maxwell's electromagnetic theory. Mie applied this computational approach to simulating the colour effects connected with changing with diameter of the gold spheres in gold colloids [16].

The low opacity of nanocrystalline TiO_2 is due to the small size (around 10 - 30 nm) and the high packing density of the particles. Usami carried out Monte Carlo

simulations using solutions based on Maxwell's equation reporting that 99 % of the incident light at 600 nm penetrates a TiO_2 film of 30 nm without scattering [17]. The use of larger TiO_2 particles (250 - 300 nm) to scatter light was predicted by Ferber *et al.* They calculated that by using large titania particles at 5 wt% to 200 nm particles in absorption of 27 % could be achieved in a 10 μm thick film owning to additional spectral sensitivity in the near-infrared [18]. Incorporating a scattering layer of large disordered TiO_2 particles (figure 3.1) into the device architecture is now an established means of improving optical density [19]. Indeed, all prototypes that reach photo-conversion efficiencies greater than 10 % and recently 12.3 % make use of diffuse light scattering to maximise light harvesting [20, 21]. The increased light-matter interaction results in an extended effective optical path length; reflected light travelling along the plane of the active medium has a greater probability of being absorbed than light travelling normal to the plane. To date, scattering layers consisting of large titania particles have yet to be successfully integrated into the solid-state DSC due to film formation and pore-filling issues.

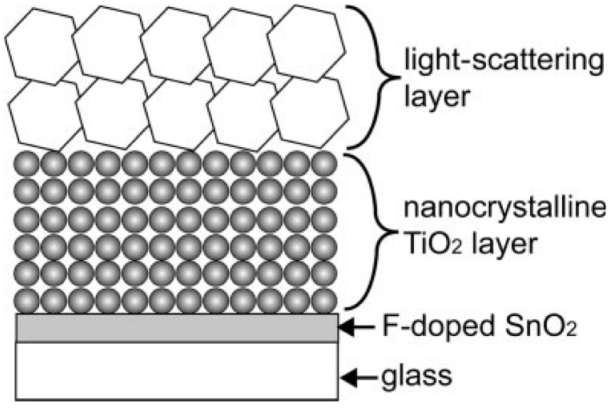

FIGURE 3.1. Schematic representation of a typical photo anode of a high-performance liquid electrolyte dye-sensitised solar cell incorporating a scattering layer (permission requested from [19])

3.2. Light scattering via micro-voids

To address issues of film formation and pore-filling we have taken an alternative approach to induce light scattering. We introduce spherical voids into the active layer causing light to scatter by creating a sharp transition in refractive index (between air: n = 1 and titania: n = 2.4) causing the incident light to refract. Snow consists of small ice crystals, or snowflakes, separated by small micro-voids of air, these micro-voids are close to the wavelength of light and consequently scatter light rather than transmit it, hence this is why a thin layer of snow on the ground is enough to hide the surface underneath. The additional benefit of creating a highly porous titania network may also lie in better pore-filling and film formation.

Enhanced light harvesting by spherical micro-voids have previously been demonstrated by Hore and co-workers [22, 23] in the liquid-state DSC but not the solid-state DSC. We embrace a similar approach of using sacrificial polymer microspheres mixed in the active layer which are then burnt off during film sintering, see figure 3.2. Our studies go into greater depth, elucidating an optimised structure through careful tailoring of layer thickness, void size and void concentration in order to maximise light absorption whilst maintaining the critical requirements of sufficient dye-loading and effective pore-filling of the solid-state hole-transporter medium.

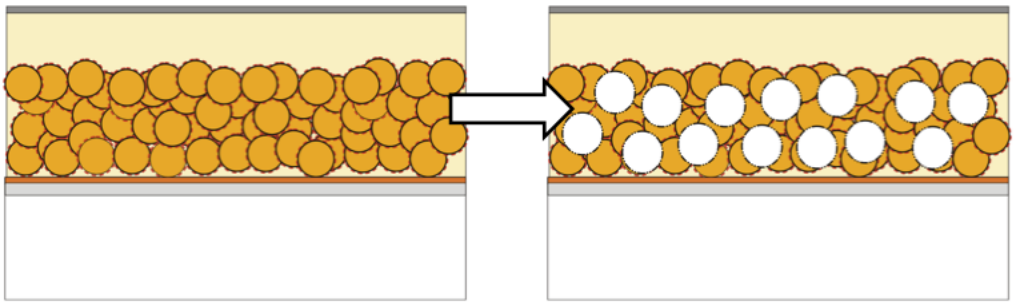

FIGURE 3.2. Schematic representation of a process to void making scattering layer; arrow indicates a sintering step.

Scattering film preparation Polystyrene microspheres suspended in water (Duke

Scientific, Thermofisher) were centrifuged at 7000 RPM for 3 hours. A buffer exchange from water to ethanol was carried out, the particles were then carefully re-suspended at low temperature using a low intensity ultrasonic probe to avoid damaging the particles by causing particles to aggregate. The re-dispersed particles in ethanol/water suspension were then centrifuged once more. The buffer exchange process was carried out three times to ensure minimal traces of water in the microsphere solution. Finally, the microspheres in ethanol were used to dilute commercially available Dyesol paste 18NR-T to the desired microsphere concentration and paste thickness.

Figure 3.3 shows a scanning electron micrograph (SEM) of a typical device incorporating a scattering structure, in the top-left panel we see a surface SEM of a scattering layer. The voids are regular in shape and size and there is no sign of aggregation between particles (this is due to thorough cleaning and thorough re-dispersion of the particles), the bottom-left panel shows a surface SEM of a standard Dyesol 18NR-T titania paste, the right-side panel shows a cross-sectional SEM of a typical device. Two phases of scattering and non-scattering layer can be clearly seen. There appears to be a sharp boundary between layers, this is due to the casting method. To create the double layer two processes of doctor-blade coating was applied: the first to create the transparent layer and second to create the scattering layer. Work by Ito *et al.* [24] show that the technique employed in processing multiple layers is significant: by repeated doctor-blade coating and drying using a TiO_2 colloidal paste, gaps and boundary layers between the repeated doctor-blade coated layers appear and micropore structures and cracks feature on the surface after sintering. Ito et al. further report that by spincoating multiple layers a homogeneous cross-section can be observed with no traces of boundary phases [24].

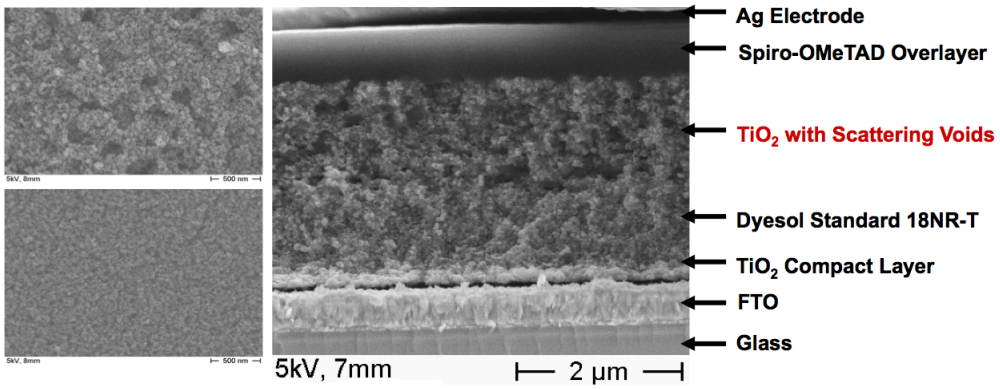

FIGURE 3.3. Scanning electron micrograph (SEM) of surface (left; top: voids, bottom: standard) and device cross-section (right)

3.2.1. Optical characterisation

Ultraviolet to visible spectroscopy with integrating sphere measurements are taken in order to determine the total transmittance, reflectance and thereby determine the absorption of different active layer architectures (see chapter 2.3), where absorption (A) = 1 - total transmittance (T) - total reflectance (R). Hence, the influence of the micro-voids on the light harvesting capability of the sensitised films can be probed. It is noted that there is additional light 'scattered' out of the sides of the device which appears as an absorption but should be better understood as a measurement error. For instance in figure 3.4 and this can be as high as 14 % of the incident light for strongly scattering films.

Micro-pore size Figure 3.4 shows calculated absorption of mesostructures with different sized pores from 60, 300, and 600 nm formed by using respectively sized microspheres (features sizes confirmed via scanning electron micrographs). The four panels from a) to d) show the evolution of a full device from a) TiO_2, b) TiO_2 with dye, c) TiO_2 with dye and hole-transporter, and finally d) TiO_2 with dye and hole-transporter (HTM) and silver electrode (final device structure). The similarity in

absorption for scattering structures with 60 nm and 600 nm pores illustrates the play off between dye-loading and light scattering: at 60 nm a structure with heavy dye-loading and low diffuse reflectance is obtained, whereas at 600 nm a structure with light dye-loading but high diffuse reflectance is obtained- the absorption is calculated to be roughly the same. From these measurements it is clear 300 nm is the optimum particle size.

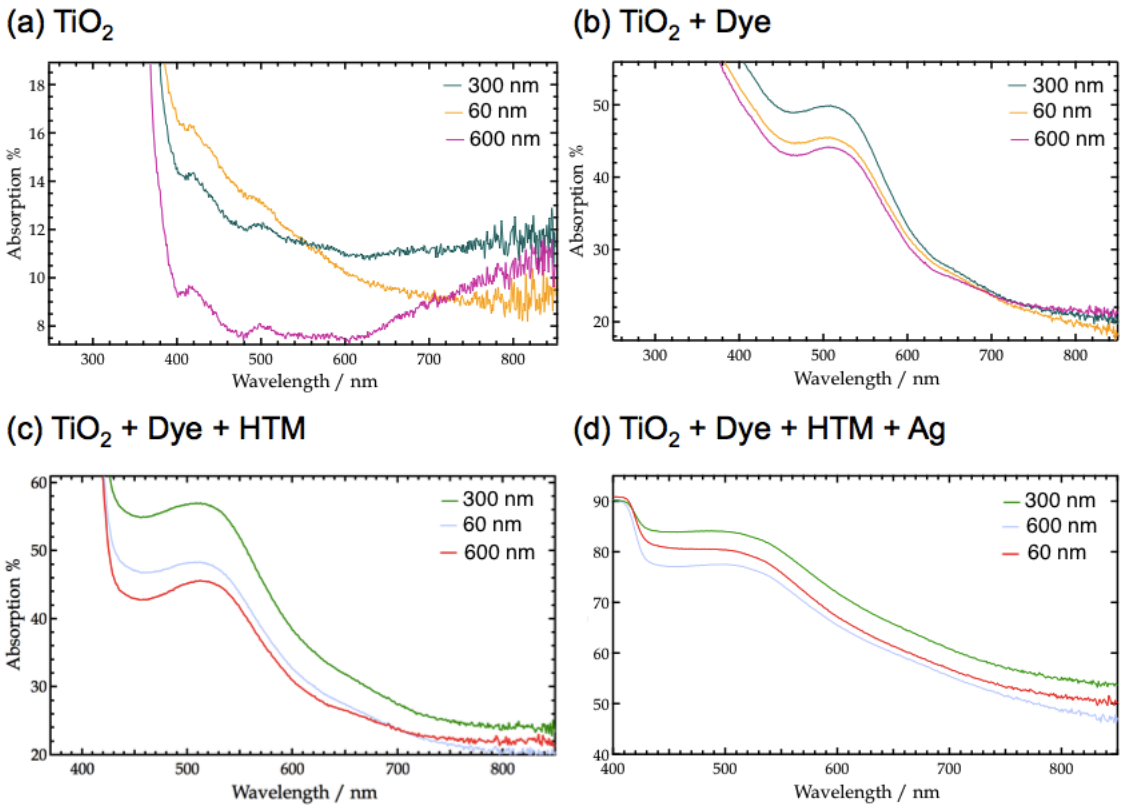

FIGURE 3.4. Optical characterisation of different pore sizes at 300 nm, 60 nm, and 600 nm. The ratio of spheres to paste was kept constant for all variations

Pore concentration and thickness the pore size as kept constant at 300 nm and the pore density was altered by varying the microsphere:paste ratio (0.66:1, 1:1, 1.32:1, v/v). The thickness was controlled by changing the spin coating speed for the layer. In figure 3.5 an increase in absorption with film thickness and with pore-density is observed. At the lowest density of voids for the thickest film and for the highest

density of voids for the thinnest film it appears the optical characteristics are very similar, indicating a balance between dye-loading and light scattering.

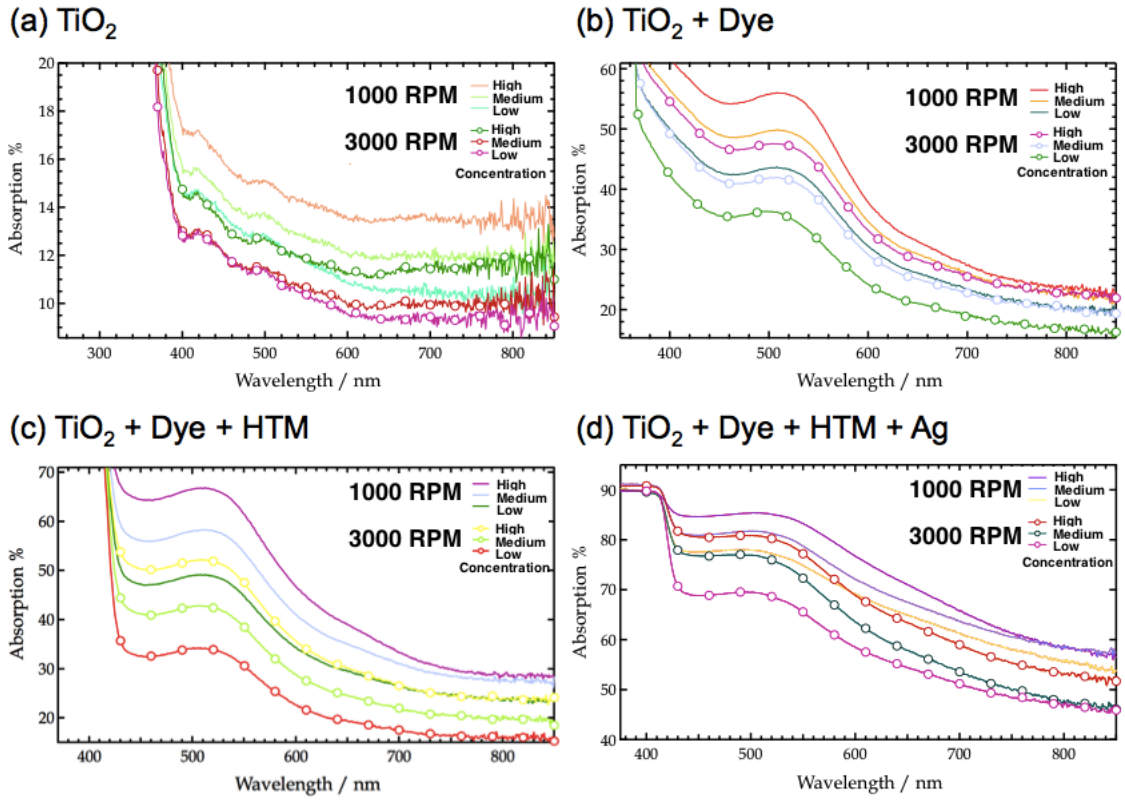

FIGURE 3.5. Optical characterisation of thickness against pore density. Traces with open circles are layers at fast speed therefore thinner structure, thicker layers are traces without open circles. The concentration of voids was changed within each thickness defined as low, medium and high, where 'high' relates to the maximum sphere concentration for good film formation (1.32:1)

Configuration of scattering layer The aforementioned optical characterisation has yielded an optimised scattering mesostructure with a thickness of 700 nm, with a pore-size of 300 nm and optimum pore density given by mixing 1.32:1 (v/v) 300 nm microspheres into commercially available Dyesol paste (DSL 18-NRT). In order to replicate the prototypical high-performance DSC device architecture the optimised scattering based on micro-voids on to a 1 μm thick layer of TiO_2 in lieu of a scattering layer of large disordered TiO_2 particles is applied. In figure 3.6 observe an

enhancement in light absorption through the application of the micro-void scattering layer is observed. Furthermore a 2 μm transparent film absorbs less than a 1 μm transparent film with a 700 nm 'scattering' layer, the implication here is that even with a thicker film with greater dye-loading the transparent films absorb less light. The majority of the enhancement is in the visible to near-IR tail of the spectra (550 nm onwards).

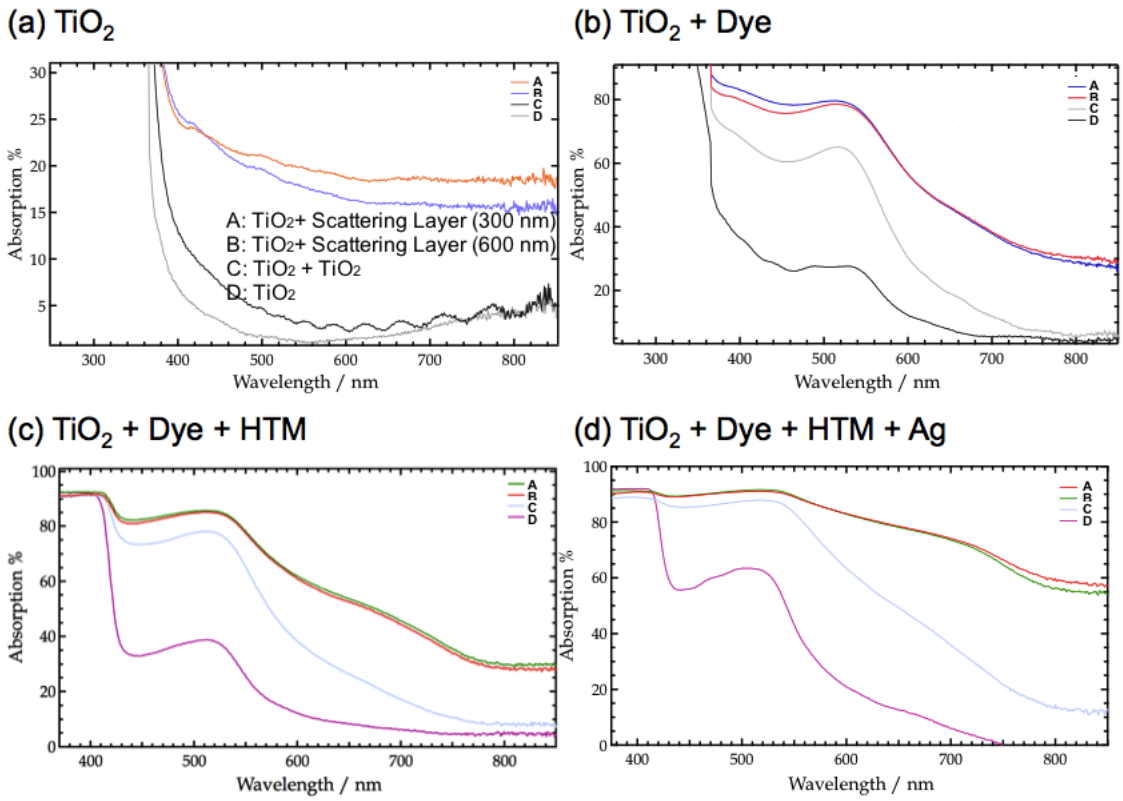

FIGURE 3.6. Optical characterisation of different structures. 1μm layer of TiO_2, 2μm layer of TiO_2, 1μm layer of TiO_2 with 0.7μm layer of 300 nm voids, 1μm layer of TiO_2 with 0.7μm layer of 600 nm voids

3.2.2. Optoelectronic characterisation

In this section devices (chapter 2.1.1) employing the optimised micro-void scattering layer are reported. Devices were characterised using current-voltage measure-

ments and incident-to-photon conversion efficiency (IPCE) measurements, JV and EQE measurements (chapter 2.4). Preliminary studies began with understanding the play off between surface area (i.e., dye-loading) and light scattering affected device performance. The results were promising, structures incorporating voids were found to be at least competitive with control devices in terms of photocurrent generation, indicating that light scattering can compensate for the loss in absorption due to lower dye-loading.

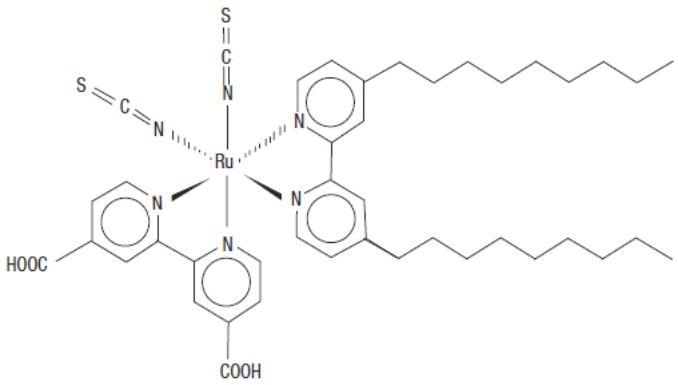

FIGURE 3.7. Molecular structure of Ruthenium-based dye-sensitiser, Z907. Permission requested from [25]

Devices incorporating optimised micro-voids employing Z907 as the sensitiser exhibit an increase in photocurrent from 7.1 mA/cm^2 to 10.6 mA/cm^2, figure 3.8(a), owing to enhanced spectral sensitivity in the near-IR evident from the incident-to-photon conversion efficiency (IPCE) spectrum measurements, figure 3.8(b). Furthermore, reflectance measurements of a completed device support optical scattering as the mechanism for enhanced photocurrent, figure 3.6(d) shows a large enhancement of absorption in the near infrared region. To our knowledge, 10.6 mA/cm^2 for low-extinction coefficient ruthenium-based sensitizer Z907 is the highest ever reported in the literature for solid-state dye-sensitized solar cells, figure 3.8 and table 3.1.

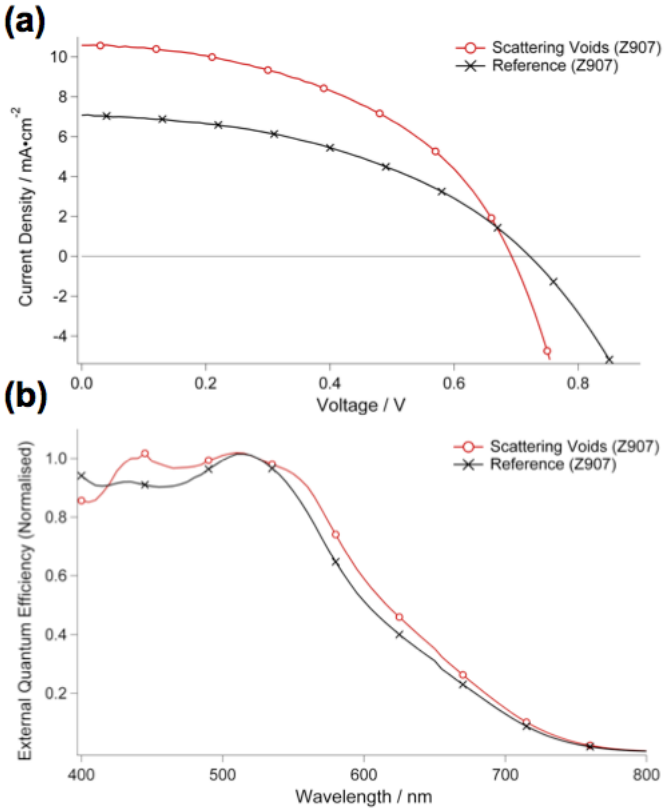

FIGURE 3.8. Optoelectronic characterisation of devices incorporating micro-void scattering layer using Z907 sensitiser

While high extinction organic dyes with narrow absorption profiles such as C220 [14] deliver impressive photo conversion efficiencies of 6.1%, photocurrent enhancements employing light scattering structures, see figure 3.9, indicate that the incorporation of optical enhancers are likely to advance the state-of-the-art for solid-state DSCs further owing to poor light-harvesting in the near-IR, figure 3.9. For both dye systems the open-circuit voltage is lower, it is possible that during film sintering the polystyrene has affected the surface properties of the titania. The fill factor has improved for both dye systems this could be indicative of better pore-filling in the hierarchical micro-to-nano assembly thus leading to lower series and shunt resistances. The key result is that even though the control films are thicker than scattering films the short-circuit current is enhanced.

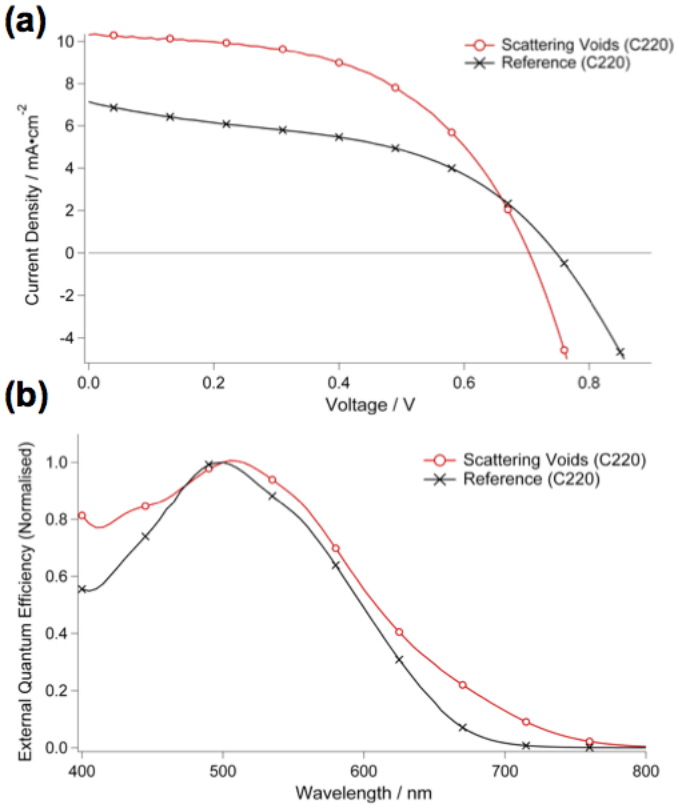

FIGURE 3.9. Optoelectronic characterisation of devices incorporating micro-void scattering layer using C220 sensitiser

Structure	Jsc (mA cm^{-2})	Voc (mV)	Fill Factor	PCE (%)	t (μm)
Z907 reference	7.07	720	0.44	2.23	2.6
+ Scattering voids	10.58	690	0.47	3.44	2.4
C220 reference	7.12	750	0.46	2.43	2.6
+ Scattering voids	10.31	700	0.53	3.84	2.4

TABLE 3.1. Best-in-class device performance for scattering and non-scattering structures with different dyes

3.3. PEDOT back reflectors

As well as employing microspheres within the TiO_2, it is possible to introduce a scattering effect at the rear of the cell. Here, microspheres mixed into a conductive

polymer, PEDOT:PSS, are used as a back reflector. PEDOT:PSS (Clevios) is first filtered though 1 μm PTFE filter. Filtered PEDOT is mixed at different volumetric ratios to microspheres in water. Figure 3.10, shows a scanning electron micrograph of a device employing a PEDOT:microsphere back reflector on top of a spiro-OMeTAD capping layer. The particles appear homogenous with little sign of aggregation. From the SEM we can confirm the thickness of the PEDOT:Microphere matrix to be around 1 μm.

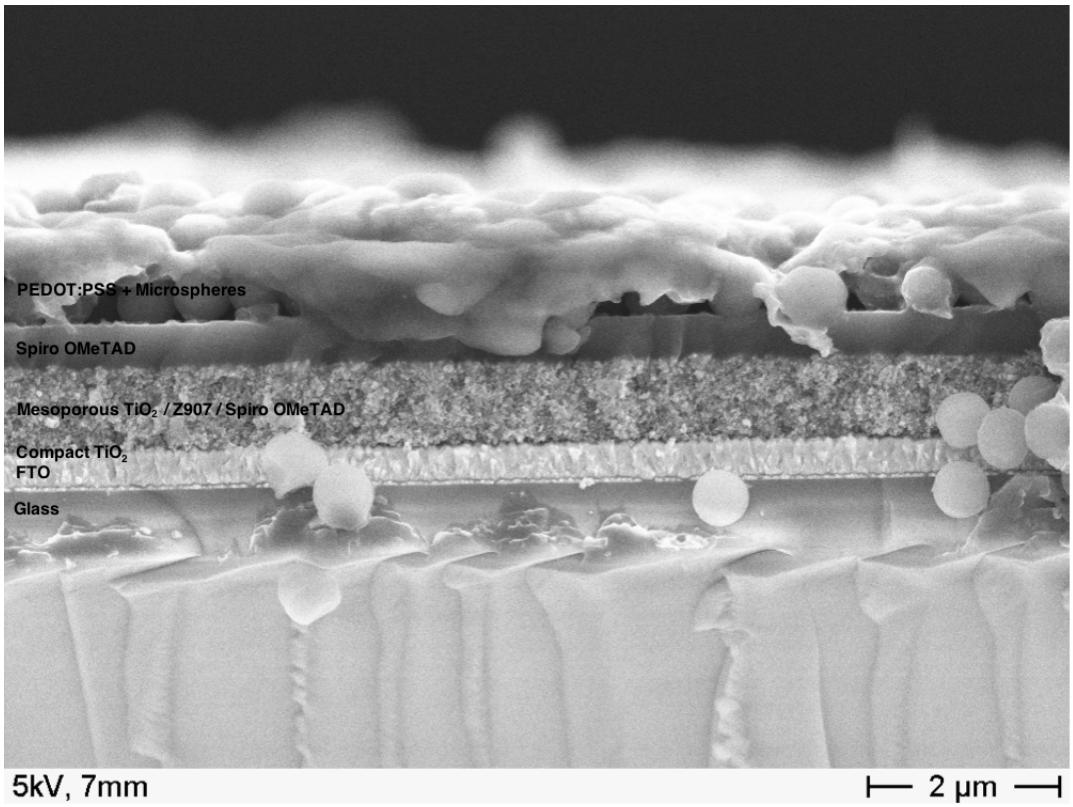

FIGURE 3.10. Scanning electron micrograph cross-section of typical device employing PEDOT:microsphere back reflector

3.3.1. Optical characterisation

Figure 3.12 shows UV-Vis absorptance measurements of PEDOT:microsphere blend at different volumetric ratios pre and post-annealing. An increase in absorbance

with the addition of polystyrene microsphere and with annealing is observed. The increase in absorptance is due to change in refractive index of local medium in which the microparticles were previously dispersed in. Figure 3.11, shows the effect on absorptance with increasing scattering layer thickness- it also shows that there is potential for multi-layer stacking which may open up new optical tools such as Bragg reflectors or dielectric mirrors.

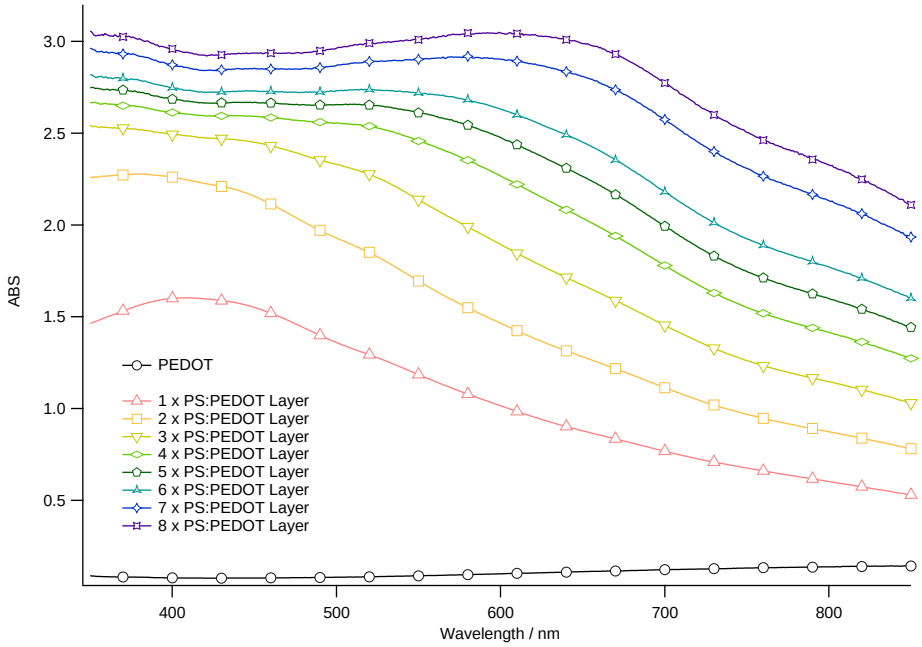

FIGURE 3.11. UV-Vis absorptance measurement of PEDOT:microsphere blends with multiple layers

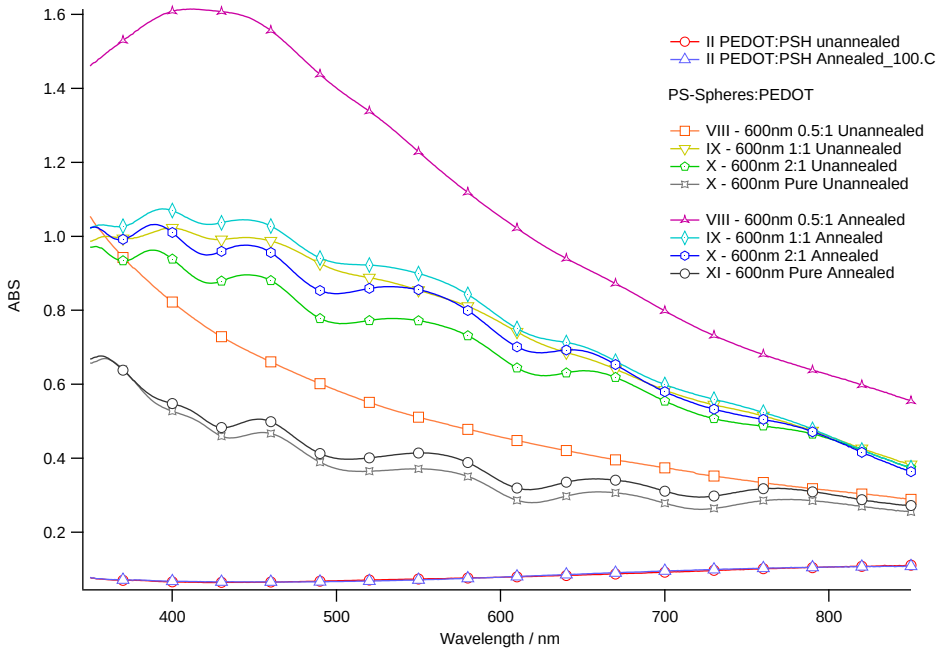

FIGURE 3.12. UV-Vis absorptance measurement of PEDOT:microsphere blends annealed and unannealed

Figure 3.13, shows reflectance measurements of films of optimised PEDOT:microsphere blends (at 1:2 v/v) with different sized microspheres from 0 (no spheres, just PEDOT), 60, 200, 300, and 600 nm. The greatest absorption is achieved by using 200 nm sized particles. The diffuse (non-specular) component is measured in figure 3.14, at 600 nm particle size the reflectance is almost completely diffuse and broadband making it an ideal scattering layer.

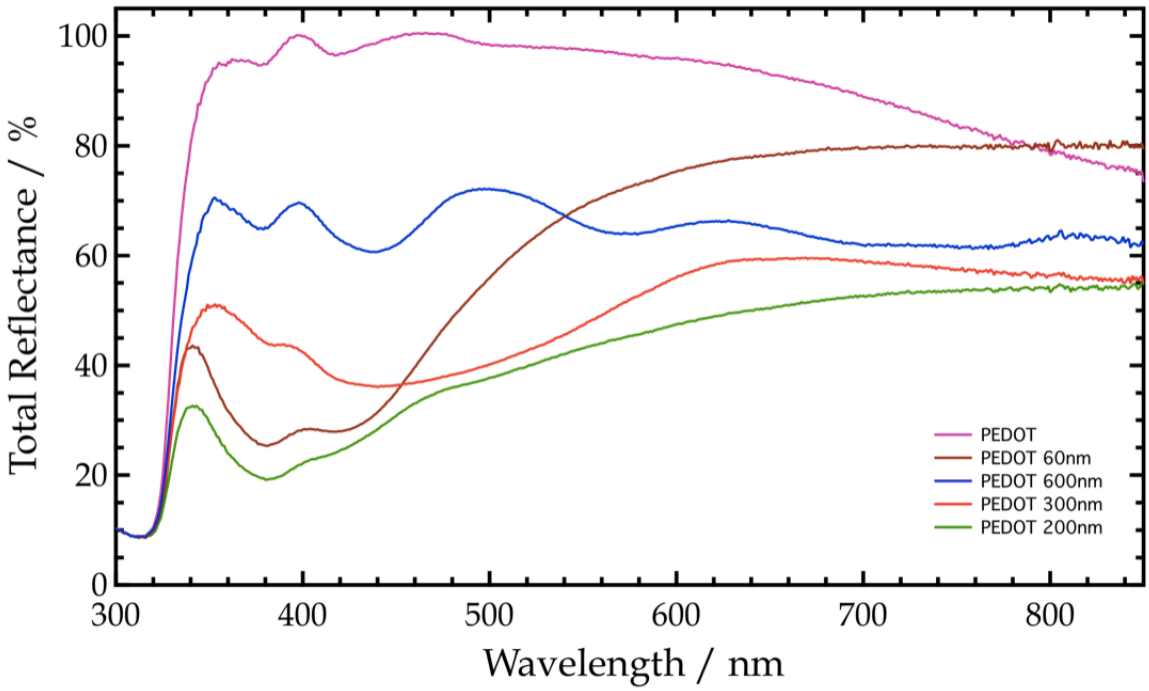

FIGURE 3.13. UV-Vis reflectance measurements taken using an integrating sphere for PEDOT:microsphere films coated on to glass with a Ag layer evaporated on top

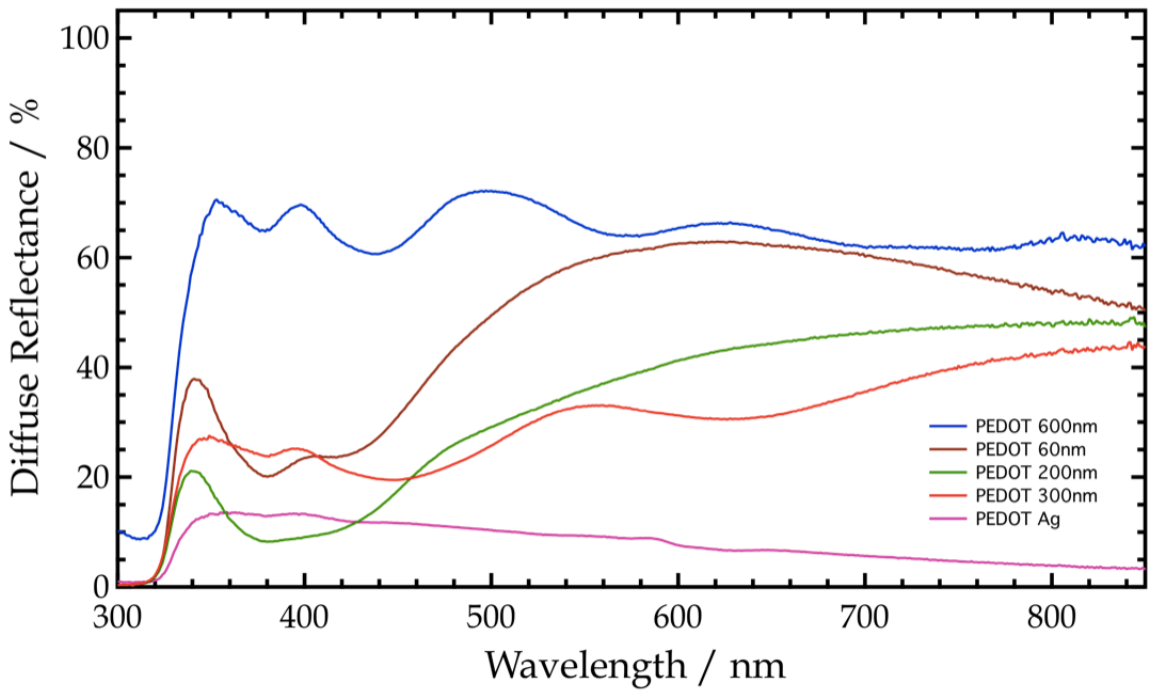

FIGURE 3.14. UV-Vis diffuse reflectance measurements taken using an integrating sphere for PEDOT:microsphere films coated on to glass with a Ag layer evaporated on top

3.3.2. Optoelectronic characterisation

In this section devices employing the optimised PEDOT:Microsphere scattering layer are fabricated and characterised.

Figure 3.15 shows IPCE for a device incorporating a PEDOT:microsphere scattering layer, the integrated short-circuit current is measured to be 11 mA/cm^2 for scattering structure and 7 mA/cm^2 for a standard reference. The enhancement in photocurrent is due to the broadband light scattering as can be seen in figure 3.15, it is one of the highest photocurrents ever measured on a dye-system with near unity external quantum efficiency if the reflectance of glass taken into account. Table 3.2 shows the average performance parameters of 32 devices of standard solid-state DSC and standard solid-state DSC with a back reflector. A systematic increase in

short-circuit photocurrent is observed, however a systematic decrease in open-circuit photovoltage and fill factor is also observed. Overall, the PCE does not improve since the gains in photocurrent are counterbalanced by the new loss-channels by incorporating the PEDOT:PSS scattering layer. The reason for this drop in open-circuit voltage and fill factor is likely to be an issue with the interface between the polymer, PEDOT:PSS, and the organic hole-transporter, spiro-OMeTAD. More work is needed to understand this problem; however, such complex interface engineering is beyond the scope of this thesis.

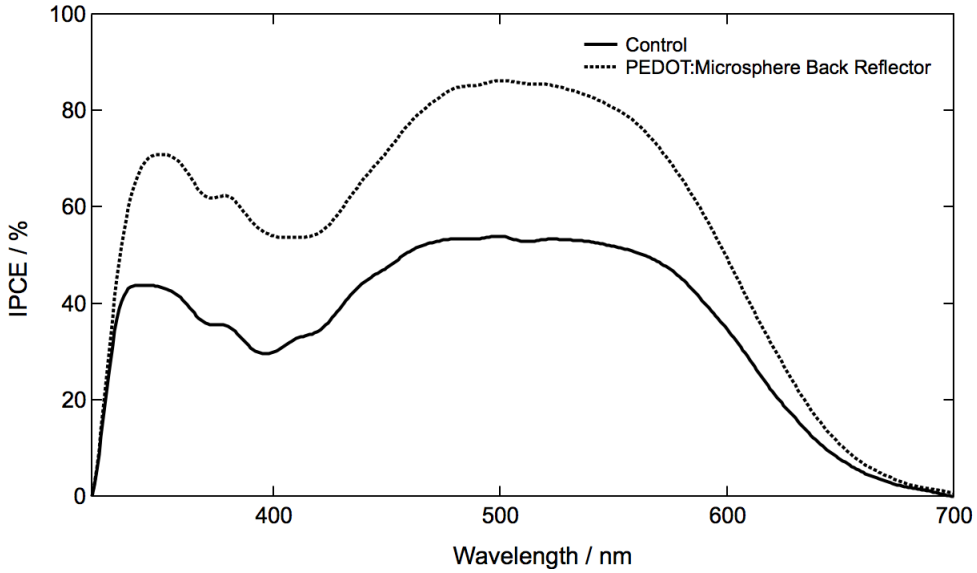

FIGURE 3.15. Incident-Photon-to-Electron Conversion Efficiency IPCE action spectra of devices with and without PEDOT:Microsphere scattering layer

Structure	Jsc (mA cm^{-2})	Voc (mV)	Fill Factor	PCE (%)
Standard	4.32 c.f. 7 (best)	850	0.75	2.8
+ PEDOT back reflector	6.51 c.f 11 (best)	740	0.60	2.9

TABLE 3.2. Current-voltage characteristics of solid-state DSCs with and without scattering layer averaged over 32 devices.

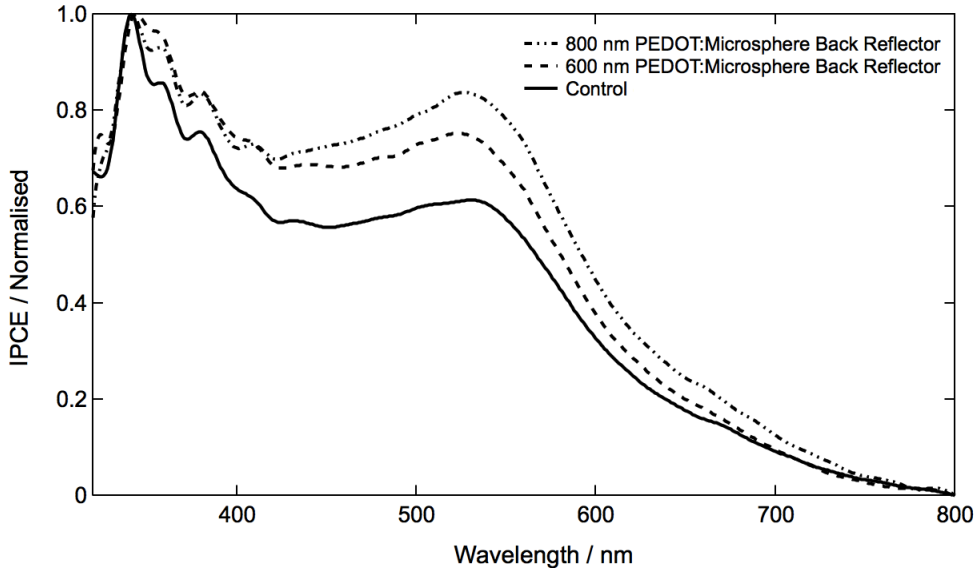

FIGURE 3.16. Normalise Incident-Photon-to-Electron Conversion Efficiency (IPCE) action spectra of devices with different sized sphere in the PEDOT:Microsphere scattering layer, showing 800 nm and 600 nm sized spheres with a standard control of no back scatterer

3.4. Summary

In this work a simple, scalable and low-energy method of increasing light collection in thin films is detailed, achieved by means of a light scattering layer comprising spherical micro-voids, resulting in structures which absorb more light even with lower dye-loading and maintain effective pore-filling through careful tailoring of layer thickness, void size and void concentration. The introduction of micro-voids in the active layer opens up new avenues of research beyond the control of light scattering such as studies into pore-filling, dye loading, high-viscosity or bulky hole-transporting materials and the functionalization of pores with other active components. PEDOT back reflectors have proven to be a very effective light scattering delivering near unity external quantum efficiencies. The key limitation to this system is the electronic contact between the polymer and organic molecule: more work is needed to understand and

better engineer this interface. Beyond new polymers and new scattering media (with altered refractive index), shape, size etc. new optical structures could be interesting. Preliminary studies showed that it was possible to stack multiple layers of PEDOT:x (where x is any material that will blend with PEDOT) this opens up opportunity to create interesting optical structures such as Bragg reflectors or dielectric mirrors. Due to the amorphous nature of PEDOT dispersion, it is unlikely to be able to form very ordered structures which may form the basis of 3D photonic crystal- though the concept of a self-assembled photonic crystal through wet-chemistry would be a target for future work.

4. Organometal Halide Perovskites

4.1. Background

Historically, the term 'perovskite' has two meanings: as a mineral calcium titanate ($CaTiO_3$) discovered by Gustav Rose in 1839 (named after Russian mineralogist Count Lev Aleksevich Perovski) and as a class of crystal structure topologically related to the mineral $CaTiO_3$ [26], see figure 4.1. Muller and Roy attempted to address this ambiguity in nomenclature by developing a formalism whereby square brackets enclosing $CaTiO_3$ would indicate a structural descriptor, i.e. [$CaTiO_3$]; without would indicate the mineral [27]. Such notation has not attracted widespread usage. In this report we apply the term perovskite as a structural descriptor.

4.2. Crystal structure

The archetypal perovskite crystal structure adopts the formulation ABX_3, where 'A' is a large cation coordinated to twelve 'X' anions, and 'B' is a smaller sized cation (relative to the 'A' cation) coordinated to six 'X' anions. It is perhaps simpler to visualise the structure in a body-centered cubic configuration where 'A' cations are located in the corner sites (0, 0, 0), 'B' cations at the body-center ($\frac{1}{2}$, $\frac{1}{2}$, $\frac{1}{2}$), and the 'X' anions in the faces (0, $\frac{1}{2}$, $\frac{1}{2}$) , ($\frac{1}{2}$, 0, $\frac{1}{2}$), ($\frac{1}{2}$, $\frac{1}{2}$, 0) of the cube [29, 30, 28, 26], see figure 4.2.

4.3. Distortion in perovskites

A crystal comprising of infinite three-dimensional array of corner-sharing BX_6 octahedra can be stable provided bonding requirements are met, an example is rhenium

FIGURE 4.1. Photograph of calcium titanate, $CaTiO_3$ permission requested from [28]

trioxide (ReO_3). Generally speaking, bonding within the octahedral framework is not stable thus another cation, 'A' , is introduced into cavity to address the charge balance [31]. The key proviso for the 'A' cation is that it must be large since a smaller cation will cause the structure to collapse and form a more densely packed alternative [31]. More formally Goldschmidt sets a tolerance factor, t, in equation 4.1 to determine the degree of distortion in an ABO_3 perovskite structure [32].

$$t = \frac{r_A + r_O}{\sqrt{2}(r_B + r_O)} \tag{4.1}$$

Where R_A is the ionic radius of the 'A' cation, R_B is the ionic radius of the 'B'

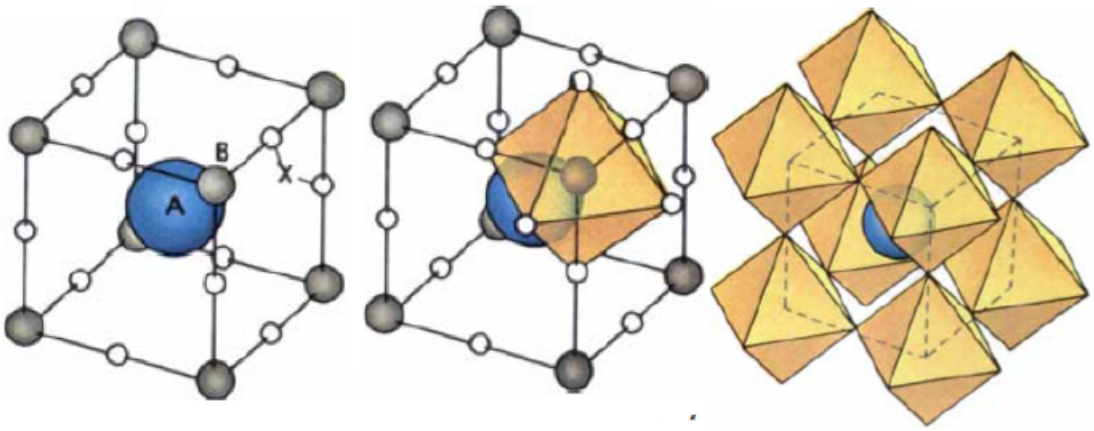

FIGURE 4.2. Unit cell representation of the perovskite structure permission requested from [28]

cation, and R_O is the ionic radius of the 'O' anion. Where the tolerance factor is close to 1 the perovskite adopts an ideal cubic structure, where the tolerance factor is less than 0.81 and the 'A' cation is smaller than the ideal size the BO_6 octahedra will tilt in order to "fill" space. Stable perovskite structures lie within $0.78 < t < 1.05$.

4.4. Scientific and technological significance of perovskites

Perovskites fascinate from a technological and scientific perspective. Earth's most abundant mineral is widely believed to be of perovskite from where a major constituent of the Earth's lower mantle (representing half of the planet's bulk) may be enstatite, ferrosilite (Mg, Fe)SiO_3 [33], see Figure 4.3. Experimental studies on the conversion of ilmenite to perovskite under pressures of 250 kbars and temperatures of 1000-1400°C (thereby replicating conditions close to the lower mantle) strongly support that entatite may be the most abundant mineral on Earth [34].

Perovskites both natural and synthetic exhibit a staggering array of properties. Perovskites run the gamut of electronic properties from insulators, semiconductors,

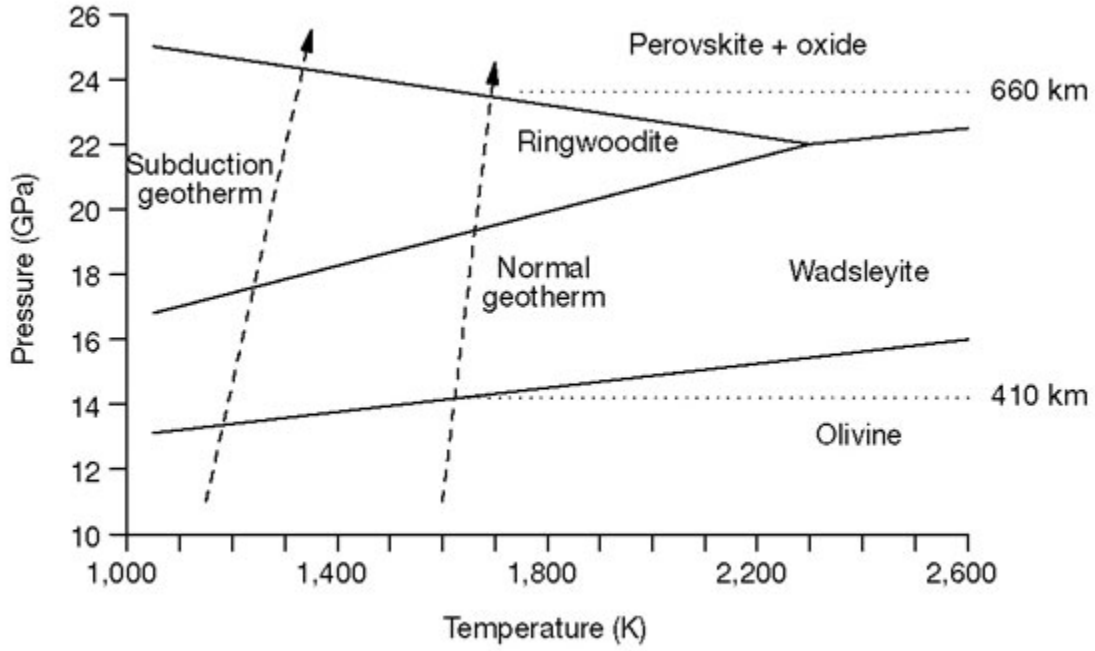

FIGURE 4.3. Schematic phase diagram of Mg_2SiO_4 olivine in mantle peridotite. Solid lines show the phase stability regions for olivine, wadsleyite, ringwoodite, and perovskite + oxide. Dashed lines show approximate temperature increase with depth in the mantle and inside a subduction zone. Cooler temperatures in subduction zones move the phase transitions either to shallower depths (olivine wadsleyite) or deeper depths (ringwoodite) perovskite + oxide permission requested from [35]

conductors, super-ionic conductors, and high-temperature superconductors for which Mueller and Bednorz won the Nobel Prize in Physics in 1987 [36]. The lanthanum barium copper oxide (LaBaCuO, or LBCO) perovskite [36] revolutionised the field of superconductors whereby superconductivity could be induced at 77 K (the boiling point of liquid N_2) negating the need for expensive coolants such as liquid He, hence a new field of high-temperature superconductivity was created. Efficient water splitting has been reported with lanthanum-doped sodium tantalate (La-$NaTaO_3$), the difference between the valence band (localised on the 2p oxygen orbitals) and the conduction band (localised on the 5d Ta orbitals) was reported to be 4.0 eV. Stronium

titanate ($SrTiO_3$) is an excellent example of a classic ceramic insulator where all the atomic sites are filled with strong ionic bonds holding atoms and electrons tightly in place. To illustrate the versatility of the perovskite structure, if Ti is substituted with its neighbour on the right in the periodic table (vanadium, V) then a superfluous d-electron is in residence thus the perovskite becomes conducting. As previously mentioned valance bands arise from the anion (oxygen) p-states and conduction bands arise from 'B' cation (metal) d-states, with this in mind the function of the 'A' cation is to simply donate electrons to these bands. This can be illustrated by considering tungsten trioxide (WO_3) an insulator with no other cations present, if lithium is added as a cation to the structure to produce $LiWO_3$ then metallic conductor is formed since Li is forced to occupy the conduction band. Indeed, the amount of Li added (relative to the other compounds) enables considerable control of the electronic properties- this family of materials are known as tungsten bronzes [37].

At elevated temperatures (200 °C) barium titanate would form into a cubic structure [38]. The cubic structure sets rather strict dimensional requirements, i.e. in terms of precisely what atoms might fit into the cage since the only parameter that can be varied is the lattice constant. The fact that the perovskite structure is not cubic at room temperature means a wider selection of atoms may accommodate the cage in different distortions and tilts; the resultant orientation is of critical importance to applications relating to dielectrics and ferroelectrics. There are essentially two ways to modify the perovskite structure: if the 'B' cation is too small this will cause an 'off-centre' tilt and if the 'A' cation is too small this will cause the octahedral framework to tilt thus reducing the effective size of the central cavity. When the 'B' cation no longer resides at the centre of the octahedra the symmetry reduces from cubic, to tetragonal or orthorhombic, and even sometimes triclinic. The result is the centre of positive charge is no longer at the same place as the centre of gravity for the surrounding negative charges thus the crystal is polarized, figure 4.4. If an electric field is applied the orientation of the titanium ions shift toward the negative

charged electrode causing the crystal to physically distort- this effect is known as piezoelectricity. The converse is also true, i.e. deforming the crystal mechanically will result in the relative distances of the charges to change thus represent a shift in potential. It is clear that disrupting the careful balance among various interatomic forces results in piezoelectric behaviour and when coordinated in unison, i.e., where the displacements are aligned parallel to each other, such phenomena may be applied to a variety of microelectromechanical systems (MEMS) or nanoelectromechanical systems (NEMS).

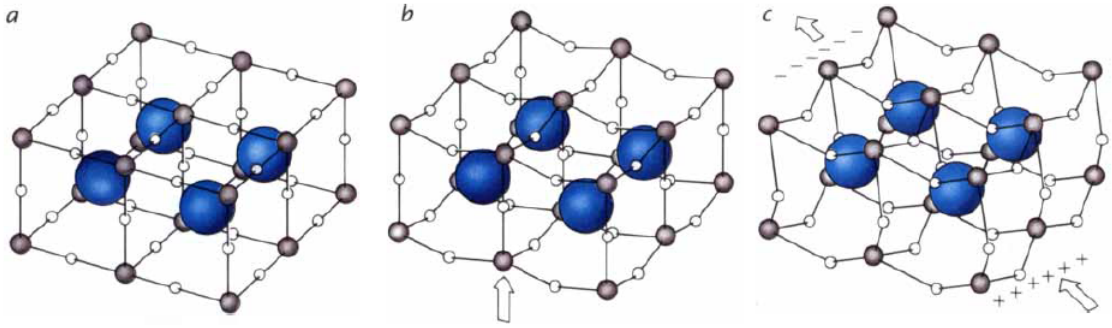

FIGURE 4.4. Barium titanate conforms strictly to the standard ABX_3 formulae but deviates slightly from the cubic structure (a) titanium cation is slightly off centre, (b) crystal becomes polarised. When an electric field is applied (c) the orientation of the titanium cation shifts towards the negatively charged electrode hence a further distortion in the crystal lattice.

One avenue of discourse I have not ventured into (since it is far too vast for the remit of this thesis) is the phenomena of magnetism in perovskites. The study of magnetism in perovskites is just as rich and full of intrigue as any other phenomena previously discussed. Perovskites have been applied in such uses as colossal magnetoresistance, charge ordering, spin dependent transport, spintronics. Figure 4.5 shows an overview of perovskites in many applications.

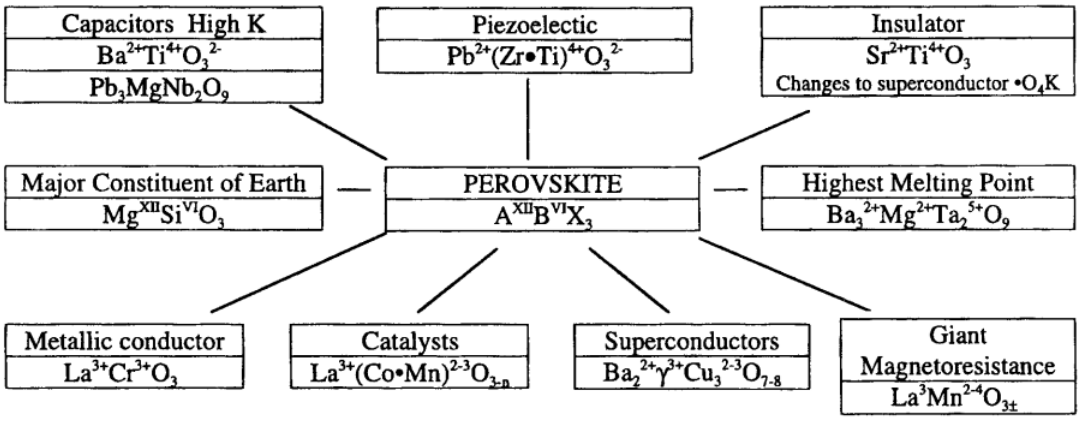

FIGURE 4.5. The many talents of perovskites. Permission requested from [39].

4.5. Inorganic-Organic perovskites

The principal aim of a composite is that the sum of its parts is greater than the effects of its constituents. There are many examples in nature where a combination of organic-inorganic material is beneficial [40, 41, 42]. The perovskite framework enables the combination of functional organic and inorganic components to exist in a neat molecular composite. Organic materials typically boast versatility in manufacture through solution-based processing, ease of tunability, structural diversity including plastic mechanical properties, high fluorescent efficiency, and large polarizability. However, organics are generally hindered by low room-temperature mobility, and this in turn sets upper limits on overall performance. This results from the weak van der Waals interactions between bonding adjacent molecules [43]. Furthermore, poor thermal stability raises issues for long-term device performance. Inorganic materials, however, are generally more stable at a range of temperatures and mobilities are generally very high owing to strong covalent bonds. It is also important to note that morphology may play an even more critical role in determining the performance of materials, as an example the mobility of amorphous silicon is 1 cm^2/Vs whereas crystalline silicon is 1000 cm^2/Vs. The essence of a device engineer lies in his abil-

ity to find ways to accentuate the positive and understate the negative features of a given material, the perovskite structure provides the opportunity to select a host of elements and apply them this precise manner. Beyond technological applications, however, from a purely academic standpoint these hybrid systems are interesting to study for novel phenomena found at the inorganic-organic interface. Takada *et al.* first introduced the concept of organic-inorganic superlattice in 1992, where photoconductive gain of 40-fold compared to that of single component copper phthalocyanine was observed when organic-inorganic multilayers of copper phthalocyanine and TiO_x were evaporated with a periodicity of 50 Åand above, forming a modulated electronic structure analogous to a type-II quantum well [44], see figure 4.6.

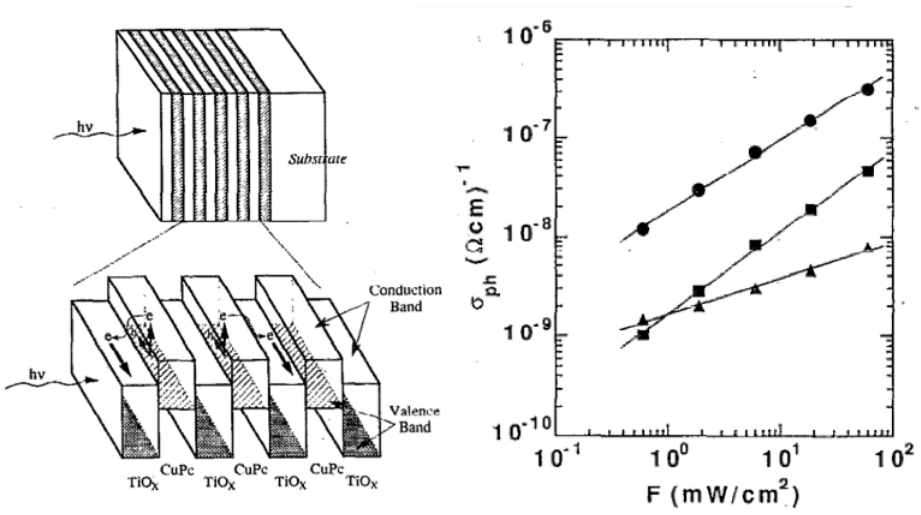

FIGURE 4.6. Schematic of device structure and energy landscape for Copper Phthalocyanine/TiO_x (left) with photoconductivity as a function of light intensity (right). Triangles are single layers of copper phthalocyanine, squares are multilayers with periodicity of 200 Åand circles are 400 Å. Permission requested from [44].

For the organic-inorganic hybrid perovskite a typical configuration consists of corner sharing MX_6 octahedra separated by A^+ cations, where M is any divalent metal (Cu^{2+}, Ni^{2+}, Co^{2+}, Fe^{2+}, Mn^{2+}, Cr^{2+}, Pd^{2+}, Cd^{2+}, Ge^{2+}, Sn^{2+}, Pb^{2+}, Eu^{2+}, or Yb^{2+}), X is some halogen (F, Cl, Br, or I), and A is some organic component with a terminating ammonium head cation (alkyl substituted R-NH_3^+ or 2-substituted

phenethylammonium [45]). Distortions from the ideal perovskite structure (in M-X-M bond angle and equatorial M-X bond distances) occur due to the steric hinderance and position of the organic cation. Such distortions will change the unit cell size, thus can result in optical bandgap shifts as much as 2 eV [46, 47]. Indeed, seminal work by Era and Mitzi champion the layered perovskite based on organometal halides as worthy rivals to more established materials, demonstrating excellent performance as light-emitting diodes [48, 49] and transistors with mobilities competitive with amorphous silicon [50].

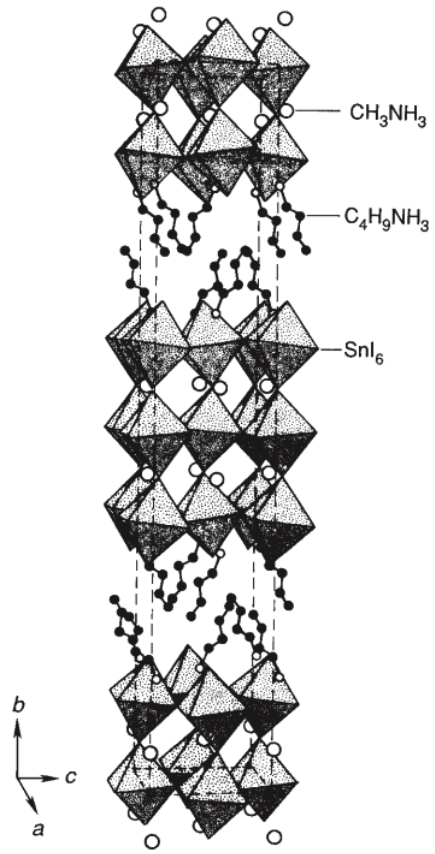

FIGURE 4.7. Schematic representation of a hybrid organic-inorganic perovskite. Permission requested from [51].

4.5.1. Organometal halide perovskite synthesis

In the following part of this chapter I describe the solution based synthesis for a range of perovskites in order to understand their optical properties. Methylamine (CH_3NH_2) solution (33 wt% in absolute ethanol) was reacted with hydroiodic acid (HI) (57 wt% in water) with excess methylamine under nitrogen atmosphere in ethanol at room temperature. Typical quantities were 24 mL methylamine, 10 mL hydroiodic acid and 100 mL ethanol. Crystallization of methylammonium iodide (CH_3NH_3I) was achieved using a rotary evaporator; a white colored powder was formed indicating successful crystallization. Methylammonium iodide (CH_3NH_3I) and lead (II) chloride ($PbCl_2$) was dissolved in anhydrous N,N-Dimethylformamide at a 3:1 molar ratio of CH_3NH_3I to $PbCl_2$, to produce a mixed halide perovskite precursor solution. In spin-coated and dried films, the formed perovskite of methylammonium lead iodide chloride ($CH_3NH_3IPbCl_2$) had a final I to Cl ratio of approximately 2:1 as determined by energy dispersive x-ray analysis, see figure 4.8. The excess methylammonium iodide and chlorine is assumed to be lost via evaporation during the drying process, however understanding this process is area of research beyond the scope of this thesis. The choice of acid and lead (II) halide can be changed to produce different perovskites. Table 4.1 shows all the lead-based perovskites formed and table 4.2 show all the tin-based perovskites formed over the duration of this thesis. It should be noted that all perovskites were mixed at 3:1 (methyl ammonium to metal halide) by molarity to ensure good solubility.

The choice of solvent depends on the selection of organic cation and metal halide. First, the solvent must dissolve both organic and inorganic components, without decomposition or with coordinating too strongly the metal cation [52]. I find that N,N-Dimethylformamide (DMF) and gamma-butyrolactone (GBL) are the appropriate solvents to dissolve methylammonium-halides with lead(II) halides. It is important to dissolve the organic component first to aid solvation of the metal component. Our

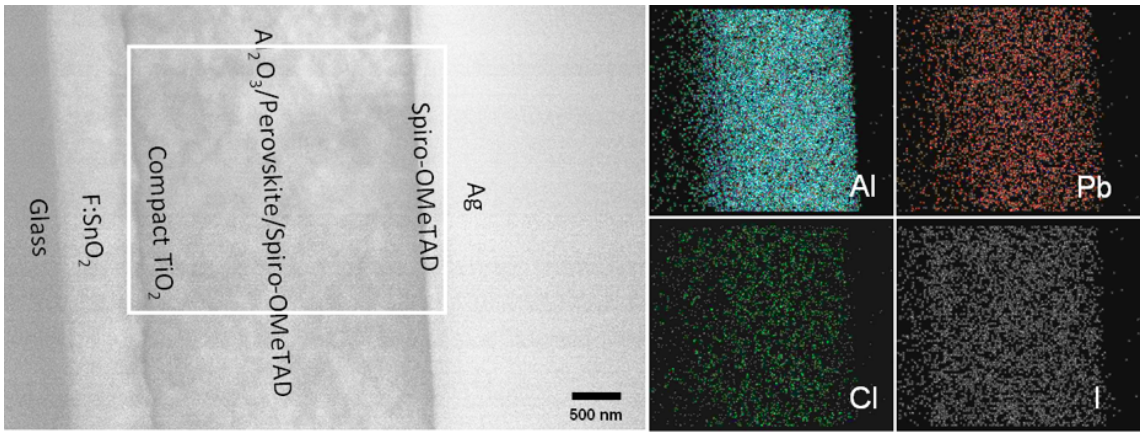

FIGURE 4.8. Cross-sectional scanning electron micrograph (SEM) of a 3 μm thick device (left), and energy-dispersive x-ray (EDX) spectroscopy with elemental mapping of (right) aluminium, lead, chlorine, iodine.

Perovskite	Methyl ammonium-X	Lead halide-X_2	Formability
Yellow Perovskite	CH_3NH_3-Br	Br_2	Y
YP-Iodine doped	CH_3NH_3-Br	l_2	Y
YP-Chlorine doped	CH_3NH_3-Br	Cl_2	Y
Black Perovskite	CH_3NH_3-I	l_2	Y
BP-Chlorine doped	CH_3NH_3-I	Cl_2	Y
BP-Bromine doped	CH_3NH_3-I	Br_2	Y
Violet Perovskite	CH_3NH_3-Cl	Cl_2	N
VP-Bromine doped	CH_3NH_3-Cl	Br_2	N
VP-Iodine doped	CH_3NH_3-Cl	l_2	N

TABLE 4.1. Formability of Pb-based perovskites

solvent of preference is DMF since it has a lower boiling point therefore more suited to processing at low temperatures. According to work by Mitzi [53], for alkylammonium and phenethlammonium lead(II) iodides, acetone and methylethylketone reportedly yield good films. The fluid properties of the solvent are important characteristics to ensure the formation of homogeneous films. Viscosities should be low and liquid-substrate interactions should be carefully considered to ensure even, reproducible coating. Finally, if sequential deposition is needed then the solubility of the solution has to be controlled carefully.

Perovskite Code	Methyl ammonium-X	Tin halide (SnY_2)	Formability
S1	CH_3NH_3-I	Cl_2	N
S2	CH_3NH_3-Br	Cl_2	N
S3	CH_3NH_3-Cl	Cl_2	N
S4	CH_3NH_3-I	F_2	Y
S5	CH_3NH_3- Br	F_2	Y
S6	CH_3NH_3-Cl	F_2	N

TABLE 4.2. Formability of Sn-based perovskites

4.5.2. Challenge to stablise perovskites for air processing / Optical Studies

The ability to produce solar cells in ambient conditions, i.e. without the need of controlled environments such as N_2 glove boxes, is one of the tenets of low-cost photovoltaics. For organic-inorganic perovskites it has been found that the stoichiometry of organic to inorganic components is important for long term stability in air. Further, it has been reported that for the group 14 (IVA) metal halides, divalent rare earth metal halides as well as some of the transition metal halides oxidation or absorption of water is a problem and control over the atmosphere is essential for forming high-quality films [52].

Different organic to inorganic (methyl ammonium to lead(II) halide) ratios were studied to elucidate its effect on the stability of the perovskites formed. Solutions of the methyl ammonium plumbate pure-iodide perovskite were mixed at 20 wt % using organic to inorganic ratios of: 1:1, 3:1, 5:1 and 8:1 (organic : inorganic). Spinning the solutions at 1500 RPM for 30 seconds on microscope slides and annealing at 100 °C for 45 minutes formed perovskites having a colour gradient from grey to red with increasing organic content. Left unsealed in air the 8:1 methyl ammonium plumbate pure-iodide perovskite bleached in less than two minutes. After two hours the 5:1 composition had done the same and when left over night all methyl ammonium plumbate pure-iodide perovskites lost their colour. Degradation occurring faster with higher the organic content in the perovskite can most likely be attributed to organic

chains in the A cation being weak against moisture [54].

To be able to directly compare the effect of halide composition on the properties of the perovskite formed the methyl ammonium plumbate mixed-halide perovskite and the methyl ammonium plumbate pure-iodide perovskite should have the same organic to inorganic molar ratio. The optical experiment conducted above indicated that the 3:1 organic to inorganic ratio pure-iodide perovskite is stable enough for processing in air (approximately two hours stability needed). To confirm this, an ultraviolet-to-visible spectroscopy study was conducted over 800 minutes. The UV-Vis absorbance spectrum of the pure-iodide perovskite is observed to be nearly flat across visible light (390–750 nm). This is the ideal spectrum for building integrated photovoltaics (BIPV), allowing the absorption of a fraction of light while leaving the colour spectrum unchanged. Furthermore, Figure 4.9 clearly shows that the methyl ammonium plumbate mixed-halide perovskite is far more stable than the methyl ammonium plumbate pure-iodide perovskite, its peak absorbance not deteriorating at all over time. Figure 4.10 shows stable to prolonged light exposure, as demonstrated by 1000 hours of constant illumination under simulated full sunlight. The absorbance of the film at 500 nm remained around 1.8 throughout the entire measurement period (absorbance of 1.8 corresponds to 98.4% absorption). The introduction of chlorine into the perovskite appears to have a stabilising effect. Nonetheless, over ninety minutes the methyl ammonium plumbate pure-iodide perovskite also showed no deterioration and is therefore stable enough to be processed in air before being sealed in the device. Having established a stable composition, the mixed-halide and pure-iodide perovskites studied in the subsequent experiments are always mixed at a 3:1 organic-inorganic ratio. In order to determine the nature of the band gap (direct or indirect) of the organometal halide perovskite, the absorption coefficient, α, was extracted from absorbance data. The absorption coefficient was then plotted square rooted against photon energy to reveal an indirect band gap, see Figure 4.11.

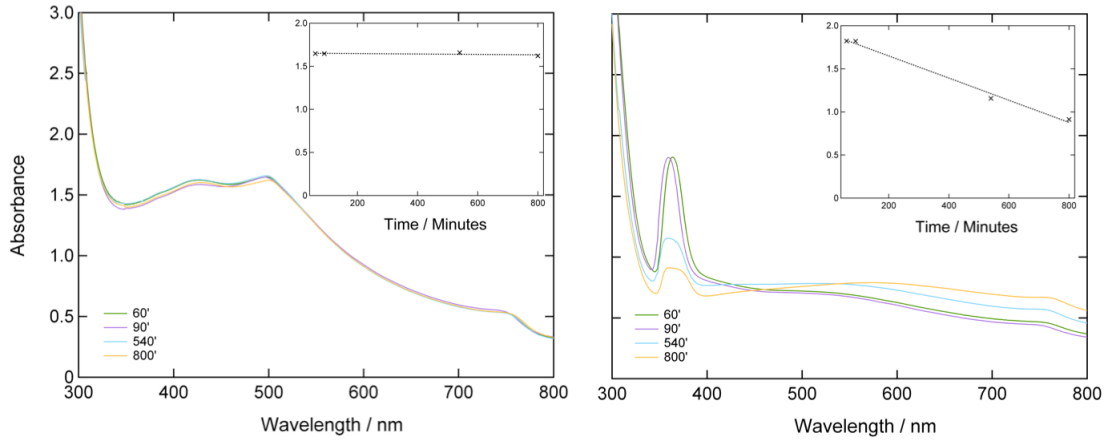

FIGURE 4.9. Optical Ultraviolet-to-Visible (UV-Vis) spectroscopy of 3:1 (organic:inorganic) mixed-halide perovskite (left) and 3:1 (organic:inorganic) pure-iodide perovskite (right). Inset for both plots shows peak absorbance over time. Measurements taken by Leonie Vogt.

4.5.3. X-ray diffraction of mixed-halide perovskite

Our preliminary x-ray diffraction analysis for $CH_3NH_3PbI_2Cl$ prepared on glass (see figure 4.12) showed diffraction peaks at 14.20°, 28.58°, and 43.27°, which are assigned as the (110), (220), and (330) planes, respectively, of a tetragonal perovskite structure with lattice parameters a = 8.825 Å, b = 8.825 Å, c = 11.24 Å, similar to the $CH_3NH_3PbI_3$ previously reported [55]. The extremely narrow diffraction peaks suggest that the films have long-range crystalline domains (>200 nm, peak width limited by instrument broadening) and are highly oriented with the a axis self-assembly [55, 54].

Wasylishen and co-workers reported rapid re-ordering motions of $CH_3NH_3^+$ by variable temperature nuclear magnetic resonance (NMR). The work revealed two phase transitions following a decrease in temperature as a consequence of progressive ordering of the $CH_3NH_3^+$ ions. Therefore, $CH_3NH_3^+$ cation cannot be assigned in the using X-Ray diffraction given its dynamic orientation [56]. Furthermore, the effective contribution of the C and N atoms to the total diffracted intensity is very

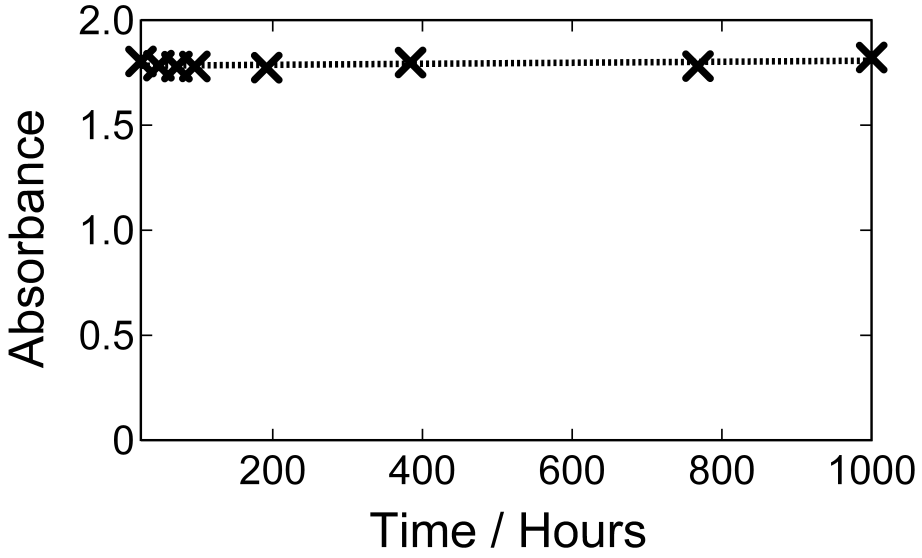

FIGURE 4.10. Absorbance of mixed-halide perovskite at 500 nm under simulated full sunlight conditions for over 1000 hours.

small relative to the contributions from Pb, Cl and I since scattering is dominated by higher atomic number elements.

The peak positions for the synthesised mixed $CH_3NH_3PbI_2Cl$ at (h,h,0) were observed to be shifted towards lower 2θ and were positioned inbetween the pure methylammonium trihalogen plumbate i.e. $CH_3NH_3PbI_3$ and $CH_3NH_3PbCl_3$ [54] respectively, and also the increased lattice parameters of the $CH_3NH_3PbI_2Cl$ film as compared to pure Cl based perovskite i.e. $CH_3NH_3PbCl_3$ (a = 5.67 Å) with the addition of I content gives an evidence of the formation of mixed halide perovskite [57].

The diffraction pattern of the product contained a few unidentified peaks, they can be attributed to the various factors including the presence of some impurity (e.g. Pb(OH)Cl, CH_3NH_3X ; X = Cl and/or I, or a related compound that may generate during the synthesis even if slightly excess of reactants are used, and also to the hygroscopic nature of the compound which can resultantly form unwanted impurity [57].

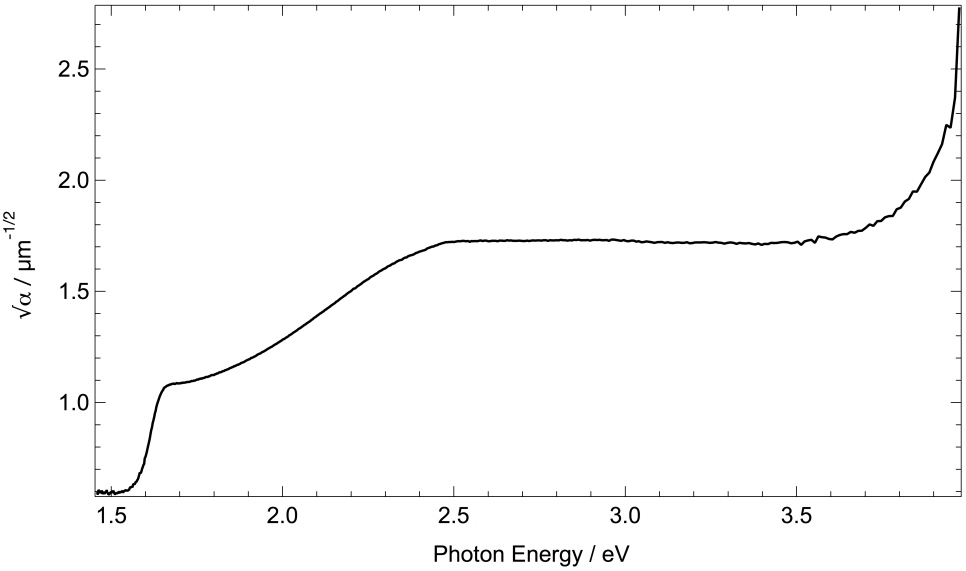

FIGURE 4.11. Absorption coefficient square rooted against photon energy. Sample is mixed-halide perovskite on glass. Thickness of 463 nm determined by averaged surface profilometer measurements.

4.5.4. High-resolution transmission electron microscopy of mixed-halide perovskite

Kojima and co-workers demonstrate using scanning electron microscopy (SEM) [55] and Im and co-workers demonstrate using transmission electron microscopy (TEM) [58], nano-sized particle (2-3 nm) features on the TiO_2 to which they assign the perovskite (figure 4.13). From the narrow XRD peak widths of the $CH_3NH_3PbI_2Cl$ perovskite it is clear that the crystals are highly crystalline and likely to be large crystallites. I took high-resolution transmission electron microscopy (HRESTEM) (with assistance from Edward Crossland) on TiO_2 sensitised with perovskite. Initial imaging on carbon film resulted in poor resolution images Figure4.13(d). Subsequent imaging taken on lacey carbon film resulted in much better resolution micrographs; however, the presence of perovskite was difficult to determine 4.13(e-f).

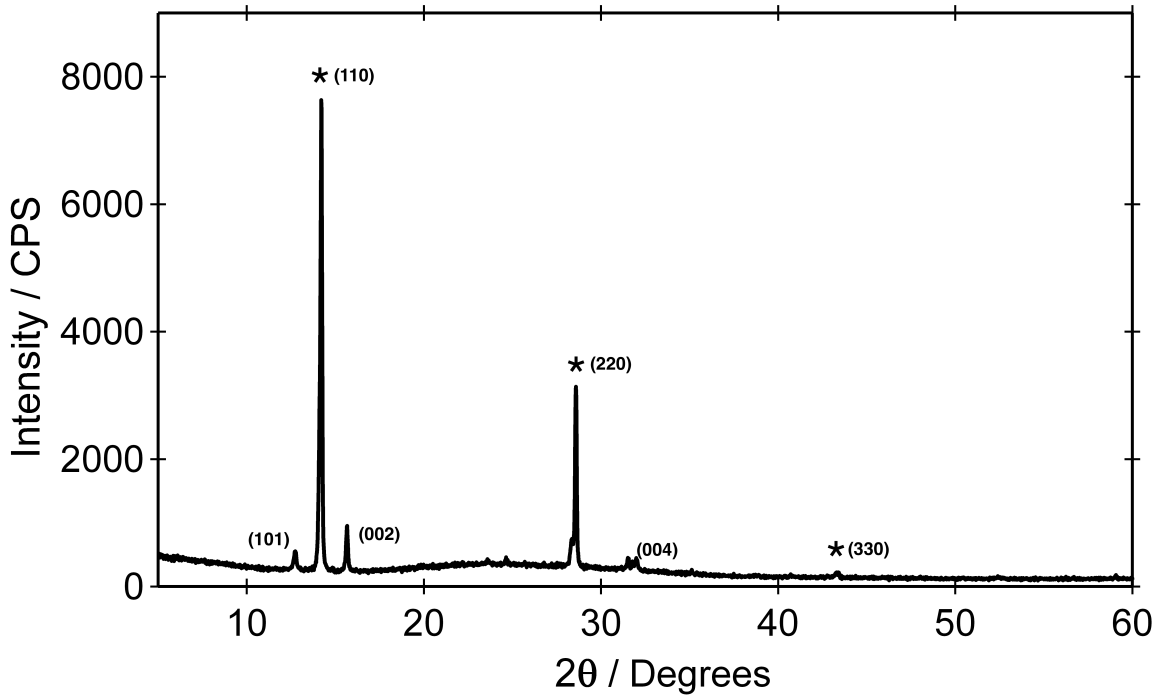

FIGURE 4.12. X-Ray Diffraction Pattern of K330 perovskite made on glass at dried at 100°C and measured at room temperature using Cu Kα line.

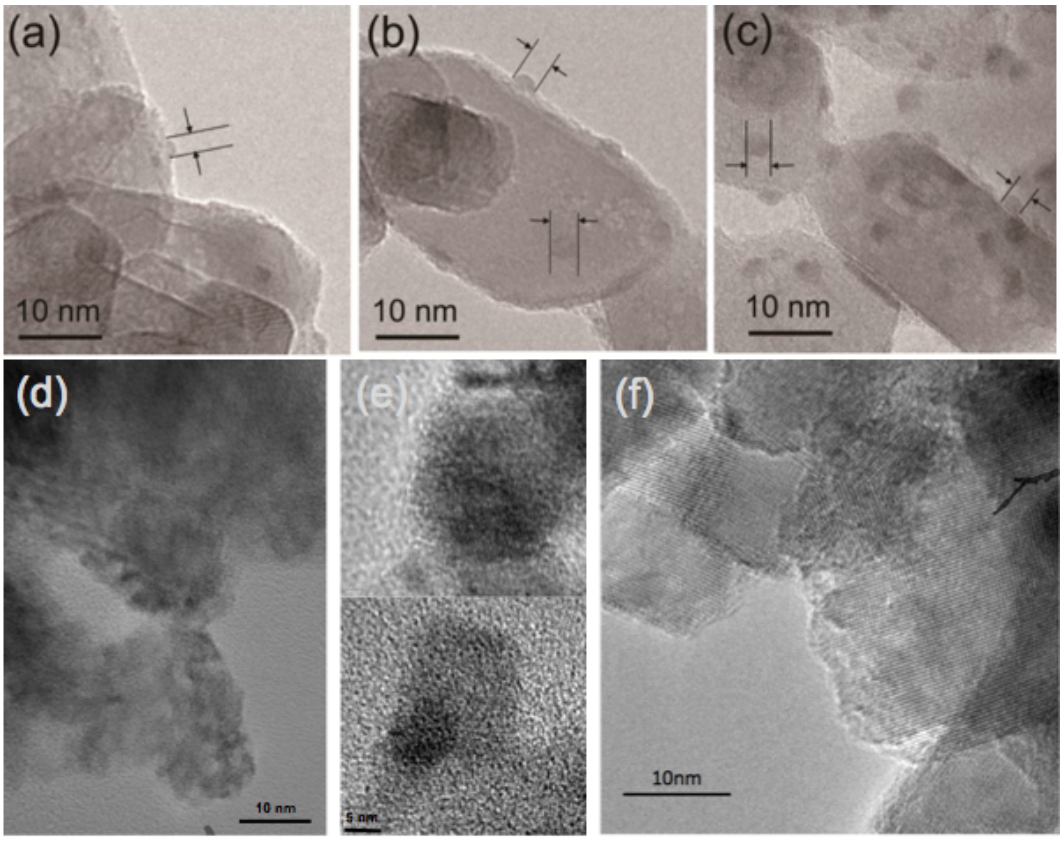

FIGURE 4.13. Transmission electron micrographs of perovskite on TiO_2 sensitised with perovskite. (a - c) taken from [58] (Permission requested). (d - f) taken with assistance of Edward Crossland.

5. Sensitised Perovskite Hybrid Solar Cell

5.1. State-of-the-art

The leading emerging technologies vying to realise the ultimate goal of low cost solar power generation are dye-sensitised and organic photovoltaics. Dye-sensitised solar cells are composed of a mesoporous n-type metal oxide photoanode, sensitised with organic or metal complex dye and infiltrated with a redox active electrolyte [3]. They currently have certified power conversion efficiencies of 11.4% [59] and highest reported efficiencies are 12.3% [21]. The current embodiment of organic solar cells, is a nanostructured composite of a light absorbing and hole-transporting polymer blended with a fullerene derivative acting as the n-type semiconductor and electron acceptor [60, 61]. The most efficient organic solar cells are now just over 10% [59]. Beyond organic materials and dyes, there has been growing activity in the development of solution processable inorganic semiconductors for thin-film solar cells. Specific interest has emerged in colloidal quantum dots, which now have verified efficiencies of over 7%, [62] and in cheaply processable thin film semiconductors grown from solution such as copper zinc tin sulphide selenide (CZTS/Se) which has generated a lot of excitement recently by breaking the 10% efficiency barrier in a low cost fabrication route [59]. The main issue currently with CZTS/Se system is that it is processed with hydrazine, a highly explosive reducing agent [63]. There is an emerging area of 'extremely thin absorber' solar cells which are a variation on the solid-state dye-sensitized solar cell [64]. An extremely thin absorber (ETA) (few nm thick) layer is coated upon the internal surface of a mesoporous TiO_2 electrode, and subsequently contacted with a solid-state hole-conductor or electrolyte. These devices have achieved efficiencies of up to 6.3% for solid-state devices employing Sb_2S_3 as the absorber [65]. However, the ETA concept still suffers from rather low open-circuit voltages, despite the use of an

inorganic absorber.

Here the properties of inorganic semiconductors combined with solution processing by using a lead-halide perovskite absorber have been utilised. The perovskite structure provides a framework to embody organic and inorganic components (see chapter 4.5) into a neat molecular composite. Herein lie possibilities to manipulate material properties, governed by the atomic orbitals of the constituent elements, the interplay between organic-inorganic components at the molecular scale, and by the size-tunable crystal framework to form new and interesting materials using rudimentary wet chemical methods. Recently, organometal halide perovskite have been reported as sensitisers in liquid electrolyte based photo-electrochemical cells, and delivered solar power conversion efficiencies of between 3.5 to 6.5% [55, 58], see Figure 5.1. However, in this previously reported electrolyte system the perovskite absorbers degrade rapidly due to incompabilitity with solvents in the electrolyte, subsequently the solar cells drop in performance after only ten minutes of operation.

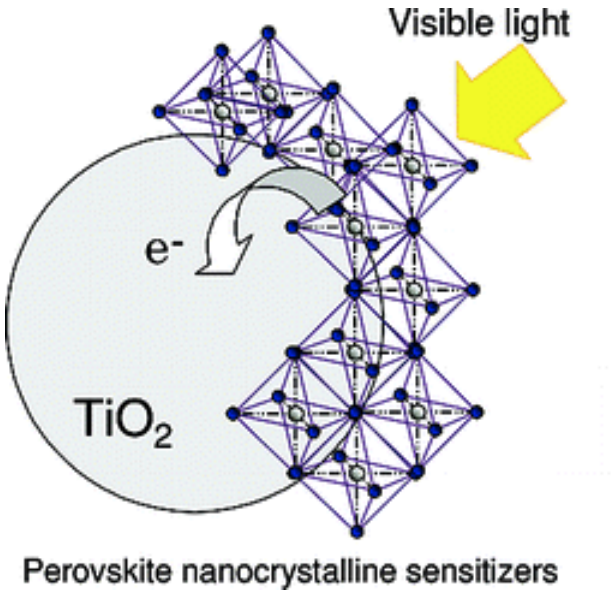

FIGURE 5.1. Schematic representation of perovskite sensitiser anchored on TiO_2 permission requested from (permission requested from [55]).

5.2. First solid-state perovskite sensitised solar cells

The devices were made according to instructions detailed in chapter 2.1.2 and 2.1.1. Briefly, a 0.5 μm thick mesoporous TiO_2 layer was deposited by spin-coating TiO_2 paste diluted further in anhydrous ethanol at 1:1.5 by weight at 2000 RPM. 25 μl of 20 wt% perovskite precursor solution was dispensed onto a pre-prepared mesoporous electrode film spin-coated at 1500 RPM for 30 seconds in air. The coated films were then placed on a hot plate set at 100 °C for 45 minutes in air. During the drying procedure at 100 °C, the coated electrode changed color from light yellow to dark brown, indicating the formation of the perovskite film. 25 μl of a chlorobenzene solution containing 68 mM Spiro-OMeTAD, 55 mM tert-butylpyridine and 9 mM lithium bis(trifluoromethylsyfonyl)imide salt was cast onto the perovskite coated substrate and spun at a rate of 2000 RPM for 45 seconds. Cells were left in the dark in air overnight prior to thermal evaporation of 200 nm Ag electrodes to complete the solar cells.

Surprisingly for a system with little optimisation, our initial efforts showed a lot of promise, with photo-conversion efficiencies of up to 6.2% using (2,2(7,7(-tetrakis-(N,N-di-pmethoxyphenylamine)9,9(-spirobifluorene) (spiro-OMeTAD) as the solid-state hole-transporter (see figure 5.2) which heralded a lab breakthrough (previously our best efficiencies just over 5%). The application of Poly(3-hexylthiophene-2,5-diyl) (P3HT) as the solid-state hole-transporter yields fairly impressive photo-conversion efficiencies of 3%. Figure 5.4 shows some preliminary stability measurements for unsealed devices over 300 scans (one scan relates to 2 minutes of illumination) or 600 minutes of constant light-soaking under simulated AM 1.5G 100 mW cm^{-2} solar illumination.

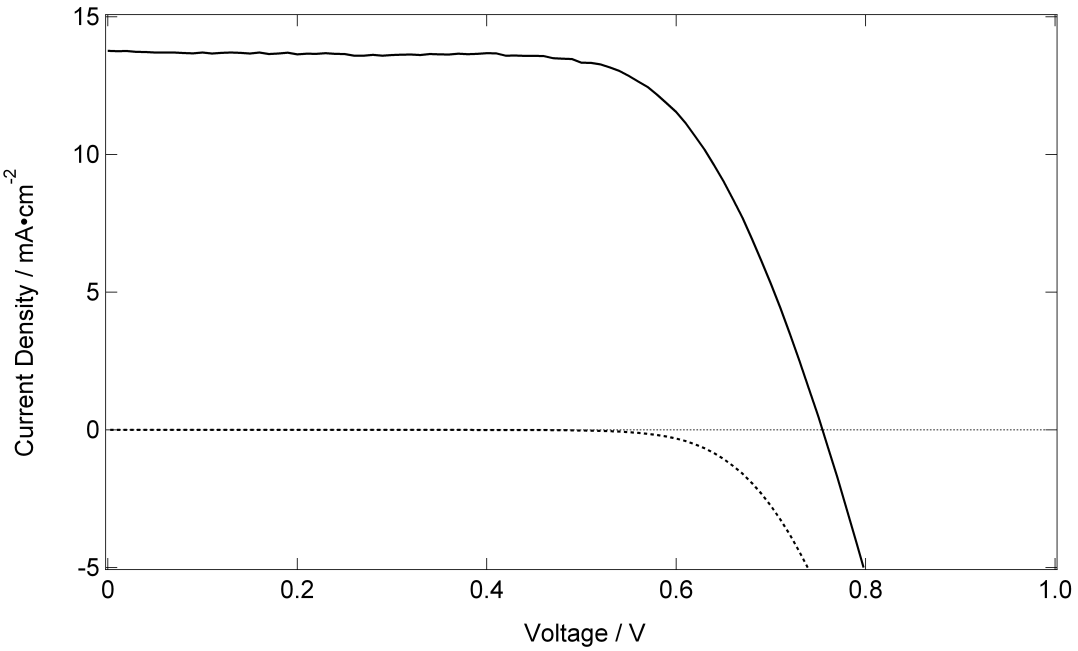

FIGURE 5.2. Current-Voltage characteristics of first-ever perovskite-sensitised solar cell in solid-state form under full sunlight illumination. Full trace is the current-voltage response under illumination, the dashed trace current-voltage response without illumination.

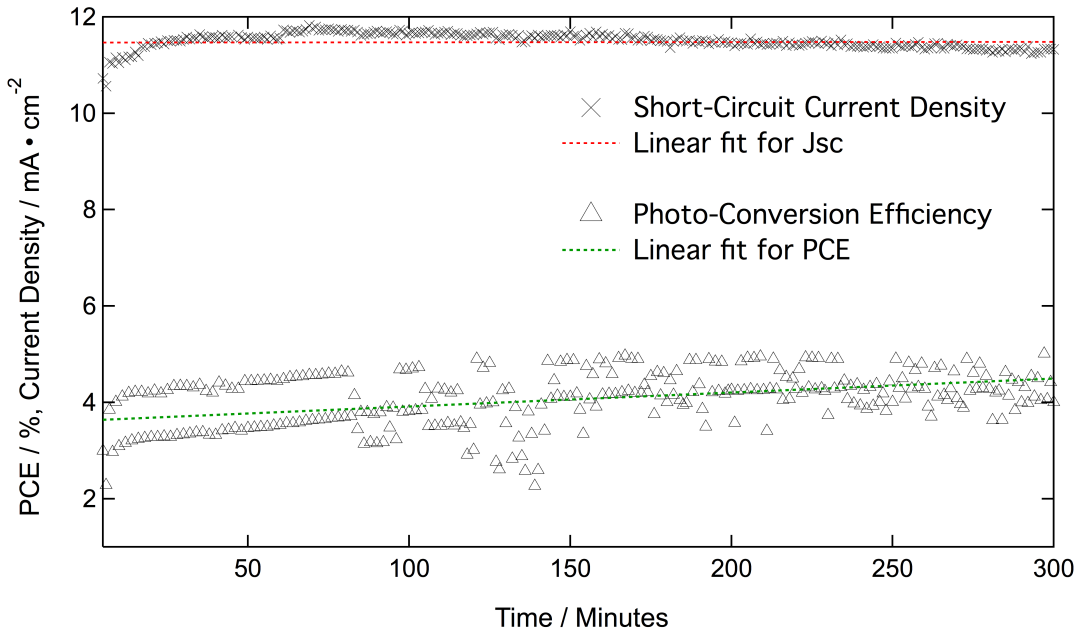

FIGURE 5.3. Stability measurements of P3HT-based perovskite devices - current density and photo conversion efficiency.

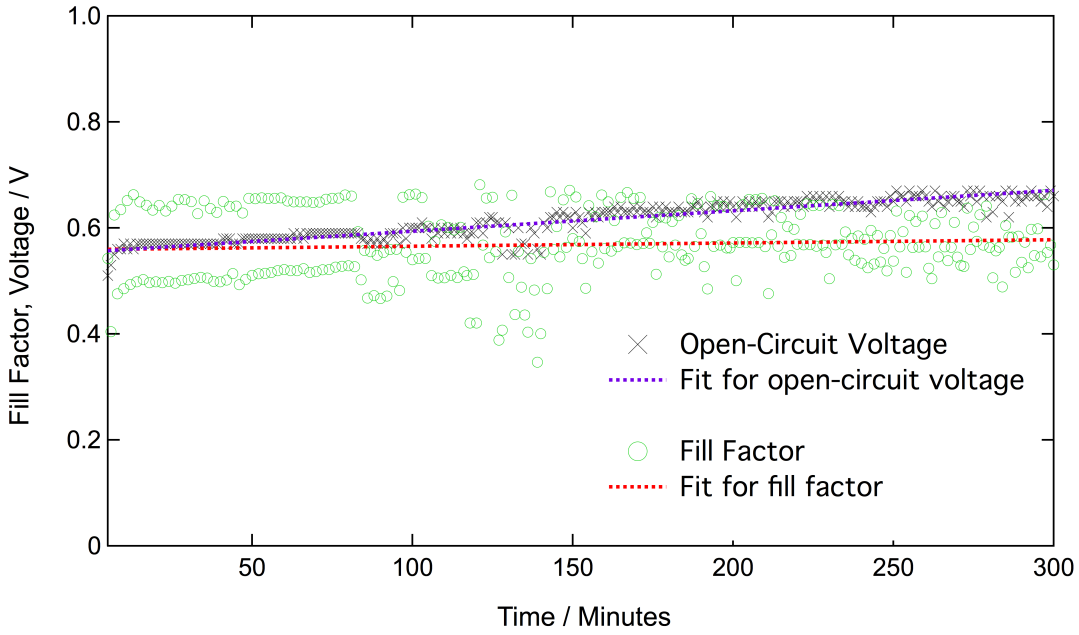

FIGURE 5.4. Stability measurements of P3HT-based perovskite devices - voltage and fill factor.

5.3. Optimisation strategy for perovskite sensitised solar cells

A strategy for creating the most efficient photovoltaic device is to consider each element of the device (see figure 5.5) independently of its constituents, i.e. optimise one component of the device whilst keeping all other parameters constant. Listed are the components of the device system that may be optimised:

1. Transparent substrate
2. Electron-extraction layer
   (a) Transparent-conducting oxide (TCO)
   (b) Metal oxide
3. Surface treatments
4. Light sensitiser
5. Post-sensitiser treatments
6. Hole-extraction layer
   (a) Hole-transporting medium (HTM)
   (b) Counter electrode
7. Post-device treatments

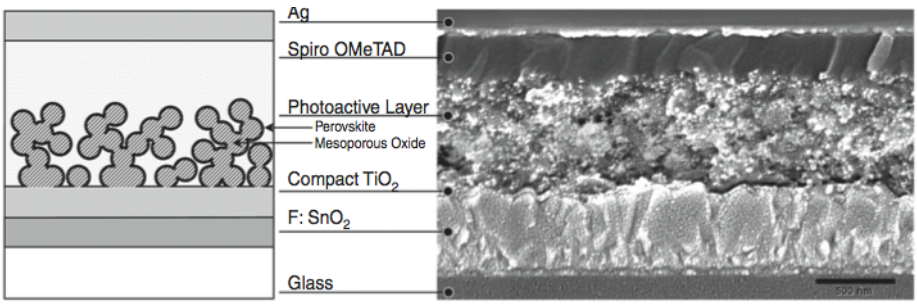

FIGURE 5.5. Device architecture (left) with cross-sectional scanning electron micrograph of device (right)

The optimisation process is labour-intensive and serves to generate a vast amount of data. The omission of this bulk of data serves as a kindness to the reader, instead of a dispassionate list of experiments which showed promised and which didn't yield any discernible benefit; a select few aspects of the optimisation will be discussed here: the roles of the surface (TiO_2:perovskite) interface, design of the mesostructure with implications to light-harvesting and charge generation, the thickness of the perovskite absorber with implications for charge extraction and light-harvesting, design and control of novel perovskite absorbers, finally a consideration of stability and reproducibility.

5.4. Surface considerations

The surface of the metal-oxide (in this case titanium dioxide, TiO_2) acts as the electron acceptor for the light-sensitising perovskite. Control over the metal-oxide to absorber interface is critical because it influences electron-injection by controlling the conduction-band level, thus setting Gibbs free energy (resulting in more or less thermodynamically favourable electron-injection). Furthermore, photovoltage may be maximised via band-edge engineering: by raising the conduction band-edge we are able to increase the useful voltage out of the device [66]. The surface will also influence electron-transport through the metal-oxide since defects on the surface can lead to trap-states (states where the electron is tightly bound and does not contribute to conductivity) eventually leading to increased recombination. It has been reported that the surface properties are likely to affect how the absorber forms. For perovskite films surface treatments of potassium hydroxide (KOH) is used to improve film quality [53]. Three surface treatments were considered: an industry standard titanium tetrachloride ($TiCl_4$) treatment, cheno deoxy cholic acid (CDCA) a well known molecular spacer as a co-adsorbent, and our workhorse dye-sensitiers (both organic [67, 68] D131 [69] and inorganic Z907 [25].)

5.4.1. $TiCl_4$

A thin layer of TiO_2 is grown on the surface of the metal oxide through chemical bath deposition (a solution of pre-prepared $TiCl_4$ diluted in water at a molarity of 2 M is further diluted to molarities typically 15 - 20 mM) for 1 hour at 70°C. The substrate is then dried and sintered to 550°C for 2 hours. However, with or without $TiCl_4$ treatment our device performed equally well, see table 5.1. $TiCl_4$ surface treatment is known to reduce particle-to-particle grain boundaries by fusing neighbouring particles together. This phenomena is known as 'necking', Fuke and co-workers have been shown that the surface treatment of TiC_4 improves electron-transport, manifested as increased short-circuit current and a reduction in impedance measured by electronic impedance spectroscopy [70]. Furthermore, Fuke and co-workers report that transient absorption signals did not change which suggests electron injection is not affected by the treatment [70]. The benefit of not requiring $TiCl_4$ treatment lies in the processing of the device, an extra high temperature (550°C) sintering stage is by-passed thus energy and time is saved. The implications here is that if a low-temperature route to forming the metal-oxide mesostructure can be found then processing on plastic (low-temperature) substrates may also become a reality.

Treatment	Jsc (mA cm^{-2})	Voc (mV)	Fill Factor	PCE (%)
Standard	15.4	820	0.61	7.7
+ With TiC_4	14.8	840	0.58	7.2

TABLE 5.1. Current-voltage characteristics of solid-state perovskite-sensitised solar cells with and without $TiCl_4$ surface treatment.

5.4.2. Chenodeoxycholic acid

Chenodeoxycholic acid (CDCA) is known to function as an anti-aggregation agent to improve the photovoltaic effect in dye-sensitised solar cells [71]. CDCA is electronically inert, so when it is adsorbed to the surface serves to segregate sensitiser

molecules, i.e. act as a molecular spacer. CDCA molecules are adsorbed to the metal oxide surface via a chemical bath deposition in a solution of CDCA, dissolved typically in ethanol (EtOH) at molarities of 0.1 mM for 30 minutes at room temperature. The solvent choice was crucial since the formed perovskite would dissolve instantly in almost all solvents apart from chlorobenzene and toluene. Therefore solutions of CDCA had to be dissolved in compatible solvents. The application of CDCA was to understand how the packing of the perovskites affected performance. No change was observed with any addition of CDCA, thus this indicates that the surface-perovskite interface isn't playing a major role in the fundamental losses of the photovoltaic operation, see table 5.2.

Treatment	Jsc (mA cm^{-2})	Voc (mV)	Fill Factor	PCE (%)
Standard	13.1	750	0.63	6.19
+ With CDCA	13.8	730	0.59	5.9

TABLE 5.2. Current-voltage characteristics of solid-state perovskite-sensitised solar cells with and without chenodeoxycholic acid surface treatment.

5.4.3. Co-sensitisation

Thin-film solid-state hybrid solar cells tend to suffer from poor spectral sensitivity in the near-IR. In order to improve the overall efficiency of solid-state hybrid solar cells attention has been focused on extending absorption characteristics of the absorber by complementing it with another sensitiser on the surface of the metal oxide. To achieve co-sensitisation a similar strategy to CDCA, with a careful selection of solvents and order of processing was employed. Overall, devices did not improve with co-sensitisation but the absorption character could be controlled, see figure 5.6. This feature could be useful if it is required to change the colour of the device, i.e. for building integrated photovoltaics (BIPV). Further, energy-transfer between perovskite and dye could be studied [72]).

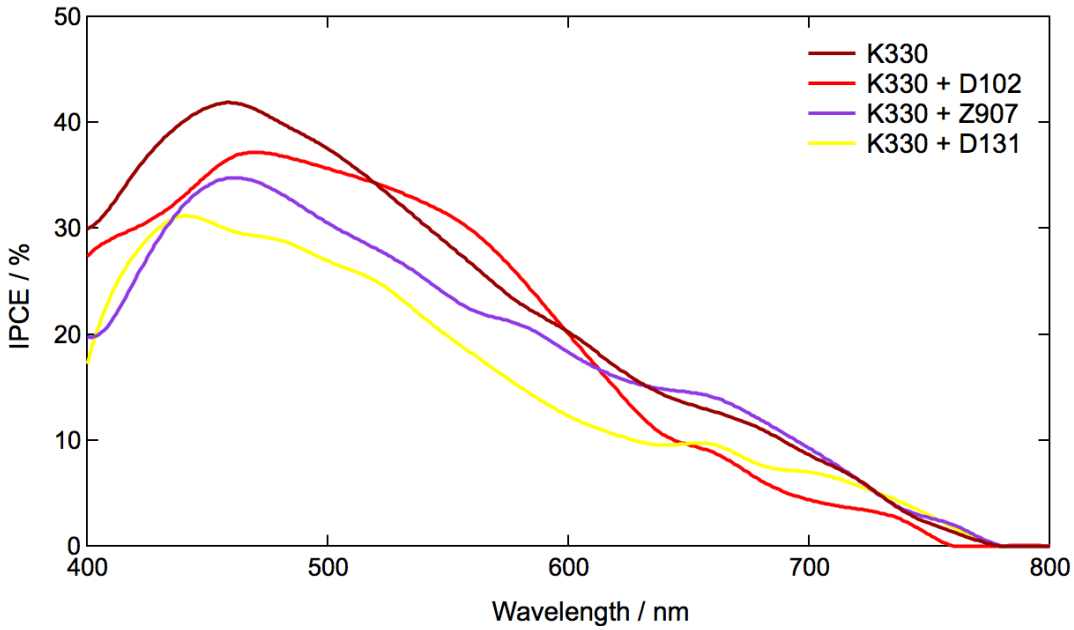

FIGURE 5.6. Incident Photon-to-Electron Conversion Efficiency spectra showing control over absorption onset via co-sensitisation.

5.5. Carrier dynamics at metal-oxide and absorber phase

Preliminary studies indicate that great enhancements in photovoltaic performance are not to be made by rudimentary surface modifications. Thus I turn my attention to loss channels that may exist within the metal-oxide and absorber phase; that is to consider carrier dynamics in the titanium dioxide and perovskite phase. To probe the recombination a simple test is undertaken whereby the thickness of the mesoporous oxide was varied and the thickness of the absorber layer was also varied. By changing the thickness it is possible to estimate charge extraction efficiency thus draw insight into the electron diffusion length (i.e., how far an electron travels before it is recombined) see figure 5.7.

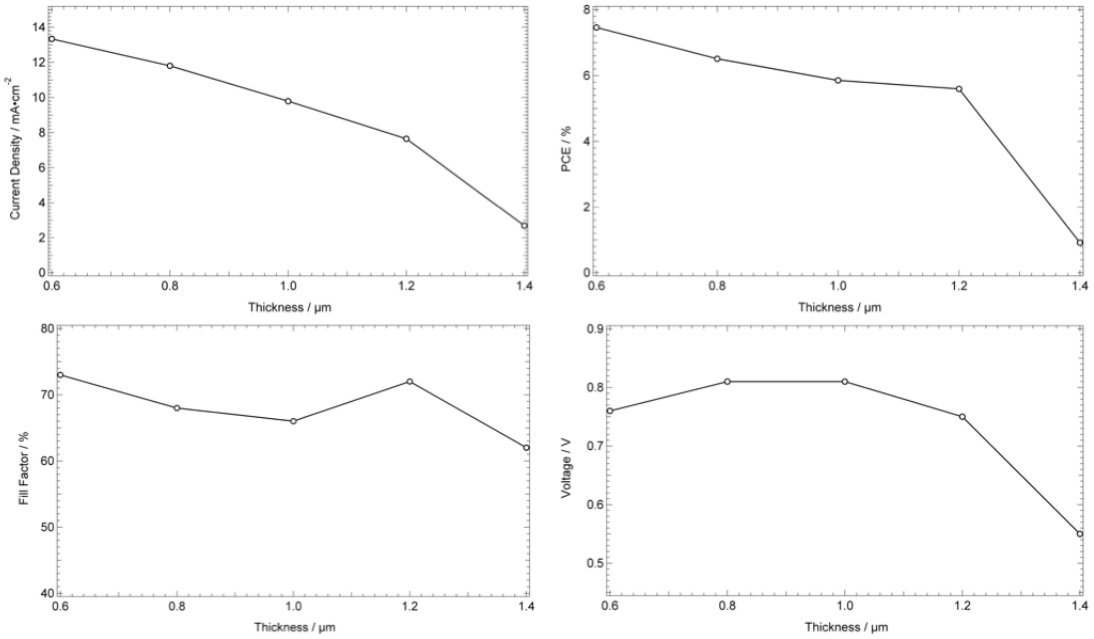

FIGURE 5.7. Thickness dependance of active layer and response of key photovoltaic parameters.

As the thickness of the photoactive layer increases it is expected that the amount of light absorbed in active layer increases, this can be seen as an increase in optical density. However, if the absorption coefficient of a material is sufficiently high, i.e. the incident light is easily attenuated, then a thicker material serves no optical benefit. In Figure 5.8 the absorption length extracted by taking the inverse of the absorption coefficient, α. For photons with energies above 2.5 eV the absorption length is around 300 nm, suggesting that a thicker active layer should not greatly enhance photocurrent harvesting at those energies. However, at lower energies (below 2.5 eV), a thicker active layer may enhance light harvesting with absorption lengths as a high as 900 nm and as low as 400 nm. The extinction of the perovskite is sufficiently high to harvest light effectively at very low thicknesses of 600 nm which has great implications for efficient charge extraction and good pore-filling, as can be seen in figure 5.9. Here the internal quantum efficiency (IQE), external quantum efficiency (EQE) per absorbed

photon, is close to unity for the thinnest films meaning that every absorbed photon is successfully converted to charge and extracted at the terminals.

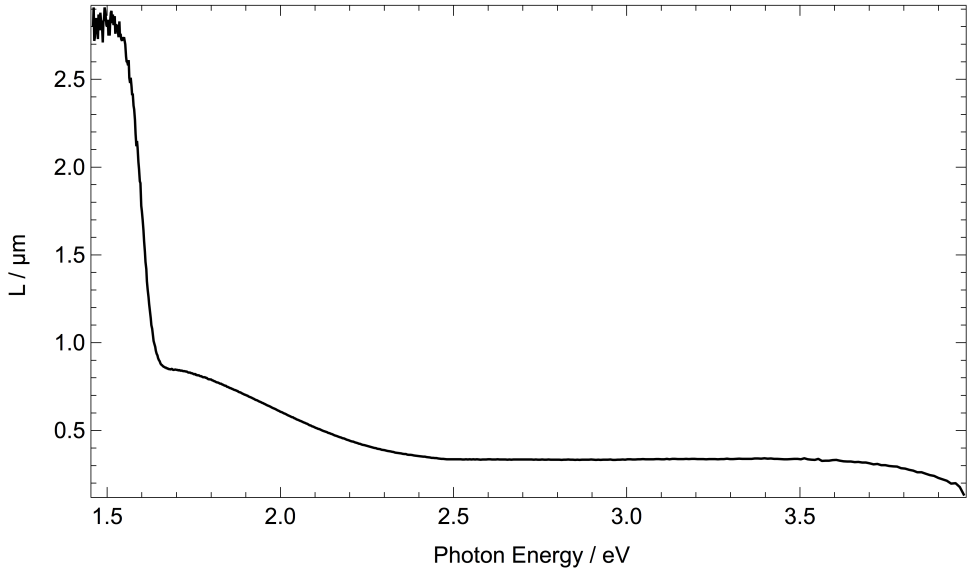

FIGURE 5.8. Absorption length against photon energy. Sample is mixed-halide perovskite on glass. Thickness of 463 nm determined by averaged surface profilometer measurements.

The balance between light-harvesting and series resistance is usually demonstrated by varying active layer thickness in dye-sensitised solar cells, where at large thicknesses of mesoporous TiO_2 layer series resistance becomes dominant because of limited charge carrier mobility in organic hole conductors [68], notwithstanding problems of pore-filling such thick structures [73, 10, 11, 12, 13, 74].

Varying the thickness of the absorber will allow us to understand the recombination dynamics, i.e, electron life times. If a device can perform with a thicker absorber layer then the electron diffusion will be long. A range of concentrations of $CH_3NH_3PbI_2Cl$ precursors were cast on mesoporous TiO_2. While at low concentrations only infiltration of the mesoporous layer is expected, at higher concentrations any excess material may form a capping layer above the filled mesostructure. As more perovskite is deposited (increasing in concentration) the optical density and

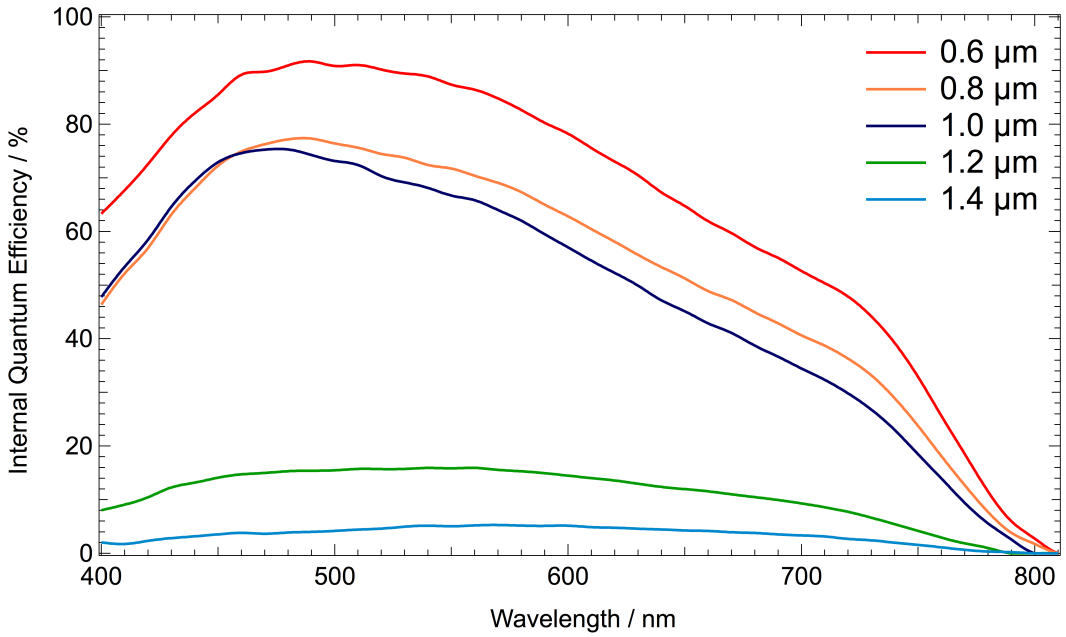

FIGURE 5.9. Internal quantum efficiency of perovskite devices with varying thickness of mesoporous titanium dioxide.

therefore the amount of photons absorbed increases in both absorber layers leading to the increase in photocurrent. However, a maximum in photocurrent generated is observed at 30 wt % for the mixed-halide perovskite suggesting recombination effects are beginning to dominate (see Figure 5.10), this is possibly the situation when a capping layer begins to form thus lower porefilling and increased recombination would be expected.

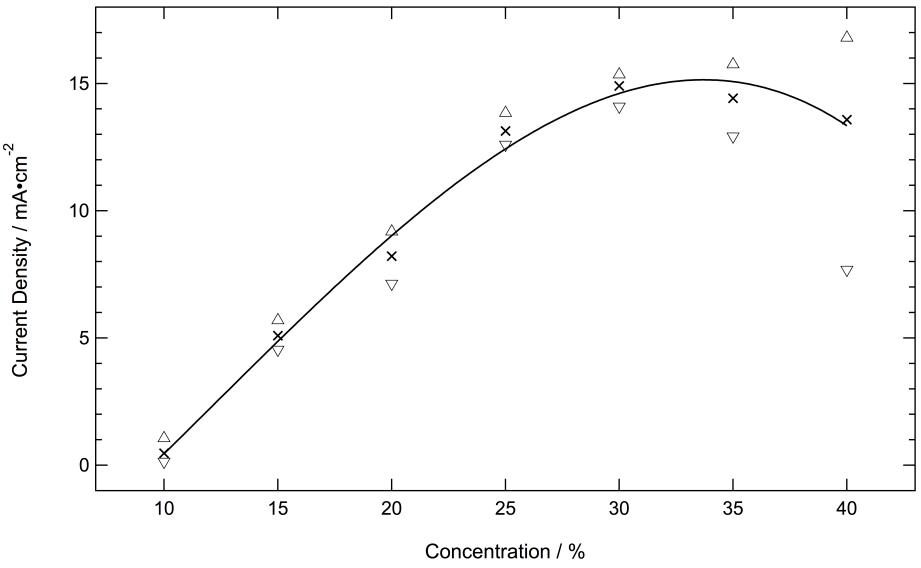

FIGURE 5.10. Dependance of short-circuit photocurrent response on absorber thickness. These experiments were performed by Leonie Vogt.

Within the mesoporous structure the charge collection efficiency will be close to unity since the interfaces are in such close proximity to the exciton generation site. In the capping layer, however, whether charges can be collected will crucially depend on the electron diffusion length. For excitons generated within the perovskite further than half the exciton diffusion length from an interface, recombination is likely to occur leading to lower charge extraction. At high concentrations of the mixed-halide perovskite a wider spread in the measured current density is observed, this can be explained by the thicker perovskite layer having a greater defect density and therefore more shunting paths.

A brief study varying the thickness of the HTM overlayer (and therefore the distance between the perovskite and the Ag electrode) shows a reduced dark current leakage (associated with device short circuiting) see Figure 5.11.

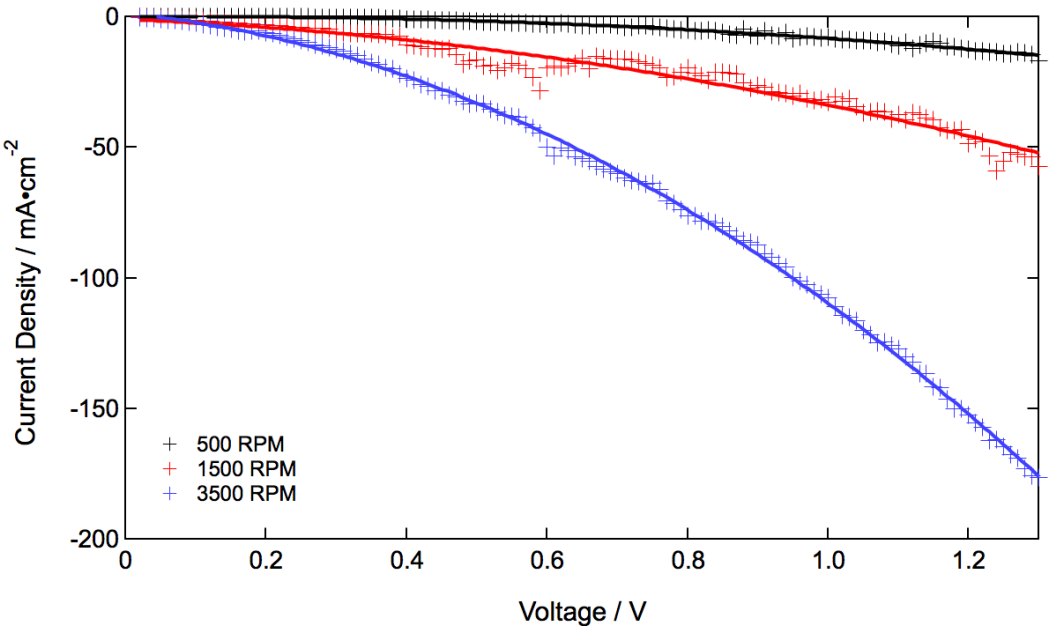

FIGURE 5.11. Dark (without illumination) current-voltage characteristics of different thicknesses of hole-transporter over layer (controlled by spin speed, i.e. faster spin speed relates to thinner over layer and vice versa)

5.6. New perovskite absorbers

Improvements in overall device performance is likely to come from extending the perovskite absorber towards wavelengths of 900 nm in order to harvest more of the solar spectrum. Very briefly, new perovskites are considered here. Different perovskites were formed by blending two perovskites (both mixed at 3:1 organic to inorganic molar ratio) together: $CH_3NH_3PbBr_2Cl$ bromine-based and $CH_3NH_3PbI_2Cl$ iodine based at different ratios. Figure 5.12 shows it is possible to control the electronic character, see Table 5.3. Figure 5.13 shows that it is possible to control the absorption character. Work has been done by Im *et al.*, to create a red perovskite with an onset of 600 nm [47]. They achieve this change in band-gap not by varying the halogen content but by physically changing the crystal size (owing to 2D confinement) by changing the organic cation element from the prototypical methylamine chain to an

ethylamine chain thus moving from a 3D perovskite to a layered 2D perovskite.

Treatment	Jsc (mA cm^{-2})	Voc (mV)	Fill Factor	PCE (%)
I + Br doped	7.2	850	0.8	4.91
I_3 doped	6.79	720	0.71	3.29

TABLE 5.3. Current-voltage characteristics of solid-state perovskite-sensitised solar cells blended perovskites showing high fill factor.

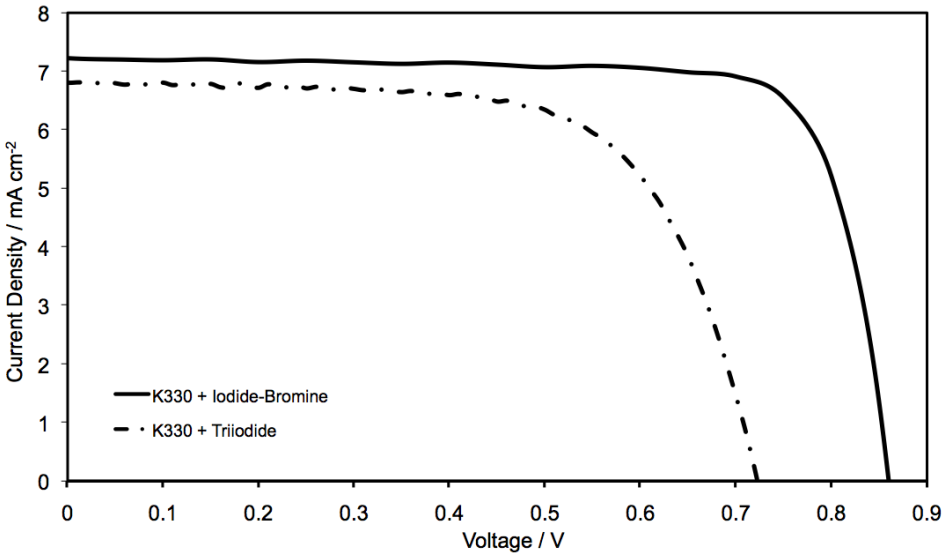

FIGURE 5.12. Current-Voltage characteristics of blended perovskite showing high fill factor

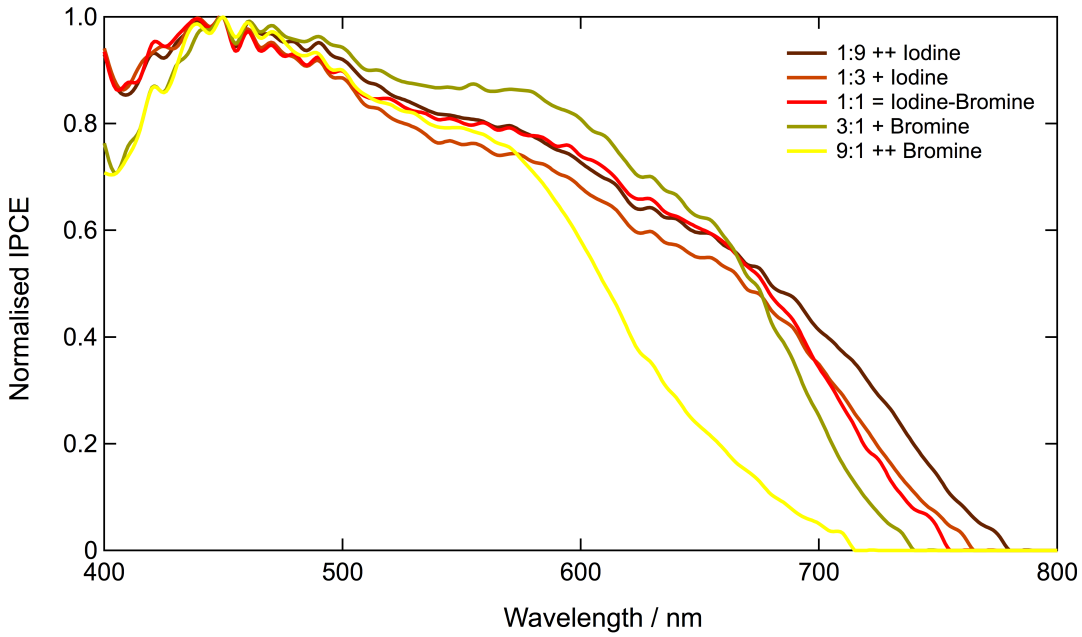

FIGURE 5.13. Normalised Incident Photon-to-Electron Conversion Efficiency spectra of blended perovskites showing control over onset in absorption.

6. Meso-Superstructured Perovskite Hybrid Photovoltaic

An efficient solar cell must absorb over a broad spectral range, from the visible to near infrared region (350 to ∼950 nm), and convert the incident light effectively into charge. Beyond this, the charge must be collected at a high voltage in order to do useful work, and it is the generation of a high voltage with suitable current that is the most challenging aspect for emerging solar technologies [3, 59, 75, 21, 60, 61, 76, 63]. A simple measure of how effectively a solar cell generates voltage from the light it absorbs is to consider the difference in energy between the optical band gap of the absorber and the open-circuit voltage generated by the solar cell under simulated AM1.5G 100 $mW{\cdot}cm^{-2}$ solar illumination [77]. For instance GaAs solar cells exhibit open-circuit voltages of 1.11 V and an optical band gap of 1.4 eV giving a difference of approximately 0.29 eV [59]. For dye-sensitized and organic solar cells this difference is usually on the order of 0.7 to 0.8 eV [59, 77]. For organics, such losses are predominantly due to their low dielectric constants resulting in the formation of tightly-bound excitons. This requires a heterojunction with an electron acceptor with a significant energy offset to enable ionization and charge separation [78, 79]. Likewise, dye-sensitized solar cells (DSC) have losses, both due to electron transfer from the dye (or absorber) into the TiO_2 which requires a certain 'driving force' and due to dye regeneration from the electrolyte which requires an 'over potential'. Efforts have been made to reduce such losses in the DSC by moving from a multi-electron iodide/tri-iodide redox couple to one-electron outer-sphere redox couples, such as a cobalt complexes or a solid-state hole-conductor [3, 21, 6, 80]. Recently, there has been mounting interest in inorganic semiconductor sensitized solar cells, [6, 64]. An extremely thin absorber (ETA) layer, 2 - 10 nm in thickness, or indeed quantum dots, is coated upon the internal surface of a mesoporous TiO_2 electrode and subsequently contacted with an electrolyte or solid-state hole-conductor. These

devices have achieved power conversion efficiencies of up to 6.3% [65]. However, the ETA concept still suffers from rather low open-circuit voltages despite the use of an inorganic absorber. The problem may lie in the characteristically disordered and extremely low mobility n-type metal oxide employed, TiO_2 [81].

6.1. Meso-Superstructure concept

Here, our motivation has been to develop a solution-processable solar cell which overcomes the fundamental losses of organic absorbers and disordered metal oxides. We first follow the ETA approach and employ a perovskite absorber and mesoporous TiO_2 as the transparent n-type component, and 2,2(7,7(-tetrakis-(N,N-di-pmethoxyphenylamine)9,9(-spirobifluorene))) (spiro-OMeTAD) as the transparent p-type hole conductor. These devices already exhibit power conversion efficiencies close to 8%. Remarkably, we discover that the mesoporous n-type TiO_2 can be replaced with insulating Al_2O_3, and the operation of the solar cells improves. The Al_2O_3 is a wide band gap (7 to 9 eV) insulator and purely acts as a 'scaffold' upon which the perovskite is coated. We observe that electron transport through the perovskite layer is much faster than through the n-type TiO_2. In addition, we observe a few hundred mV increase in open-circuit voltage moving from the TiO_2 to the insulating Al_2O_3 scaffold, and a record power conversion efficiency of 10.9% under simulated Air Mass (AM)1.5 full sun illumination.

6.2. Device structure and physical characterisation

The solar cells are fabricated on semi-transparent fluorine doped tin oxide (FTO) coated glass, coated with a compact layer of TiO_2 which acts as an electron selective electrode (anode). The porous oxide films are fabricated from sol-gel processed sintered nanoparticles. The perovskite precursor solution infiltrates the porous oxide mesostructure via spin-coating, and is dried at 100°C which enables the perovskite

to form via self-assembly of the constituent ions. Dark coloration is only observed after this drying step. To elaborate upon the perovskite coating process, there has been extensive work done on investigating how solution-cast materials infiltrate into mesoporous oxides [73, 10, 11, 12, 13, 74]. If the concentration of the solution is low enough, and the solubility of the cast material high enough, the material will completely penetrate the pores as the solvent evaporates. The typical result is that the material forms a "wetting" layer upon the internal surface of the mesoporous film, which uniformly coats the pore walls throughout the thickness of the electrode. The degree of 'pore-filling' is controlled by varying the solution's concentration. If the concentration of the casting solution is high, then maximum pore filling occurs, and any 'excess' material forms a 'capping layer' on top of the filled mesoporous oxide. For the optimum perovskite precursors concentrations employed here, there is no appearance of a capping layer, which implies that the perovskite is predominantly formed within the mesoporous film. We have verified that the perovskite is within and uniformly distributed throughout the mesoporous oxide films by performing cross-sectional electron microscopy (SEM) with elemental mapping via energy dispersive x-ray (EDX) analysis which is shown in figure 6.1.

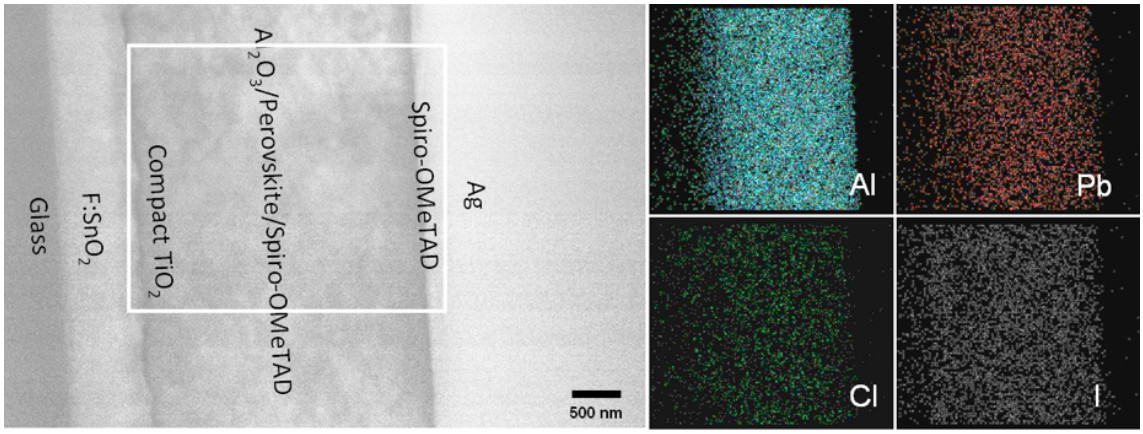

FIGURE 6.1. Cross-sectional scanning electron micrograph (SEM) of a 3 μm thick device (left), and energy-dispersive x-ray (EDX) spectroscopy with elemental mapping of (right) aluminium, lead, chlorine, iodine.

To confirm the presence of the $CH_3NH_3PbI_2Cl$ throughout the mesoporous Al_2O_3, we have performed energy dispersive x-ray (EDX) analysis on a cross section of a device. Figure 6.1 shows a cross-sectional scanning electron micrograph (SEM) of a 3 μm thick device (left), and EDX spectroscopy with elemental mapping of (right) aluminium, lead, chlorine, iodine. We show the uniform distribution of Al, Pb, Cl, and I throughout a 3 μm thick film. We note that for the optimised devices the mesoporous alumina films are only 0.5 μm thick, but we have used a 3 μm due to spatial resolution limitations of the EDX technique. The elemental composition determined by the EDX gives an approximately 2:1 I:Cl ratio.

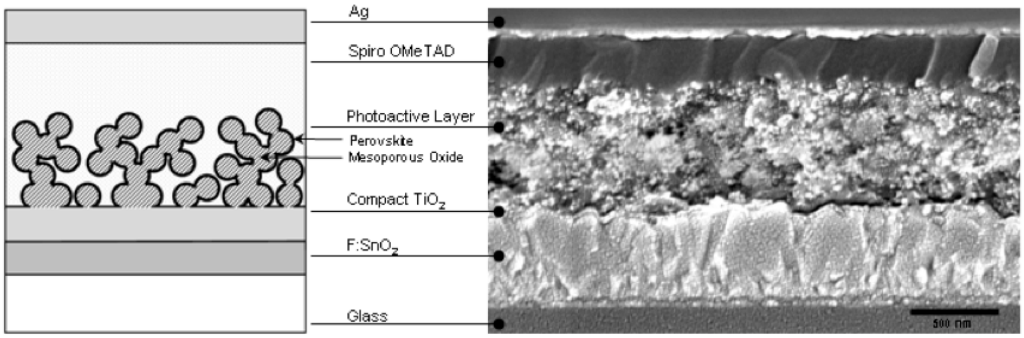

FIGURE 6.2. Schematic representation of full device structure, where the mesoporous oxide is either Al_2O_3 or anatase TiO_2 (left), Cross-sectional SEM image of a full device incorporating mesoporous Al_2O_3 (right). Scale bar represents 500 nm. SEM measurements were taken using JEOL JSM 7500F.

To complete the photoactive layer, the perovskite coated porous electrode is further filled with the hole-transporter, spiro-OMeTAD, via spin-coating. A schematic illustration of a complete device is given in Figure 6.2. It is apparent from an SEM cross section of an optimised device shown in Figure 6.2, that the spiro-OMeTAD has formed a capping layer, which ensure selective collection of holes at the silver electrode.

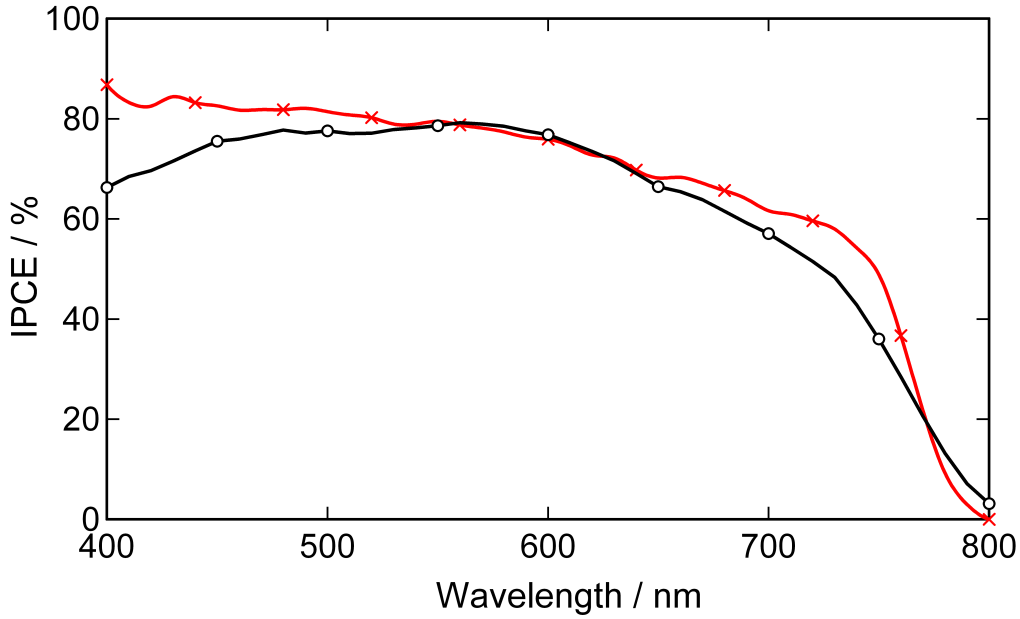

FIGURE 6.3. IPCE action spectrum of an Al_2O_3 based and perovskite sensitised TiO_2 solar cell, with device structure: FTO/Compact-TiO_2/Mesoporous Al_2O_3 (red trace with crosses) or mesoporous TiO_2 (black trace with circles)/$CH_3NH_3PbI_2Cl$/Spiro-OMeTAD/Ag

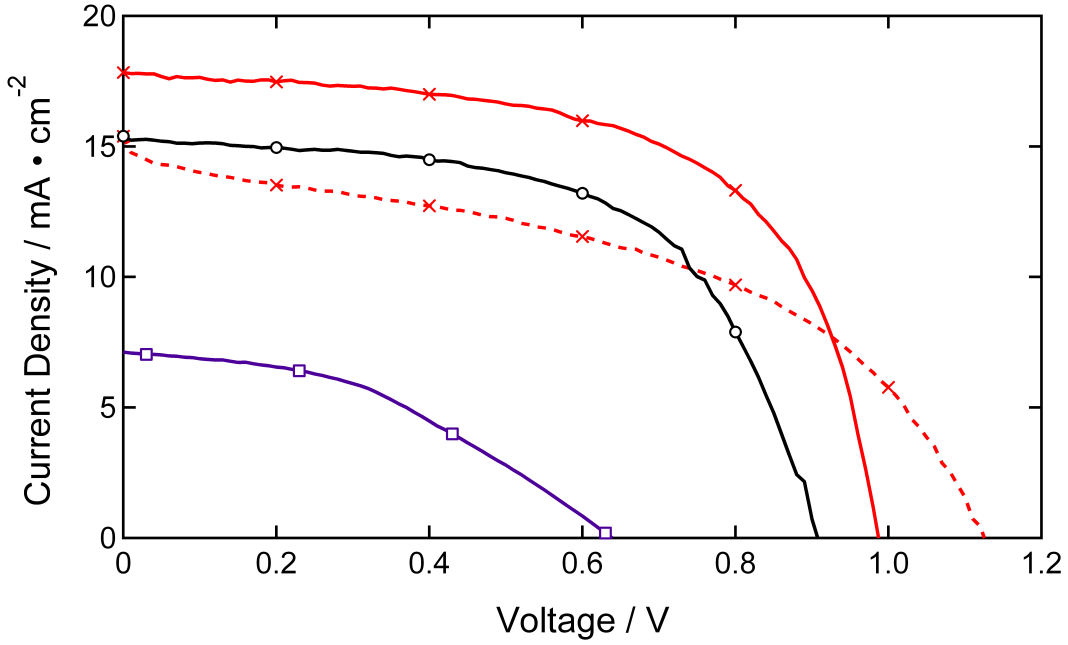

FIGURE 6.4. Current-Voltage characteristics under simulated AM1.5G 100 mW·cm^{-2} illumination for Al_2O_3 based cells, one cell exhibiting high efficiency (red solid trace with crosses, J_{SC} = 17.8 mA·cm^{-2}, V_{OC} = 0.98 V, FF = 0.63, η = 10.9%) and one exhibiting V_{OC} greater than 1.1 V (red dashed line with crosses, J_{SC} = 15.4 mA·cm^{-2}, V_{OC} = 1.13 V, FF = 0.45, η = 7.8%), perovskite TiO_2 sensitised solar cell (black trace with circles) exhibiting J_{SC} = 15.4 mA·cm^{-2}, V_{OC} = 0.80 V, FF =0.53, η = 7.6%. We further illustrate the 'semiconducting' nature of the perovskite by the construction of a planar-junction diode with a structure FTO/compact TiO_2/ $CH_3NH_3PbI_2Cl$/Spiro-OMeTAD/Ag (purple trace with squares). The perovskite film is approximately 150 nm thick in this configuration, and the solar cell generates J_{SC} = 7.13 mA·cm^{-2}, V_{OC} = 0.64 V, fill factor = 0.4 and η = 1.8%.

6.3. Optoelectronic characterisation

In Figure 6.3 the incident photon-to-electron conversion efficiency (IPCE) action spectrum is shown for the devices employing mesoporous TiO_2 and Al_2O_3, exhibiting spectral sensitivity spanning from the visible to the near-IR (400 to 800 nm) with a peak IPCE of over 80% for both 'concepts'. The slight difference in shape is due to slightly different perovskite concentrations in the optimised devices. In Figure 6.4 we show current voltage curves measured under simulated AM1.5 100 mW cm^{-2} illumination. The sensitized solar cell employing TiO_2 gives a short-circuit photocurrent (J_{SC}) of 17.8 mA·cm^{-2}, an open-circuit voltage (V_{OC}) of 0.80 V with a fill factor of 0.53 yielding an overall power conversion efficiency of 7.6%. We present two different JV curves for the Al_2O_3 based device. The most efficient device exhibits a J_{SC} of 17.8 mA·cm^{-2}, a V_{OC} of 0.98 V with a fill factor of 0.63 yielding an η of 10.9%. The third curve, dashed trace, shows a device with respectable J_{SC} of 15.4 mA·cm^{-2} and very high V_{OC} of 1.13 V but a low fill factor of 0.45, yielding an overall power conversion efficiency of 7.8%.

In Figure 6.5 we show histograms of device performance parameters for a large batch of perovskite cells measured under simulated AM 1.5 100 mW cm^{-2} illumination comparing TiO_2 and Al_2O_3 based devices. The general trend is that the Al_2O_3 cells generate over 200 mV higher open-circuit voltages than the sensitized TiO_2 solar cells, with comparable short-circuit currents and slightly lower fill factors, giving overall a slightly higher efficiency for the meso-superstructure solar cells (MSSC) as compared to the TiO_2 sensitized devices. The distribution is reasonably wide, reducing this spread in performance is central to the commercialization of this technology.

Simply from the solar cell measurements on alumina-based devices, it is apparent that the perovskite layer is capable of functioning as both absorber and n-type component, transporting electronic charge out of the device. We further illustrate the 'semiconducting' nature of the perovskite by the construction of a planar-junction

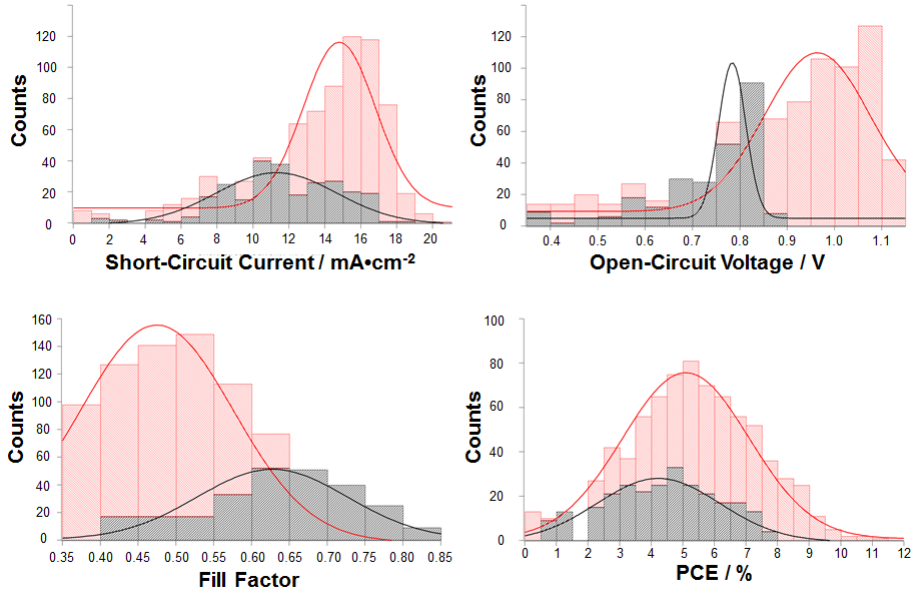

FIGURE 6.5. Histogram plots of solar cell performance parameters: fill factor, open-circuit voltage, short-circuit current and photo-conversion efficiency for a large batch of $CH_3NH_3PbI_2Cl$ sensitized TiO_2 photovoltaic devices (black, total of 262 devices) and meso-superstructured solar cells (Al_2O_3 based) (red, total of 767 devices). The Gaussian fits have been added to aid the eye.

diode with a structure FTO/compact TiO_2/ $CH_3NH_3PbI_2Cl$/Spiro-OMeTAD/Ag, i.e. no mesoporous alumina scaffold. The perovskite film is approximately 150 nm thick in this configuration, and the solar cell generates J_{SC} of 7.13 mA·cm^{-2} V_{OC} of 0.64 V fill factor of 0.4 and η of 1.8%.

If we take the optical band gap of $CH_3NH_3PbI_2Cl$ to be 1.55 eV from the IPCE onset at 800 nm[82], and the open-circuit voltage to be 1.1 V, this represents a difference in energy of only 0.45 eV, competitive with the best thin film technologies [59]. To understand why we observe such a dramatic increase in voltage over the TiO_2 cells we need to consider the operational mode of the two concepts. We would expect that for the sensitised TiO_2 device, following light absorption in the perovskite, electrons will be transferred to the TiO_2 with subsequent electron transport to the FTO electrode through the TiO_2, and holes to the spiro-OMeTAD with subsequent

transport to the silver electrode. For the Al_2O_3 based cells the electrons must remain in the perovskite phase[83] until they are collected at the planar TiO_2 coated FTO electrode, and must hence be transported throughout the film thickness in the perovskite. Hole-transfer from the photoexcited perovskite should occur to the spiro-OMeTAD in much the same way as in the sensitized device. A cartoon illustrating these two modes of operation is shown in figure 6.6.

6.4. Pure versus mixed-halide

Efforts by Kim *et al.* to replicate our MSSC system have been unsuccessful [84]. We postulate that the origin of this inconsistency could lie in the nature of the perovskite itself. While Kim *et al.* use the standard pure-halide perovskite we opt for a mixed-halide perovskite. To understand whether the mixing of the anions was indeed central to the operation of the MSSC we 'doped' the pure-iodide perovskite with the mixed-halide perovskite in the following percentages: 0, 1, 3, 10, 30, 70 and 100 % (resulting in the proportion of Cl in the halides being 0, 0.33, 0.99, 3.3, 9.9, 23.1, 33 % respectively) and devices using a precursor concentration of 30 wt % were fabricated on both TiO_2 and Al_2O_3. On alumina there was practically no current seen until about 10 % of the halides in the mixture were chlorine. The best performing devices were achieved for a third of the halide content being chlorine. The exact mechanism of why this occurs is yet unclear. We hypothesise that the substitution of some of the iodine atoms for the chlorine atoms would distort the perovskite lattice perhaps causing electrons to be less tightly bound in turn leading to improved conductivity. Four-point probe measurements and detailed x-ray diffraction analysis on these perovskite blends might shed light on the exact mechanism causing this switch on of current generation on alumina.

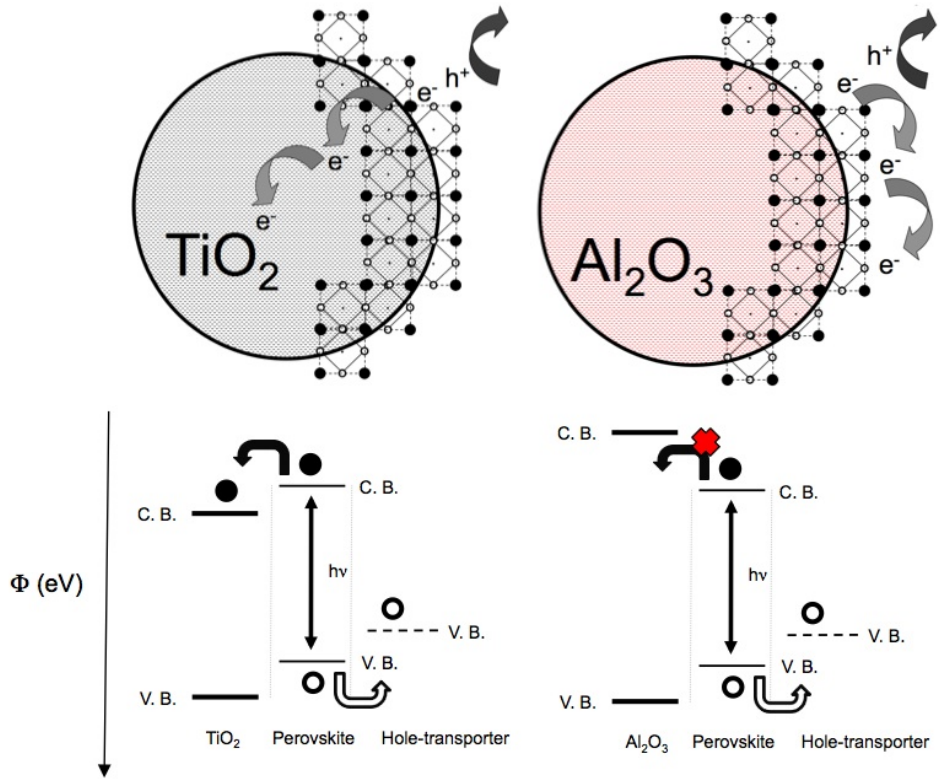

FIGURE 6.6. Schematic illustrating the charge transfer and charge transport in a perovskite-sensitized TiO_2 solar cell (left) and a noninjecting Al_2O_3-based solar cell (right); a representation of the energy landscape is shown below, with electrons shown as solid circles and holes as open circles.

6.5. Charge transport mechanism

In order to examine the charge generation in these devices we have performed photo-induced absorption (PIA) spectroscopy on the oxide films coated with the perovskite, both with and without the addition of spiro-OMeTAD, the results are shown in figure 6.9. For the mesoporous TiO_2 film coated with perovskite, the PIA spectrum reveals features in the near infrared assigned to the free electrons in the titania [85] therefore confirming effective sensitization of the titania by the perovskite. In contrast, films made of Al_2O_3 coated with perovskite exhibit no PIA signal confirming the insulating

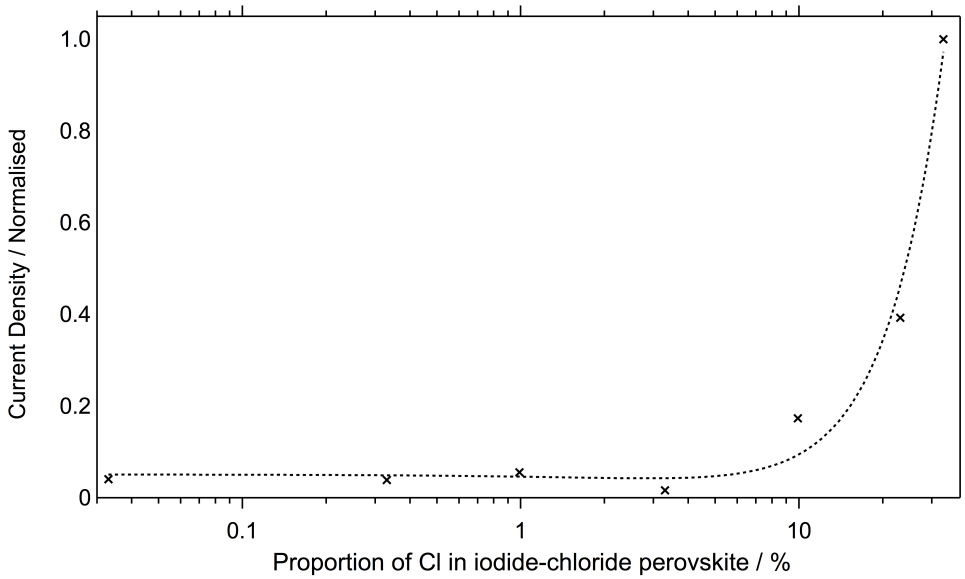

FIGURE 6.7. Current-density (normalised) versus proportion of Cl content in iodide-chloride perovskite on alumina scaffold, i.e. non-injecting oxide. Measurements taken by Leonie Vogt.

role of alumina (we additionally show dye-sensitized Al_2O_3 solar cells in figure 6.8 to confirm the insulating nature of Al_2O_3).

To confirm the insulating nature of alumina (Al_2O_3), solid-state dye-sensitized solar cells were made with either mesoporous titania (TiO_2) or mesoporous alumina (Al_2O_3). Figure 6.8 current-voltage characteristics under AM 1.5 (100 $mWcm^{-2}$) simulated sunlight (solid) and in dark (dashed) to red trace- TiO_2, and bottom black trace- Al_2O_3. The devices were constructed in the same manner as the perovskite-sensitized or the meso-superstructured solar cells (using spiro-OMeTAD as the hole-transporting medium); however, a prototypical ruthenium based dye (termed N719) was used in lieu of the perovskite absorber. The film thicknesses of the mesoporous TiO_2 and Al_2O_3 were around 500 nm, accounting for the relatively low photocurrent of the TiO_2 sensitized device. After addition of spiro-OMeTAD, we can efficiently monitor the oxidized species of spiro-OMeTAD created after photoexcitation of the perovskite. They have absorption features at 525 and 750 nm as well as a broad band

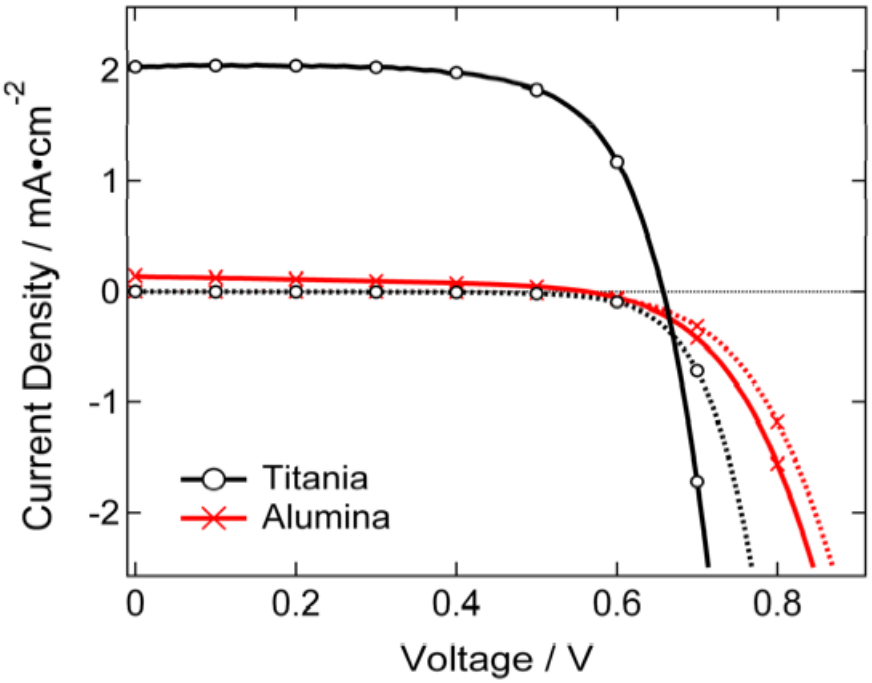

FIGURE 6.8. Current-voltage characteristics measured under AM 1.5 100mWcm^{-2} simulated sunlight (solid) and in dark (dashed) for solid-state dye-sensitised solar cells with TiO_2 (black trace with circles) and Al_2O_3 (red trace with crosses).

around 1200 nm, assigned to the hole located on the triarylamine moieties, [10, 86] which dominate the spectra in both the TiO_2 and Al_2O_3 based samples. These results indicate that hole-transfer is highly effective from the photoexcited perovskite to spiro-OMeTAD, and specifically that a hole-conductor is required to enable long lived charge species within the perovskite coated on the Al_2O_3. We note that the PIA signal is both dependent on the concentration and lifetime of the species monitored, hence from this measurement alone quantification of the relative charge generated yield is not possible.

In order to probe how effective the perovskite layer is at transporting electronic charge out of the device, we have performed small perturbation transient photocurrent decay measurements [87]. The solar cells are exposed to simulated sun light and 'flashed' with a small red light pulse, the decay rate of the transient photocurrent

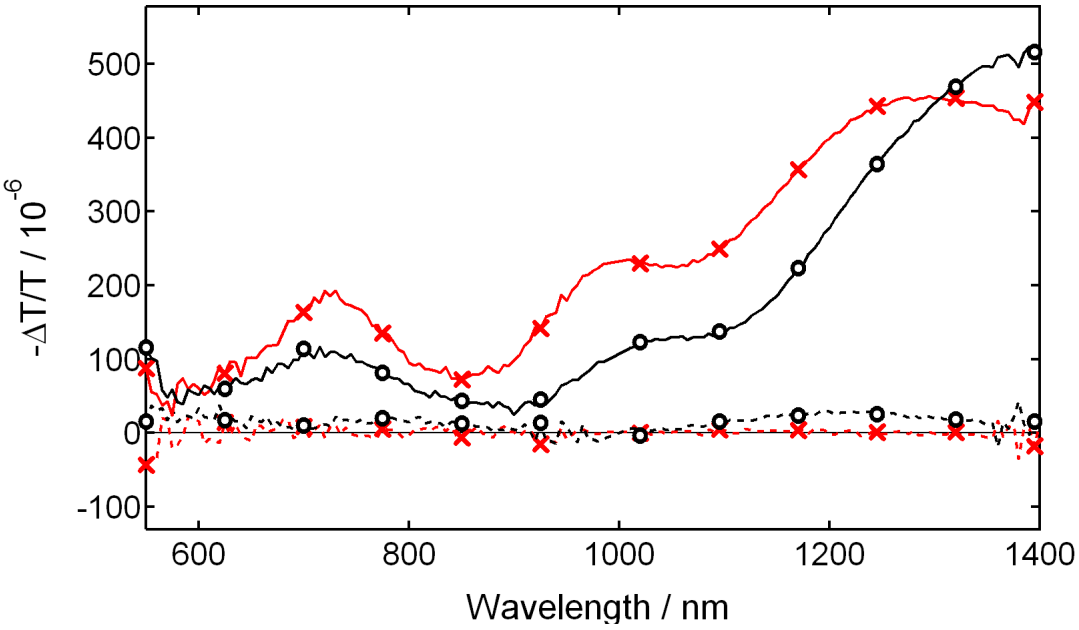

FIGURE 6.9. Photo-induced absorbance (PIA) spectra of the mesoporous TiO_2 (black open circles) and Al_2O_3 (red crosses) films coated with perovskite with (solid lines) and without (dashed lines) spiro-OMeTAD hole transporter. $\lambda_{ex} = 496.5$ nm, repetition rate 23 Hz. Measurement taken by Joel Teuscher.

signal is approximately proportional to the rate of charge transport out of the photoactive layer [87]. In figure 6.10, we observe over tenfold faster charge collection in the Al_2O_3 based devices than in the TiO_2 based sensitized devices indicating faster electron diffusion through the perovskite phase, than through the n-type TiO_2.

Since there is no n-type oxide in the Al_2O_3 -based cells, the devices are not 'sensitized' solar cells, but rather two-component hybrid solar cells. As designed, the Al_2O_3 is simply acting as a mesoscale 'scaffold' upon which the device is structured; we term this concept a 'mesosuperstructured solar cell' (MSSC). The above measurements demonstrate that long-lived charge carriers can be generated via hole transfer from the perovskite to spiro-OMeTAD and that the perovskite layer is faster at transporting electronic charge than the mesoporous TiO_2 . However, they do not explain the increase in V_{OC} values. The V_{OC} is generated by the build-up of electrons in the n-type material and holes in the p-type material, resulting in splitting of the quasi

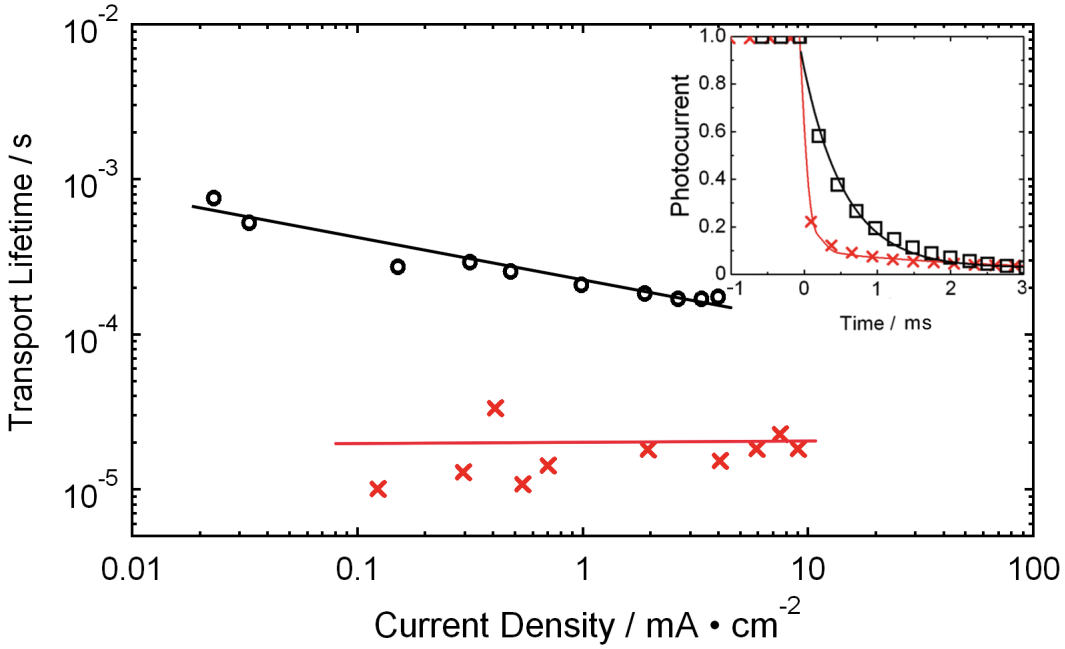

FIGURE 6.10. Charge transport lifetime determined by small perturbation transient photocurrent decay of perovskite sensitized TiO_2 (circles with black line to aid the eye) and Al_2O_3 cells (red crosses with line to aid the eye). Inset shows normalised photocurrent transients for Al_2O_3 (red trace with crosses every 7th point) and TiO_2 (black trace with circles every 7th point) cells, set to generate $5mA{\cdot}cm^{-2}$ photocurrent from the background light bias.

Fermi levels for both electrons and holes. For mesoporous TiO_2 , there exist sites in the tail of the density of states that extend into the band gap [88]. These fill with electrons under illumination; the result is that the quasi-Fermi level for electrons (E^*_{Fn}) is farther from the conduction band, for any given charge density, than would be the case if these states did not exist (i.e., in a highly crystalline semiconductor). The increased charge storing capacity of materials with a high density of sub-band gap states is termed 'chemical capacitance' [88]. There is, in essence, no chemical capacitance of the Al_2O_3 , and for the MSSCs all the electronic charge resides in the perovskite, moving the E^*_{Fn} in this material nearer to the conduction band for the same charge density. The higher voltage indicates that there are fewer surface and sub-band gap states in the perovskite films than in the mesoporous TiO_2 . Hence, the

increased voltage is caused by a substantial reduction of the chemical capacitance of the solar cell. We used a compact layer of TiO_2 as the electron-selective anode, but the chemical capacitance of this extremely thin (50 to 100 nm) TiO_2 layer was very low because of the low volume and surface area (i.e., flat). In addition, the compact layer deposited via spray pyrolysis has a donor density of 10^{18} cm^{-3} [89], and the sub-band gap sites responsible for the chemical capacitance may be full.

A central question is whether the MSSC is excitonic or a distributed p-n junction. The organometal halide perovskites tend to form layered structures, with continuous 2D metal halide planes perpendicular to the z-axis, and the lower dielectric organic components (methylamine) between these planes. The quasi 2D confinement of the excitons results in an increased exciton binding energy which can be up to a few hundred meV [90]. The reasonably high photocurrents from the planar junction solar cells (figure 6.3) could be explained by either moderately delocalized and highly mobile excitons being quenched at the perovskite spiro-OMeTAD interface, or the generation of free charges in the bulk of the perovskite films with reasonably good electron and hole-migration out of the devices. Further work is underway to identify if excitons play a significant role in this system.

6.6. Loss-in-potential vs band gap

The power-conversion efficiency for this system is at the very highest level for new and emerging solar technologies [59], but more exciting than the efficiency is the extremely high open-circuit voltage generated under 1 sun illumination. GaAs is the only other photovoltaic technology which both absorbs over the visible to near-IR region and generates such a high open-circuit voltage. Earlier we discussed one simple measure of the 'fundamental energy loss' in a solar cell as the difference in energy between the open-circuit voltage generated under full sunlight and the band gap of the absorber [77]. From the onset of the IPCE spectrum at 800 nm, we have

taken the optical band gap of the $CH_3NH_3PbCl_2I$ perovskite to be 1.55 eV [82]. The theoretical maximum open-circuit voltage can be estimated as a function of band gap following the Shockley-Queisser treatment [91]. For a material with a band gap of 1.55 eV the maximum possible open-circuit voltage under full sun illumination is 1.3V, yielding a minimum loss-in-potential 0.25 eV. In Figure 6.11, we have plotted the open-circuit voltage versus the optical-band gap of the absorber for the 'best-in-class' of most established and emerging solar technologies. For the perovskite MSSC we have taken the open-circuit voltage to be 1.1 V. With loss-in-potential as the only performance metric, the new technology is very well positioned in fourth place out of all solar technologies, behind GaAs, crystalline silicon and copper indium gallium (di)selenide. Remarkably the fundamental losses of this new technology are already lower than CdTe, with a loss-in-potential of 0.59 eV, which is the technology of choice for the world's largest solar company [92]. We note that all the materials used in the perovskite absorber, including solvents, are abundant and readily available. The cost of the absorber at the research scale (less than 1 kg) is \$0.70 (1.09) per m^2, which for a 10% efficient solar cell represents an addition of only 0.01 \$/Wp to the total solar cell cost. The ratio of \$/Wp is the ratio of the cost of a solar cell to the power generated under full (or peak) sun light, i.e. a 10% solar cell will generate 100 Wm^{-2} under full sun light, if it costs 100 $\$m^{-2}$ to manufacture the solar cell would be rated at 1 \$/Wp. The lowest cost solar cells are currently manufactured at 0.75 \$/Wp, hence, this new concept is a major contender for near-future large scale solar power generation.

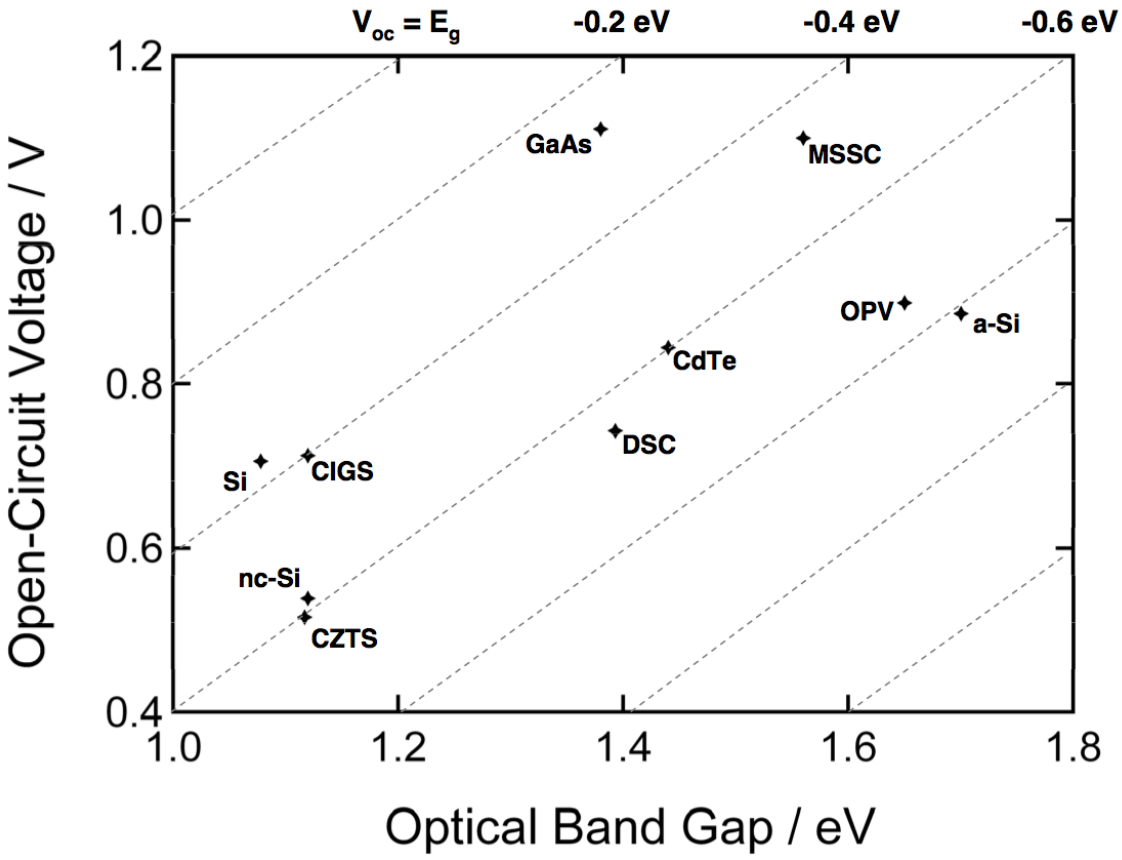

FIGURE 6.11. Open-circuit voltage versus optical band gap for the 'best-in-class' solar cells for most current and emerging solar technologies. The reference data were taken from [59]. The optical band gaps have been estimated by taking the onset of the incident photon-to-electron conversion efficiency for all technologies.

7. Conclusions and Outlook

In this thesis I have developed a solution for enhancing light-harvesting in thin-film photovoltaics through mesostructure design. I used polystyrene microspheres to template microvoids in mesoporous titanium dioxide. I report the highest photocurrent reported for low extinction and broadly absorbing ruthenium-based dye sensitiser (Z907) in a solid-state dye-sensitised solar cell (DSC). Further, I have developed a simple light-scattering back reflector by suspending scattering beads into a polymer matrix. Applying this back-reflector to our standard device resulted in near unity external quantum efficiencies indicating almost 100% of the incident light was converted into free charge and extracted at the terminals. After enhancing the solid-state DSC optically, I spent sometime improving the electronic properties of the solid-state DSC by studying various interfaces (electron/hole extraction layers, electron/hole blocking layers); however, this is not reported in this thesis due to unexpected results with a new material- the organometal halide perovskite.

Perovskites are an exciting prospect from a scientific and engineering point of view. The subset of perovskite I was particularly interested in was the organometal halide perovskite. Specifically, the methylammonium trihalide plumbate perovskite. I began with studying the rich variety of perovskite available through altering X anions (halogens), B cations (divalent metals), and A cations (organic component). My breakthrough was to stabilise perovskite for processing in air (i.e. without the need for a glovebox) by mixing the X anions. This perovskite was sealed and subjected to simulated 1 sun constant illumination, the perovskite was stable for over 1000 hours indicating that the perovskite itself is fundamentally stable under sunlight thus it is suitable for photovoltaic applications. Some rudimentary study of the basic properties (physical characterisation) of perovskites were done but much more work is needed here. As seen from chapter 8, many collaborations have been set up to char-

acterise the perovskite comprehensively. The focus of this thesis has been to develop the solid-state dye-sensitised solar cell device concept. However, understanding the fundamental material properties is of paramount importance and will be addressed in due course.

This thesis demonstrates the first embodiment of the perovskite-sensitised solid-state cell with photo-conversion efficiencies competitive with the state-of-the-art. While the perovskite had previously been demonstrated as a sensitiser on TiO_2 using a liquid electrolyte, poor stability (a few minutes) was reported. By switching the liquid-electrolyte with a solid-state hole-transporter I resolved the issue of short-term stability. I report over 10 hours of stability for an unsealed solid-state perovskite-sensitised device. Longer term stability is a target. I have done a lot of optimisation on the perovskite-sensitised solar cell. The key findings were that the role of surface is not particularly important since it appears that the device does not operate like a dye-sensitised solar cell but more like that of an extremely-thin absorber (ETA) solar cell. By co-sensitising the perovskite with dyes I showed that it is possible to change the onset of absorption (hence the colour of the device), this also opens up new routes for other advanced functional materials to be used. Electron diffusion was studied and the importance of perovskite layer thickness on charge recombination and light-harvesting was demonstrated, distinct differences were observed for pure and mixed-halide perovskites. Some preliminary work has begun on developing new perovskites absorbers with different optical and electronic character. A rigorous study of new perovskites is planned, new device applications beyond solar cells will be considered.

I have evolved the solid-state sensitized solar cell into a new low-cost concept, based on a mesostructured insulating scaffold, upon which extremely thin films of n-type and p-type semiconductors are assembled. The "meso-superstructured solar cell" (MSSC) concept has proven itself to be extraordinarily effective with an n-type perovskite, delivering over 10.9% power conversion efficiency under 1 sun illumination.

The key limitation in performance of the MSSC at present is a play off between series and shunt resistance. The perovskite absorber is reasonably conductive, measured to be on the order of (10^{-5} S cm^{-3}), and any instance of contact between the silver electrode and the perovskite absorber results in the short-circuiting of the device. This is overcome by processing a thick capping layer of spiro-OMeTAD. However, spiro-OMeTAD is less conductive (10^{-3} S cm^{-3}), and the thick capping layer reduces the fill factor of the solar cell, and thus represents a compromise. Routes to eliminate this shunting path without detrimentally increasing the series resistance of the cell are being pursued.

Further advances in overall power conversion efficiency are expected by extending the absorption onset towards 940 nm, by either implementing new perovskites or broadening this concept to other solution processable semiconductors. Enhancing the light absorption near the band edge through thicker films, or better photon management, will lead to increased photocurrent. Reduced series resistance through the application of higher mobility hole-transporters, or better control over the capping layer thickness will improve the fill factor. Better understanding of the influences upon open-circuit voltage will move this parameter closer to the theoretical maximum for single junction solar cells. The combination of these developments promises to deliver a low cost solar cell which is competitive with the very best, well established flat-plate solar technologies. Extending this system to multi-junction devices, notably without the requirement for lattice matching, should result in a globally competitive solar technology capable of being scaled to the terawatt level.

8. Further and on-going projects

8.1. Individual projects

Both light scattering systems developed in chapter 3 can be readily applied to the high-performance perovskite device detailed in chapter 6 which are expected to lead to even higher photo-conversion efficiencies. Beyond efficiency, understanding whether charge transport is influenced by mesostructure porosity will be interesting. In the early stages of my doctoral studies a lot of work was done on investigating hole-blocking layers in solid-state dye-sensitised solar cells, dense layers of metal-oxide so called 'compact layers'. One of the roles of the compact layer in the solid-state dye-sensitised solar cells is to nullify any shorting paths (created from pin-holes in the active layer) between the cathode (in this case a reflective Ag counter electrode) and anode (in this case a transparent conducting oxide F:SnO_2 or fluorine-doped tin-oxide FTO). Design rules for efficient electron-collecting electrodes were established through rigorous x-ray diffraction analysis and applied in the context of fully operational photovoltaics in order to understand the implications to device performance. Applying this design toolkit to the high-performance devices described in chapter 6 is also a target. However, the core result from this work was the optimised configuration (such as thickness, crystallinity, choice of oxide and even blends of oxides) vastly improves quality factor (i.e. improved reproducibility). Low temperature routes to forming compact layers were also studied. Of utmost importance is establishing a detailed physical description of the meso-superstructured solar cell beginning with a study of the organometal mixed-halide perovskite. Detailed x-ray diffraction studies are currently being undertaken and high-resolution transmission electron microscopy studies in collaboration with the University of Cambridge. Furthermore, studies to understand the formation of the perovskite according to temperature and atmosphere

with in-situ x-ray are planned. Detailed electronic studies with quantum hall measurements will be carried out with support from the Politecnico di Milano. Optoelectronic studies via photoelectron spectroscopy are underway with Uppsala University. While my short-term (10s of hours) stability studies are very positive, a milestone would be to achieve over 1000 hours of device stability. This is a very ambitious goal which will need highly co-ordinated efforts of which I will focus on developing new perovskites. The standard formula of ABX_3 where A is some organic component, B a divalent metal and X some halogen or mixture therein. The complexity of the A cation allows for many variations to be studied. Our group has recently purchased a nano-imprinting lithography suite. Nanostructuring the perovskite absorber via nano-imprint lithography will allow sub-100 nm features created on the perovskite layer, potentially leading to photonic effects such as near-field light trapping via plasmonic back reflectors [93].

8.2. Collaborative projects

Work on colloidal quantum-dot (CQD) solar cells has begun [94, 95, 96, 97]. In particular device architecture as route to achieve high performance CQD solar cells is being studied, for instance building an interpenetrated donor-acceptor bulk heterojunction structure to enhance light absorption and quicken charge extraction [98, 99]. The highly porous meso-structure developed through microsphere templating (see chapter 3.2) has been employed and improvements in performance reported with efficiencies of standard low-porosity systems at 3% and highly porous systems on average around 5% are reported.

Hybrid composites of semiconducting polymers and n-type metal oxides are interesting systems to study from a fundamental photophysical and device perspective. Contrary to organic solar cells, hybrid architectures offer a vast library of materials for device optimisation, including a variety of metal oxides, organic and inor-

ganic absorbers, molecular, polymeric and electrolytic hole-conducting media. The versatility offered by a hybrid framework allows these new materials to be utilised in novel configurations; one example being our newly developed mesoporous metal oxide/co-functionalized with surface adsorbed fullerene and absorber/polymer architecture [100]. Combining recently acquired knowledge about the C_{60}-SAM-polymer interface engineering with the optimised perovskite system is a route forward.

Optical-pump-terahertz-probe (OPTP) are planned in order to investigate charge carrier mobility and dynamics [101, 102, 103, 104]. By probing the full waveform of a terahertz pulse transmitted through the sample, the full complex dielectric function in the range from a few hundred gigahertz to a few terahertz can be directly constructed, thus it is possible to determine the conductivity of the sample in this frequency range. OPTP spectroscopy allows to use an optical pulse to excite free carriers at a well-defined point in time before the arrival of the THz pulse, thus early time carrier dynamics such as charge separation, trapping and recombination can be investigated with picosecond resolution.

Studying new solid-state hole-transporting materials with different ionisation potentials slightly above and below the one of 2,2',7,7'-tetrakis(N,Ndi-p-methoxyphenylamino)-9,9'-spirobifluorene (spiro-OMeTAD) to explore the possibility of reducing the overpotential between dye and hole transporting material in order to improve the device efficiency have been studied using transient absorption spectroscopy. Since the meso-superstructured solar cell reduces losses on the electron side it would be interesting to study the hole side.

The integration of carbon nanomaterials such as nanotubes or graphene is an exciting growth area in high-performance molecular electronics research [105]. Our initial attempts to integrate carbon nanotubes into the optimised perovskite device structure were promising because performance was not hindered, despite high loadings of nanotubes and random nanotube alignments. Future work would include investigating the formation of perovskites on nanotubes, where the nanotubes act as seeding

layers. Further, it would be interesting to understand the effect of the perovskites on nanotubes aligned or grown in vertical arrays or in the plane of the device.

References

[1] M. Graetzel, R. A. J. Janssen, D. B. Mitzi, and E. H. Sargent, "Materials interface engineering for solution-processed photovoltaics," *Nature*, vol. 488, no. 7411, pp. 304–312, 2012. 10.1038/nature11476.

[2] C. Candelise, M. Winskel, and R. Gross, "Implications for cdte and cigs technologies production costs of indium and tellurium scarcity," *Progress in Photovoltaics: Research and Applications*, vol. 20, no. 6, pp. 816–831, 2012.

[3] B. O'Regan and M. Gratzel, "A low-cost, high-efficiency solar cell based on dye-sensitized colloidal tio$_2$ films," *Nature*, vol. 353, no. 6346, pp. 737–740, 1991.

[4] S. A. Haque, E. Palomares, B. M. Cho, A. N. M. Green, N. Hirata, D. R. Klug, and J. R. Durrant, "Charge separation versus recombination in dye-sensitized nanocrystalline solar cells: the minimization of kinetic redundancy," *Journal of the American Chemical Society*, vol. 127, no. 10, pp. 3456–3462, 2005.

[5] J. N. Clifford, E. Palomares, M. K. Nazeeruddin, M. Grätzel, and J. R. Durrant, "Dye dependent regeneration dynamics in dye sensitized nanocrystalline solar cells: evidence for the formation of a ruthenium bipyridyl cation/iodide intermediate," *The Journal of Physical Chemistry C*, vol. 111, no. 17, pp. 6561–6567, 2007.

[6] U. Bach, D. Lupo, P. Comte, J. E. Moser, F. Weissortel, J. Salbeck, H. Spreitzer, and M. Gratzel, "Solid-state dye-sensitized mesoporous tio$_2$ solar cells with high photon-to-electron conversion efficiencies," *Nature*, vol. 395, no. 6702, pp. 583–585, 1998.

[7] S. Pelet, J.-E. Moser, and M. Grätzel, "Cooperative effect of adsorbed cations and iodide on the interception of back electron transfer in the dye sensitization of nanocrystalline tio2," *The Journal of Physical Chemistry B*, vol. 104, no. 8, pp. 1791–1795, 2000.

[8] J. E. Kroeze, N. Hirata, L. Schmidt-Mende, C. Orizu, S. D. Ogier, K. Carr, M. Graetzel, and J. R. Durrant, "Parameters influencing charge separation in solid-state dye-sensitized solar cells using novel hole conductors," *Advanced Functional Materials*, vol. 16, no. 14, pp. 1832–1838, 2006.

[9] L. Schmidt-Mende and M. Grätzel, "Tio$_2$ pore-filling and its effect on the efficiency of solid-state dye-sensitized solar cells," *Thin Solid Films*, vol. 500, no. 1–2, pp. 296–301, 2006.

[10] J. S. Henry, H.-B. Robin, C. Peter, C. Ilkay, M. Z. Shaik, and G. Michael, "Charge collection and pore filling in solid-state dye-sensitized solar cells," *Nanotechnology*, vol. 19, no. 42, p. 424003, 2008.

[11] J. Melas-Kyriazi, I. K. Ding, A. Marchioro, A. Punzi, B. E. Hardin, G. F. Burkhard, N. Tétreault, M. Grätzel, J.-E. Moser, and M. D. McGehee, "The effect of hole transport material pore filling on photovoltaic performance in solid-state dye-sensitized solar cells," *Advanced Energy Materials*, vol. 1, no. 3, pp. 407–414, 2011.

[12] A. Abrusci, I. K. Ding, M. Al-Hashimi, T. Segal-Peretz, M. D. McGehee, M. Heeney, G. L. Frey, and H. J. Snaith, "Facile infiltration of semiconducting polymer into mesoporous electrodes for hybrid solar cells," *Energy & Environmental Science*, vol. 4, no. 8, pp. 3051–3058, 2011.

[13] I. K. Ding, N. Tétreault, J. Brillet, B. E. Hardin, E. H. Smith, S. J. Rosenthal, F. Sauvage, M. Grätzel, and M. D. McGehee, "Pore-filling of spiro-ometad in solid-state dye sensitized solar cells: Quantification, mechanism, and consequences for device performance," *Advanced Functional Materials*, vol. 19, no. 15, pp. 2431–2436, 2009.

[14] N. Cai, S.-J. Moon, L. Cevey-Ha, T. Moehl, R. Humphry-Baker, P. Wang, S. M. Zakeeruddin, and M. Graetzel, "An organic d-π-a dye for record efficiency solid-state sensitized heterojunction solar cells," *Nano Letters*, vol. 11, no. 4, pp. 1452–1456, 2011.

[15] H. J. Snaith, A. J. Moule, C. Klein, K. Meerholz, R. H. Friend, and M. Grätzel, "Efficiency enhancements in solid-state hybrid solar cells via reduced charge recombination and increased light capture," *Nano Letters*, vol. 7, no. 11, pp. 3372–3376, 2007.

[16] G. Mie *Annalen der Physik*, vol. 377, p. 330(3), 1908.

[17] A. Usami, "Rigorous solutions of light scattering of neighboring tio_2 particles in nanocrystalline films," *Solar Energy Materials and Solar Cells*, vol. 59, no. 3, pp. 163–166, 1999.

[18] J. Ferber and J. Luther, "Computer simulations of light scattering and absorption in dye-sensitized solar cells," *Solar Energy Materials and Solar Cells*, vol. 54, no. 1–4, pp. 265–275, 1998.

[19] S. Ito, "High-efficiency organic-dye- sensitized solar cells controlled by nanocrystalline-tio2 electrode thickness," *Advanced Materials*, vol. 18, no. 9, pp. 1202–1205, 2006.

[20] Y. Chiba, A. Islam, Y. Watanabe, R. Komiya, N. Koide, and L. Han, "Dye-sensitized solar cells with conversion efficiency of 11.1%," *Japanese Journal of Applied Physics*, vol. 45, no. 25, pp. L638–L640, 2006.

[21] A. Yella, H.-W. Lee, H. N. Tsao, C. Yi, A. K. Chandiran, M. Nazeeruddin, E. W.-G. Diau, C.-Y. Yeh, S. M. Zakeeruddin, and M. Grätzel, "Porphyrin-sensitized solar cells with cobalt (ii/iii)–based redox electrolyte exceed 12 percent efficiency," *Science*, vol. 334, no. 6056, pp. 629–634, 2011.

[22] S. Hore, P. Nitz, C. Vetter, C. Prahl, M. Niggemann, and R. Kern, "Scattering spherical voids in nanocrystalline tio_2 - enhancement of efficiency in dye-sensitized solar cells," *Chemical Communications*, no. 15, pp. 2011–2013, 2005.

[23] S. Hore, C. Vetter, R. Kern, H. Smit, and A. Hinsch, "Influence of scattering layers on efficiency of dye-sensitized solar cells," *Solar Energy Materials and Solar Cells*, vol. 90, no. 9, pp. 1176–1188, 2006.

[24] S. Ito, T. Takeuchi, T. Katayama, M. Sugiyama, M. Matsuda, T. Kitamura, Y. Wada, and S. Yanagida, "Conductive and transparent multilayer films for low-temperature-sintered mesoporous tio_2 electrodes of dye-sensitized solar cells," *Chemistry of Materials*, vol. 15, no. 14, pp. 2824–2828, 2003.

[25] P. Wang, S. M. Zakeeruddin, J. E. Moser, M. K. Nazeeruddin, T. Sekiguchi, and M. Gratzel, "A stable quasi-solid-state dye-sensitized solar cell with an amphiphilic ruthenium sensitizer and polymer gel electrolyte," *Nat Mater*, vol. 2, no. 6, pp. 402–407, 2003. 10.1038/nmat904.

[26] W.-T. Reller, A., "A material for all seasons - perovskites," *Chem. Brit.*, vol. 25, p. 1227, 1989.

[27] R.-R. Muller, O., "The major ternary structural families, springer berlin heidelberg, new york," 1974.

[28] R. M. Hazen, "Perovskites," *Scientific American*, vol. 358, p. 52, 1988.

[29] A. S. Hyde, B. G., "Inorganic crystal structures," *Wiley Interscience, New York*, 1989.

[30] H. D. Megaw, "Crystal structures: a working approach," *Saunders, Philadelphia*, 1973.

[31] R. J. D. Tilley, "Perovskites: materials for all seasons," *Endeavour, New Series*, vol. 14, no. 3, p. 124, 1990.

[32] V. M. Goldschmidt, "On perovskites crystals and tolerances," *Oslo Press*, 1927.

[33] O. Tschauner, A. Zerr, S. Specht, A. Rocholl, R. Boehler, and H. Palme, "Partitioning of nickel and cobalt between silicate perovskite and metal at pressures up to 80[thinsp]gpa," *Nature*, vol. 398, no. 6728, pp. 604–607, 1999. 10.1038/19287.

[34] L.-G. Liu, "Post-oxide phases of olivine and pyroxene and mineralogy of the mantle," *Nature*, vol. 258, no. 5535, pp. 510–512, 1975. 10.1038/258510a0.

[35] G. R. Helffrich and B. J. Wood, "The earth's mantle," *Nature*, vol. 412, no. 6846, pp. 501–507, 2001. 10.1038/35087500.

[36] J. G. Bednorz and K. A. Müller, "Possible hight c superconductivity in the ba−la−cu−o system," *Zeitschrift für Physik B Condensed Matter*, vol. 64, no. 2, pp. 189–193, 1986.

[37] M. Green, W. C. Smith, and J. A. Weiner, "A thin film electrochromic display based on the tungsten bronzes," *Thin Solid Films*, vol. 38, no. 1, pp. 89–100, 1976.

[38] H. D. Megaw, "Changes in polycrystalline barium-strontium titanate at its transition temperature," *Nature*, no. 157, pp. 20–21, 1946.

[39] A. S. Bhalla, R. Guo, and R. Roy, "The perovskite structure – a review of its role in ceramic science and technology," *Material Research Innovations*, vol. 4, no. 1, pp. 3–26, 2000.

[40] J. Currey *J. Mater. Educ.*, vol. 9, p. 120, 1987.

[41] W. S. Lowenstam, H. A., "On biomineralization," *Oxford University Press, New York*, 1989.

[42] A. I. Caplan, "Materials synthesis utilizing biological processes," *Mater. Res. Sym. Proc.*, vol. 174, p. 9, 1990.

[43] C. D. Dimitrakopoulos and P. R. L. Malenfant, "Organic thin film transistors for large area electronics," *Advanced Materials*, vol. 14, no. 2, pp. 99–117, 2002.

[44] J. Takada, H. Awaji, M. Koshioka, A. Nakajima, and W. A. Nevin, "Organic–inorganic multilayers: A new concept of optoelectronic material," *Applied Physics Letters*, vol. 61, no. 18, pp. 2184–2186, 1992.

[45] Z. Xu, D. B. Mitzi, C. D. Dimitrakopoulos, and K. R. Maxcy, "Semiconducting perovskites (2-xc6h4c2h4nh3)2sni4 (x = f, cl, br): steric interaction between the organic and inorganic layers," *Inorganic Chemistry*, vol. 42, no. 6, pp. 2031–2039, 2003. Organic cation - focus on how it affects steric interactions. Confirm Sn-I-Sn bond angle when moved farther from 180deg the Eg goes up. Considers the effect of the lattice as increase size of halide ions.

[46] J. L. Knutson, J. D. Martin, and D. B. Mitzi, "Tuning the band gap in hybrid tin iodide perovskite semiconductors using structural templating," *Inorganic Chemistry*, vol. 44, no. 13, pp. 4699–4705, 2005.

[47] J.-H. Im, J. Chung, S.-J. Kim, and N.-G. Park, "Synthesis, structure, and photovoltaic property of a nanocrystalline 2h perovskite-type novel sensitizer (ch3ch2nh3)pbi3," *Nanoscale Research Letters*, vol. 7, no. 1, p. 353, 2012.

[48] K. Chondroudis and D. B. Mitzi, "Electroluminescence from an organic−inorganic perovskite incorporating a quaterthiophene dye within lead halide perovskite layers," *Chemistry of Materials*, vol. 11, no. 11, pp. 3028–3030, 1999.

[49] M. Era, T. Tsutsui, and S. Saito, "Polarized electroluminescence from oriented p-sexiphenyl vacuum-deposited film," *Applied Physics Letters*, vol. 67, no. 17, pp. 2436–2438, 1995.

[50] C. R. Kagan, D. B. Mitzi, and C. D. Dimitrakopoulos, "Organic-inorganic hybrid materials as semiconducting channels in thin-film field-effect transistors," *Science*, vol. 286, no. 5441, pp. 945–947, 1999.

[51] D. B. Mitzi, C. A. Feild, W. T. A. Harrison, and A. M. Guloy, "Conducting tin halides with a layered organic-based perovskite structure," *Nature*, vol. 369, no. 6480, pp. 467–469, 1994.

[52] D. B. Mitzi, *Synthesis, Structure, and Properties of Organic-Inorganic Perovskites and Related Materials*, pp. 1–121. John Wiley & Sons, Inc., 2007.

[53] T. Ishihara, "in optical properties of low-dimensional materials," *World Scientific*, pp. 288–339, 1995.

[54] A. Poglitsch and D. Weber, "Dynamic disorder in methylammoniumtrihalogenoplumbates (ii) observed by millimeter-wave spectroscopy," *The Journal of Chemical Physics*, vol. 87, no. 11, pp. 6373–6378, 1987.

[55] A. Kojima, K. Teshima, Y. Shirai, and T. Miyasaka, "Organometal halide perovskites as visible-light sensitizers for photovoltaic cells," *Journal of the American Chemical Society*, vol. 131, no. 17, pp. 6050–6051, 2009.

[56] R. Wasylishen, O. Knop, and J. Macdonald, "Cation rotation in methylammonium lead halides," *Solid State Communications*, vol. 56, no. 7, pp. 581 – 582, 1985.

[57] N. Kitazawa, Y. Watanabe, and Y. Nakamura, "Optical properties of ch3nh3pbx3 (x = halogen) and their mixed-halide crystals," *Journal of Materials Science*, vol. 37, no. 17, pp. 3585–3587, 2002.

[58] J.-H. Im, C.-R. Lee, J.-W. Lee, S.-W. Park, and N.-G. Park, "6.5perovskite quantum-dot-sensitized solar cell," *Nanoscale*, vol. 3, no. 10, pp. 4088–4093, 2011.

[59] M. A. Green, K. Emery, Y. Hishikawa, W. Warta, and E. D. Dunlop, "Solar cell efficiency tables (version 39)," *Progress in Photovoltaics: Research and Applications*, vol. 20, no. 1, pp. 12–20, 2012.

[60] G. Yu, J. Gao, J. C. Hummelen, F. Wudl, and A. J. Heeger, "Polymer photovoltaic cells: Enhanced efficiencies via a network of internal donor-acceptor heterojunctions," *Science*, vol. 270, no. 5243, pp. 1789–1791, 1995.

[61] J. J. M. Halls, C. A. Walsh, N. C. Greenham, E. A. Marseglia, R. H. Friend, S. C. Moratti, and A. B. Holmes, "Efficient photodiodes from interpenetrating polymer networks," *Nature*, vol. 376, no. 6540, pp. 498–500, 1995.

[62] J. Tang, K. W. Kemp, S. Hoogland, K. S. Jeong, H. Liu, L. Levina, M. Furukawa, X. Wang, R. Debnath, D. Cha, K. W. Chou, A. Fischer, A. Amassian, J. B. Asbury, and E. H. Sargent, "Colloidal-quantum-dot photovoltaics using atomic-ligand passivation," *Nature Materials*, vol. 10, no. 10, pp. 765–771, 2011.

[63] T. K. Todorov, K. B. Reuter, and D. B. Mitzi, "High-efficiency solar cell with earth-abundant liquid-processed absorber," *Advanced Materials*, vol. 22, no. 20, pp. E156–E159, 2010.

[64] Y. Itzhaik, O. Niitsoo, M. Page, and G. Hodes, "Sb_2s_3-sensitized nanoporous tio_2 solar cells," *The Journal of Physical Chemistry C*, vol. 113, no. 11, pp. 4254–4256, 2009.

[65] J. A. Chang, S. H. Im, Y. H. Lee, H.-j. Kim, C.-S. Lim, J. H. Heo, and S. I. Seok, "Panchromatic photon-harvesting by hole-conducting materials in inorganic–organic heterojunction sensitized-solar cell through the formation of nanostructured electron channels," *Nano Letters*, vol. 12, no. 4, pp. 1863–1867, 2012.

[66] Olson, "Band-offset engineering for enhanced open-circuit voltage in polymer–oxide hybrid solar cells," *Advanced Functional Materials*, vol. 17, no. 2, pp. 264–269, 2007.

[67] T. Horiuchi, H. Miura, and S. Uchida, "Highly efficient metal-free organic dyes for dye-sensitized solar cells," *Journal of Photochemistry and Photobiology A: Chemistry*, vol. 164, no. 1–3, pp. 29–32, 2004.

[68] L. Schmidt-Mende, U. Bach, R. Humphry-Baker, T. Horiuchi, H. Miura, S. Ito, S. Uchida, and M. Grätzel, "Organic dye for highly efficient solid-state dye-sensitized solar cells," *Advanced Materials*, vol. 17, no. 7, pp. 813–815, 2005.

[69] T. Horiuchi, H. Miura, and S. Uchida, "Highly-efficient metal-free organic dyes for dye-sensitized solar cells," *Chemical Communications*, no. 24, pp. 3036–3037, 2003.

[70] N. Fuke, R. Katoh, A. Islam, M. Kasuya, A. Furube, A. Fukui, Y. Chiba, R. Komiya, R. Yamanaka, L. Han, and H. Harima, "Influence of ticl4 treatment on back contact dye-sensitized solar cells sensitized with black dye," *Energy & Environmental Science*, vol. 2, no. 11, pp. 1205–1209, 2009.

[71] A. Kay and M. Graetzel, "Artificial photosynthesis. 1. photosensitization of titania solar cells with chlorophyll derivatives and related natural porphyrins," *The Journal of Physical Chemistry*, vol. 97, no. 23, pp. 6272–6277, 1993.

[72] M. D. Brown, P. Parkinson, T. Torres, H. Miura, L. M. Herz, and H. J. Snaith, "Surface energy relay between cosensitized molecules in solid-state dye-sensitized solar cells," *The Journal of Physical Chemistry C*, vol. 115, no. 46, pp. 23204–23208, 2011.

[73] T. Leijtens, I. K. Ding, T. Giovenzana, J. T. Bloking, M. D. McGehee, and A. Sellinger, "Hole transport materials with low glass transition temperatures and high solubility for application in solid-state dye-sensitized solar cells," *ACS Nano*, vol. 6, no. 2, pp. 1455–1462, 2012.

[74] P. Docampo, A. Hey, S. Guldin, R. Gunning, U. Steiner, and H. J. Snaith, "Pore filling of spiro-ometad in solid-state dye-sensitized solar cells determined via optical reflectometry," *Advanced Functional Materials*, vol. 22, no. 23, pp. 5010–5019, 2012.

[75] L. Han, A. Islam, H. Chen, C. Malapaka, B. Chiranjeevi, S. Zhang, X. Yang, and M. Yanagida, "High-efficiency dye-sensitized solar cell with a novel co-adsorbent," *Energy & Environmental Science*, vol. 5, no. 3, pp. 6057–6060, 2012.

[76] A. H. Ip, S. M. Thon, S. Hoogland, O. Voznyy, D. Zhitomirsky, R. Debnath, L. Levina, L. R. Rollny, G. H. Carey, A. Fischer, K. W. Kemp, I. J. Kramer, Z. Ning, A. J. Labelle, K. W. Chou, A. Amassian, and E. H. Sargent, "Hybrid passivated colloidal quantum dot solids," *Nature Nanotechnology*, vol. advance online publication, 2012.

[77] H. J. Snaith, "Estimating the maximum attainable efficiency in dye-sensitized solar cells," *Advanced Functional Materials*, vol. 20, no. 1, pp. 13–19, 2010.

[78] G. Dennler, M. C. Scharber, and C. J. Brabec, "Polymer-fullerene bulk-heterojunction solar cells," *Advanced Materials*, vol. 21, no. 13, pp. 1323–1338, 2009.

[79] B. E. Hardin, H. J. Snaith, and M. D. McGehee, "The renaissance of dye-sensitized solar cells," *Nature Photonics*, vol. 6, no. 3, pp. 162–169, 2012.

[80] J. Burschka, A. Dualeh, F. Kessler, E. Baranoff, N.-L. Cevey-Ha, C. Yi, M. K. Nazeeruddin, and M. Grätzel, "Tris(2-(1h-pyrazol-1-yl)pyridine)cobalt(iii) as p-type dopant for organic semiconductors and its application in highly efficient solid-state dye-sensitized solar cells," *Journal of the American Chemical Society*, vol. 133, no. 45, pp. 18042–18045, 2011.

[81] J. Nelson, "Continuous-time random-walk model of electron transport in nanocrystalline tio$_2$ electrodes," *Physical Review B*, vol. 59, no. 23, pp. 15374–15380, 1999.

[82] D. A. R. Barkhouse, O. Gunawan, T. Gokmen, T. K. Todorov, and D. B. Mitzi, "Device characteristics of a 10.1% hydrazine-processed cu2znsn(se,s)4 solar cell," *Progress in Photovoltaics: Research and Applications*, vol. 20, no. 1, pp. 6–11, 2012.

[83] A. Kojima, M. Ikegami, K. Teshima, and T. Miyasaka, "Highly luminescent lead bromide perovskite nanoparticles synthesized with porous alumina media," *Chemistry Letters*, vol. 41, no. 4, pp. 397–399, 2012.

[84] H.-S. Kim, C.-R. Lee, J.-H. Im, K.-B. Lee, T. Moehl, A. Marchioro, S.-J. Moon, R. Humphry-Baker, J.-H. Yum, J. E. Moser, M. Gratzel, and N.-G. Park, "Lead iodide perovskite sensitized all-solid-state submicron thin film mesoscopic solar cell with efficiency exceeding 9 10.1038/srep00591.

[85] G. Rothenberger, D. Fitzmaurice, and M. Graetzel, "Spectroscopy of conduction band electrons in transparent metal oxide semiconductor films: optical determination of the flatband potential of colloidal titanium dioxide films," *The Journal of Physical Chemistry*, vol. 96, no. 14, pp. 5983–5986, 1992.

[86] G. Boschloo and A. Hagfeldt, "Photoinduced absorption spectroscopy as a tool in the study of dye-sensitized solar cells," *Inorganica Chimica Acta*, vol. 361, no. 3, pp. 729–734, 2008.

[87] P. Docampo, S. Guldin, M. Stefik, P. Tiwana, M. C. Orilall, S. Hüttner, H. Sai, U. Wiesner, U. Steiner, and H. J. Snaith, "Control of solid-state dye-sensitized solar cell performance by block-copolymer-directed tio$_2$ synthesis," *Advanced Functional Materials*, vol. 20, no. 11, pp. 1787–1796, 2010.

[88] J. Bisquert, "Chemical capacitance of nanostructured semiconductors: its origin and significance for nanocomposite solar cells," *Physical Chemistry Chemical Physics*, vol. 5, no. 24, pp. 5360–5364, 2003.

[89] L. Kavan and M. Grätzel, "Highly efficient semiconducting tio$_2$ photoelectrodes prepared by aerosol pyrolysis," *Electrochimica Acta*, vol. 40, no. 5, pp. 643–652, 1995.

[90] T. Ishihara, J. Takahashi, and T. Goto, "Optical properties due to electronic transitions in two-dimensional semiconductors (c$_n$h$_{2n+1}$nh$_3$)$_2$pbi$_4$)," *Physical Review B*, vol. 42, no. 17, pp. 11099–11107, 1990.

[91] W. Shockley and H. J. Queisser, "Detailed balance limit of efficiency of p-n junction solar cells," *Journal of Applied Physics*, vol. 32, no. 3, pp. 510–519, 1961.

[92] www.firstsolar.com, "First solar website," 2012.

[93] I. K. Ding, J. Zhu, W. Cai, S.-J. Moon, N. Cai, P. Wang, S. M. Zakeeruddin, M. Grätzel, M. L. Brongersma, Y. Cui, and M. D. McGehee, "Plasmonic dye-sensitized solar cells," *Advanced Energy Materials*, vol. 1, no. 1, pp. 52–57, 2011.

[94] E. H. Sargent, "Infrared photovoltaics made by solution processing," *Nat Photon*, vol. 3, no. 6, pp. 325–331, 2009. 10.1038/nphoton.2009.89.

[95] J. Tang and E. H. Sargent, "Infrared colloidal quantum dots for photovoltaics: Fundamentals and recent progress," *Advanced Materials*, vol. 23, no. 1, pp. 12–29, 2011.

[96] I. J. Kramer and E. H. Sargent, "Colloidal quantum dot photovoltaics: A path forward," *ACS Nano*, vol. 5, no. 11, pp. 8506–8514, 2011.

[97] R. Debnath, O. Bakr, and E. H. Sargent, "Solution-processed colloidal quantum dot photovoltaics: A perspective," *Energy & Environmental Science*, vol. 4, no. 12, pp. 4870–4881, 2011.

[98] D. A. R. Barkhouse, R. Debnath, I. J. Kramer, D. Zhitomirsky, A. G. Pattantyus-Abraham, L. Levina, L. Etgar, M. Grätzel, and E. H. Sargent, "Depleted bulk heterojunction colloidal quantum dot photovoltaics," *Advanced Materials*, vol. 23, no. 28, pp. 3134–3138, 2011.

[99] I. J. Kramer, D. Zhitomirsky, J. D. Bass, P. M. Rice, T. Topuria, L. Krupp, S. M. Thon, A. H. Ip, R. Debnath, H.-C. Kim, and E. H. Sargent, "Ordered nanopillar structured electrodes for depleted bulk heterojunction colloidal quantum dot solar cells," *Advanced Materials*, vol. 24, no. 17, pp. 2315–2319, 2012.

[100] G. Grancini, R. S. Santosh Kumar, A. Abrusci, H.-L. Yip, C.-Z. Li, A.-K. Y. Jen, G. Lanzani, and H. J. Snaith, "Boosting infrared light harvesting by molecular functionalization of metal oxide/polymer interfaces in efficient hybrid solar cells," *Advanced Functional Materials*, vol. 22, no. 10, pp. 2160–2166, 2012.

[101] M. C. Beard, G. M. Turner, and C. A. Schmuttenmaer, "Terahertz spectroscopy," *The Journal of Physical Chemistry B*, vol. 106, no. 29, pp. 7146–7159, 2002.

[102] C. A. Schmuttenmaer, "Exploring dynamics in the far-infrared with terahertz spectroscopy," *Chemical reviews*, vol. 104, no. 4, pp. 1759–1779, 2004. Review.

[103] P. Parkinson, J. Lloyd-Hughes, Q. Gao, H. H. Tan, C. Jagadish, M. B. Johnston, and L. M. Herz, "Transient terahertz conductivity of gaas nanowires," *Nano Letters*, vol. 7, no. 7, pp. 2162–2165, 2007.

[104] P. Tiwana, P. Docampo, M. B. Johnston, H. J. Snaith, and L. M. Herz, "Electron mobility and injection dynamics in mesoporous zno, sno2, and tio2 films used in dye-sensitized solar cells," *ACS Nano*, vol. 5, no. 6, pp. 5158–5166, 2011.

[105] T. C. Dinadayalane and J. Leszczynski, "Remarkable diversity of carbon–carbon bonds: structures and properties of fullerenes, carbon nanotubes, and graphene," *Structural Chemistry*, vol. 21, no. 6, pp. 1155–1169, 2010.

List of Figures

List of Figures—*Continued*

List of Figures—*Continued*

List of Figures—*Continued*

LIST OF FIGURES—*Continued*

List of Figures—*Continued*

List of Tables